THE ANGULAR DISTRIBUTIONS OF PHOTONEUTRONS IN LEAD 206 AND 208 USING MONOCHROMATIC PHOTONS

By

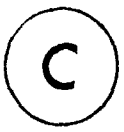

JOHN NICHOLAS BARKMAN

A Thesis

Submitted to the School of Graduate Studies

in Partial Fulfilment of the Requirements

for the Degree

Doctor of Philosophy

McMaster University

May 1980

DOCTOR OF PHILOSOPHY (1980) McMASTER UNIVERSITY
(Physics)

TITLE: The Angular Distributions of Photoneutrons in Lead 206 and 208 Using Monochromatic Photons

AUTHOR: JOHN NICHOLAS BARKMAN, B.Sc. (Waterloo University)

SUPERVISOR: Dr. T.J. Kennett

NUMBER OF PAGES: 154

ABSTRACT

In this work, an experiment to measure the angular distributions of neutrons generated in the (γ,n) reaction is described. Data are presented for the separated isotopes ^{206}Pb and ^{208}Pb and from the data analysis, the results are used to infer the extent of photon multipole mixing between 7 and 11 MeV, within the framework of the statistical collective nuclear model.

The experiment made use of an intense beam of highly monochromatic photons generated by neutron capture on nickel and chromium in the core of the McMaster Nuclear Reactor, and a high resolution Helium-3 neutron detector. Photoneutron spectra were recorded at seven angles between 20 and 160 degrees, and angular distribution functions were determined for all observed transitions.

Of considerable interest especially in ^{208}Pb, is the question of M1 strength in the energy range of this experiment. The results of this work cannot confirm the existence of M1 strength; but evidence of multipole mixing, most likely E2 : E1, was found at all photon energies. Estimates of the ratio of E2 to E1 strength are presented at all photon energies investigated for both lead isotopes.

ACKNOWLEDGMENTS

Throughout the period in which the experiments, analysis and writing of this work were accomplished, there were many people who contributed in large and small ways to its completion. First of all, I must thank my supervisor, Dr. T.J. Kennett who provided support, guidance and understanding throughout the project. I benefited greatly from his experience and knowledge in all aspects of the field. The same can also be said for Dr. W.V. Prestwich who contributed a great deal of guidance, impetus and enthusiasm.

The staff of the McMaster Nuclear Reactor should also be thanked for their support and co-operation. John McFee, from his previous work with the beam port facility and the neutron detector, supplied much help in the early stages of the experiments. As well as John, I would also like to thank the late Garnet Jones and Tom Cousins for their assistance in setting up the experimental system. The latter and Doris Stevanovic also contributed by proofreading and making copies of the manuscript. For any problems with the electronics or computing, Kenrick Chin was always a great help at virtually any hour of the day or night.

I appreciated the drafting talents of Diane Lowe, who took time from her own work to draw most of the figures; hers were the ones that were drawn neatly. For typing the manuscript under adverse conditions, my thanks go to Dorothy Matthews who persevered even after they came and took her typewriter away. In the last few weeks, Lynda Hills was a great help in finishing the typing.

Finally, I would like to thank all the citizens of the Nuclear Research Building (NRB), many of whom have since moved on to other adventures, for making my stay interesting and unforgettable, and for making the old place seem like home for a while.

TABLE OF CONTENTS

		Page
CHAPTER I	INTRODUCTION	1
1.1	EXPERIMENTAL TECHNIQUES	4
1.2	COLLECTIVE EXCITATION IN LEAD 206 AND 208	10
CHAPTER 2	THEORY	14
2.1	THE INTERACTION OF PHOTONS AND NUCLEI	14
2.1.1	PHOTOABSORPTION PROCESSES	14
2.1.2	EXCITATION OF A GIANT RESONANCE	17
2.1.3	CLASSIFICATION OF GIANT MULTIPOLE RESONANCES	21
2.2	ANGULAR DISTRIBUTIONS	23
2.2.1	ANGULAR DISTRIBUTION COEFFICIENTS	24
2.2.2	REACTION MATRIX ELEMENTS π_{A-1}	32
2.2.3	THE ANGULAR DISTRIBUTION FOR $j_{A-1}=\frac{1}{2}^-$	39
CHAPTER 3	THE EXPERIMENTAL SYSTEM	43
3.1	THE BEAM PORT FACILITY	44
3.2	TARGET DETECTOR GEOMETRY	50
3.3	THE HELIUM 3 SPECTROMETER	55
3.3.1	NEUTRON DETECTION	55
3.3.2	CHARGE COLLECTION	59
3.3.3	THE FNS-1 SPECTROMETER	62
3.4	ELECTRONICS	64
3.5	THE BEAM MONITOR	67

		Page
CHAPTER 4	DATA ANALYSIS	71
4.1	DATA ACQUISITION	72
4.2	IDENTIFICATION OF NEUTRON GROUPS	75
4.3	REACTION RATES	75
4.3.1	DETERMINATION OF PEAK AREAS	76
4.3.2	COUNTING TIMES	82
4.4	THE ANGULAR DISTRIBUTIONS	84
4.4.1	SPREAD IN PHOTONEUTRON EMISSION ANGLES	85
4.4.2	CALCULATION OF THE $Q_\nu(\cos\theta)$ FUNCTIONS	92
4.4.3	THE ANGULAR DISTRIBUTION FUNCTIONS AND ASYMMETRY PARAMETER	92
CHAPTER 5	RESULTS AND DISCUSSION	95
5.1	LEAD 206	95
5.1.1	THE PHOTONEUTRON SPECTRA	95
5.1.2	THE ANGULAR DISTRIBUTIONS	101
5.1.3	MULTIPOLE MIXING	108
5.2	LEAD 208	114
5.2.1	THE PHOTONEUTRON SPECTRA	114
5.2.2	THE ANGULAR DISTRIBUTIONS	119
5.2.3	MULTIPOLE MIXING	125
5.3	CONCLUSIONS AND RECOMMENDATIONS	126
TABLES		129
APPENDIX I	PHOTONEUTRON ANGULAR DISTRIBUTION OF THE 8884 keV RESONANCE IN ^{49}Ti	143
APPENDIX II	ANGULAR DISTRIBUTION COEFFICIENTS FOR PHOTONEUTRON REACTIONS ON A 0^+ TARGET NUCLEUS	144
REFERENCES		152

LIST OF FIGURES

		Page
2.1	Nuclear Photoexcitation Cross-Section	15
2.2	Collective Multipole Oscillations of the Nucleus	22
2.3	Schematic of a Photoneutron Transition	26
2.4	Interference between Reaction Channels	29
2.5	Neutron Optical Model Transition Probabilities for A=207	36
2.6	Hard Sphere Scattering Phase Angles for A=207	40
3.1	The Photoneutron Experimental Facility	46
3.2	Neutron Capture Gamma Ray Source Holder	47
3.3	Neutron Spectrum with Aluminum Target in Beam	49
3.4	Contour Profile of the Beam Intensity	52
3.5	The Rotatable Neutron Detector Holder	53
3.6	The $^{3}He(n,p)^{3}H$ Cross-Section	57
3.7	Specifications of the FNS-1 ^{3}He Neutron Ionization Chamber	63
3.8	The Electronics for Neutron Counting	65
3.9	The Beam Monitor System	69
4.1	Data Acquisition System Block Diagram	73
4.2	Spectral Deconvolution Using Bayes Theorem	83
4.3	Determination of the Angular Spread	87
4.4	Detector Angular Spreads at 20, 40, 60 and 90 degrees	90
4.5	The Modified Legendre Polynomials	93
5.1	Photoneutron Spectrum of Pb-206 with Nickel Source at 90 Degrees	96

		Page
5.2	Photoneutron Spectra of Pb 206 with Nickel Source at all Angles	97
5.3	Photoneutron Spectrum of Pb-206 with Chromium Source at 90 Degrees	98
5.4	Photoneutron Spectra of Pb-206 with Chromium Source at all Angles	99
5.5	Pb-206 Angular Distributions: Transitions to Ground State and 2 keV Doublet of Pb-205	102
5.6	Pb-206 Angular Distributions: Transitions to the 263 keV Level of Pb-205	103
5.7	Pb-206 Angular Distributions: Transitions to the 576 keV Level of Pb-205	104
5.8	Pb-206 Angular Distributions: Transitions to Higher Levels of Pb-205	105
5.9	Variation of Angular Distribution Coefficients and Asymmetry Parameter with Photon Energy for Pb-206	107
5.10	E2:E1 Mixing Ratio and Phase Angle for a_1 Coefficient	111
5.11	Photoneutron Spectrum of Pb.208 with Nickel Source at 90 Degrees	115
5.12	Photoneutron Spectrum of Pb-208 with Nickel Source at all Angles	116
5.13	Photoneutron Spectrum of Pb-208 with Chromium Source at 90 Degrees	117
5.14	Photoneutron Spectrum of Pb-208 with Chromium Source at all Angles	118
5.15	Pb-208 Angular Distributions: Transitions to Ground State of Pb-207	120
5.16	Pb-208 Angular Distributions: Transitions to 570 keV Level of Pb-207	121
5.17	Pb-208 Angular Distributions: Transitions to 898 keV Level of Pb-207	122
5.18	Variation of Angular Distribution Coefficients and Asymmetry Parameter with Photon Energy for Pb-208	123

LIST OF TABLES

		Page
3.1	Material Properties and Isotopic Analysis of the Separated Lead Samples	128
5.1	Expected and Observed Photoneutron Transitions in the Reaction $^{206}Pb(\gamma,n)^{205}Pb$	129
5.2	Angular Distributions for $^{206}Pb(\gamma,n)^{205}Pb$ E_γ = 8999 keV	130
5.3	Angular Distributions for $^{206}Pb(\gamma,n)^{205}Pb$ E_γ = 9720 keV	131
5.4	Angular Distributions for $^{206}Pb(\gamma,n)^{205}Pb$ E_γ = 8884/8484, 8512 keV	132
5.5	Neutron Transmission Probabilities and Phase Angles for all Transitions: $^{206}Pb(\gamma,n)^{205}Pb$	133
5.6	Lead 206 Mixing Ratios	134
5.7	Expected and Observed Photoneutron Transitions in the Reaction $^{208}Pb(\gamma,n)^{207}Pb$	135
5.8	Angular Distributions for $^{208}Pb(\gamma,n)^{207}Pb$ E_γ = 8990 keV	136
5.9	Angular Distributions for $^{208}Pb(\gamma,n)^{207}Pb$ E_γ = 8533 keV	137
5.10	Angular Distributions for $^{208}Pb(\gamma,n)^{207}Pb$ E_γ = 9720 keV	138
5.11	Angular Distributions for $^{208}Pb(\gamma,n)^{207}Pb$ E_γ = 8884 keV	139
5.12	Angular Distributions for $^{208}Pb(\gamma,n)^{207}Pb$ E_γ = 8484, 8512, 7819, 10054, 11387 keV	140

		Page
5.13	Neutron Transmission Probabilities and Phase Angles Small Transitions: $^{208}Pb(\gamma,n)^{207}Pb$	141
5.14	Lead 208 Mixing Ratios	142

CHAPTER I

INTRODUCTION

The study of photon induced collective excitation of nuclei has been of great interest to both experimentalists and theoreticians for the last forty years. Much of the initial effort focused on the phenomenon known as the Giant Dipole Resonance (GDR), which came to be associated with the electric dipole oscillation of the nucleus (Mi44).. Its energy and gross structure were explained by collective or hydrodynamical models (Go48, St50) in which protons and neutrons oscillate against each other. Subsequently, microscopic models were developed to explain the observed fine structure (Br59, Gi66) associated with the individual nuclear levels.

Giant collective resonances of different multipolarity, both electric and magnetic, have also been predicted by the models, and experimental evidence exists for several of these resonances. Of particular interest to this experiment are the isoscalar Giant Quadrupole Resonance and the Giant Magnetic Dipole Resonance, which have energies that are expected to lie within the range of photon energies used in this experiment. The giant E2 resonance was first

predicted by Bohr and Mottelson (Mo60), and both hydrodynamical (Bo76) and shell model calculations (Be75), predict its energy at 63 $A^{-1/3}$ MeV (10.6 MeV for lead-208). The search for M1 strength, especially in lead-208, has been extensive between 5 and 10 MeV (Ho79), but its energy has not been established conclusively and theoretical predictions vary considerably (Ho79).

The objective of this experimental work was to identify collective E2 or M1 excitation in the isotopes ^{206}Pb and ^{208}Pb for photon energies between 7.8 and 11.4 MeV. Since most of this energy range lies on the low energy tails of the Giant Dipole and Electric Quadrupole Resonances, and since the photon energy resolution is of the order of 1 eV, much less than the level spacing, the observed multipole strengths will be influenced by the fine structure associated with individual nuclear level resonances (see Figure 2.1). Also, since the source of photons is neutron capture on materials in the core of a nuclear reactor, only certain specific photon energies can be obtained. For these reasons, a systematic study of the variation of multipole strengths with photon energy was not possible. A series of measurements at several isolated energies, however, should provide meaningful

evidence of the extent of different multipole strengths.

In this experiment, the angular distributions of neutrons generated in the photoneutron (γ,n) reaction:

$$\gamma + {}^{N}_{Z}A \rightarrow n + {}^{N-1}_{Z}(A-1) \ , \qquad (1.1)$$

were investigated. The photoneutron reaction is well suited for the study of collective excitation of nuclei in this energy region, since it dominates the photoabsorption cross-section. These energies are also below the thresholds for competing reactions, (γ,np) and $(\gamma,2n)$. At this point, however, an explanation should be given as to how the angular distribution of photoneutrons provides a useful contribution to the study of collective multipole excitation of the nucleus.

If a photon energy matches exactly the energy of a nuclear level above the binding energy of a neutron, it can be shown that the angular distribution of photoneutrons will be symmetric about 90 degrees. Conversely, any asymmetry is evidence for contributions of at least two multipoles. Since the E1 strength is well established on the tail of the GDR, the angular distributions can provide a measure of the extent of E2 or M1 mixing. Other experimental techniques used in the identification of multipole

collective excitation include the comparison of the integrated cross-section of a resonance with an Energy Weighted Sum Rule (Sa74), and photoneutron polarization methods (Ho 79). The former method cannot be used without a variable energy photon source, and the latter would require extensive experimental facilities.

The photoneutron reaction is only one of many methods used to study the collective excitation of nuclei. Other photoparticle reactions can be used at higher energies, as can radiative capture reactions, such as (n,γ) or (p,γ). Elastic photon scattering is another useful tool. Excitation via individual photons in such experiments as inelastic electron, proton and alpha scattering has also been studied extensively. In the next section, a short critique of the experimental method used in this work is given and a comparison with other methods is presented. The remainder of this chapter summarizes the previous work and findings on the photoexcitation of lead 206 and 208 and how the present work contributes to the overall study.

1.1 EXPERIMENTAL TECHNIQUES

Photon Sources

Beams of high energy photons may be generated either

electromagnetically or by nuclear excitation. The former includes bremsstrahlung and positron annihilation in flight techniques, both of which involve intense high energy electron beams; and the latter includes such reactions as (p,γ) and neutron capture. A brief outline of the sources used in photoneutron work is given here.

Bremsstrahlung experiments utilise a high energy electron beam, which strikes a metal foil, emitting a continuous photon spectrum characterised by a well defined maximum energy determined by the electron energy. The threshold yield technique was the first used (Fi70). In these experiments, the maximum photon energy is increased in small increments to yield an integrated cross-section which can be unfolded analytically to determine the cross-section $\sigma_{\gamma n}(E_\gamma)$. Energy resolution is improved ($\sim$ 100 keV near E_γ = 10 MeV) and analysis made simpler with the "tagged photon" technique using a bremsstrahlung monochromator (Oc62). In this technique, the electrons passing through the foil are energy analysed, and by selecting a small energy window, the detected electrons are used as a coincidence criterion for the photons. A different bremsstrahlung threshold technique can be used to obtain excellent resolution (Ho79). In this case the entire bremsstrahlung spectrum is

incident on the target, and the resulting photoneutron spectrum is in fact a measure of the photon energy. This method is limited to studies involving transitions to one state of the residual nucleus.

Positron annihilation in flight has also been used as a photon source in photoneutron experiments (Mi62, Fu62). In this case, an energetic, intense electron beam strikes a high Z target, producing high energy positrons which are allowed to annihilate in a second material, generating a forward peaked cone of photons with energy $E_{pos}+\frac{1}{2}mc^2$. The resulting photon resolution is typically of the order of 250 keV. The main limitation of this technique is the extremely high electron beam intensity needed to produce a strong enough beam of photons. Nuclear excitation sources include such reactions as $^{19}F(p,\alpha\gamma)^{16}O$, $^{7}Li(p,\gamma)^{8}Be$ and $^{3}H(p,\gamma)^{4}He$ which produce discrete spectra with resolutions between 15 and 130 keV. In the last reaction, the photon energy can be varied by changing the proton energy, but this is not true for other reactions. An alternate intense source of photons is neutron capture on certain materials placed in the core of a nuclear reactor. Resolution is excellent, only $\sim$ 1 eV due to the thermal motion of the source atoms. This method has been used for

(γ,n) work (We61, Gr64, Hu67, Mc77) and is the source of photons used in this experiment. The major drawback is that the photon energy cannot be varied without using a Compton monochromator with a subsequent loss of resolution.

Neutron Detection

The choice of neutron detection techniques depends on the photon source. Time of flight methods utilise high speed detectors with little or no energy information such as organic scintillators, as in the case for bremsstrahlung monochromator experiments where fast coincidence timing is necessary. Time of flight measurements involve two detectors placed several meters apart along the neutron flight path, which provide two pulses from the same neutron to start and stop a time to amplitude converter (TAC) whose output is thus related to the neutron energy. This technique is also used in bremsstrahlung threshold experiments.

Because of the low counting efficiency due to the small solid angle and the decreased duty cycle, this method is not well suited for positron annihilation in flight experiments where the photon beam intensities are lower. High efficiency detectors such as BF_3 counters are used but these give no energy information; so, this technique is

suitable mainly for total photoneutron cross-section experiments.

Recently, high resolution ^{3}He neutron detectors have been made (Cu69), which permit high count rate neutron spectra to be recorded with an energy resolution of about 15 keV for thermal neutrons to 27 keV at 1 MeV. Solid angle can be made very large for increased counting efficiency, but for an angular distribution measurement, the solid angle must be reduced to minimize angular resolution effects.

Comparison of Experimental Techniques

For this experiment, a beam of high energy photons between 7 and 11 MeV was obtained by placing either nickel or chromium sources in the core of the McMaster Nuclear Reactor. The highly monochromatic photons were collimated onto external targets of the separated isotopes ^{206}Pb and ^{208}Pb. Photoneutrons were detected by a high resolution ^{3}He ionization chamber which could be rotated about the sample between 20 and 160 degrees with respect to the beam axis.

This technique possesses the superior photon energy resolution not available with electromagnetic sources. The one exception is the bremsstrahlung tnreshold technique,

which is suitable only for transitions to the ground state of the residual nucleus. The photon intensity from a neutron capture source can be superior to the elctromagnetic sources which have low duty cycles. For a thermal neutron flux of $2 \times 10^{13}/cm^2 \cdot s$ in the reactor core, a collimated beam of 10^6 photons/s above 7 MeV can be obtained.

The major drawback of the (n,γ) technique is that the photon energy cannot be varied. Electromagnetic sources then are more suitable for mapping the cross-section as a function of energy. Because of their poorer resolution, e.m. sources are also more suited for studies where one wishes to average over the contributions of the fine structure in the cross-section. Conversely, neutron capture or bremsstrahlung threshold sources are better for studying the individual level structure.

The choice of a ^3He detector enables several photo-neutron transitions, each characterized by the photon energy and energy level of the residual nucleus, to be recorded concurrently in a single spectrum. For example, using the chromium source and the ^{208}Pb target, eleven different transitions can be seen, arising from three different photon energies and seven levels of ^{207}Pb. Photon and level energies are reasonably well spaced; so that most transitions

can be resolved. The movable ^{3}He detector allows angles of 20 to 160 degrees from the beam axis to be obtained with a minimum of movement, and with identical target-detector geometry.

In summary, the experimental techniques employed in this study permit a broad angular range, identification of many individual transitions, and a high intensity source of photons covering a suitably wide range of energies.

1.2 COLLECTIVE EXCITATION IN LEAD 206 AND 208

There are several reasons for choosing the isotopes ^{206}Pb and ^{208}Pb for the photoneutron angular distribution measurements. Lead 208 is a doubly magic nucleus, and as such has been the object of a great deal of theoretical interest from both collective and microscopic approaches. The latter are especially attractive because of the small number of intermediate states involved in particle-hole calculations. In addition, the wide spacing of most of the low lying levels of the residual nuclei make analysis of the photoneutron spectra straightforward. Also, the photoneutron Q-values, 8089 $\pm$ 3 keV for ^{206}Pb (Ba79) and 7367.7 $\pm$ 0.7 keV for ^{208}Pb (Wa77), are low enough to permit investigation with neutron capture photon sources and high enough that neutron

energies are in the range of reasonable detector efficiency. Finally, both isotopes have 0^+ ground states; so, the multipolarity of the photoexcitation determines exactly the spin of the intermediate level. This greatly simplifies the angular distribution analysis.

In the past few years, there has been a great deal of interest in the M1 strength in lead 208. M1 modes should be readily excited in doubly magic ^{208}Pb from the spin-flip transitions of an outer shell neutron ($i_{13/2} \rightarrow i_{11/2}$) or proton ($h_{11/2} \rightarrow h_{9/2}$). Predictions of the location and magnitude of the magnetic dipole components have ranged between 5.4 and 10.3 MeV, and there are still considerable differences in the interpretation of the experimental results. A summary of the present state of the knowledge of M1 strength in ^{208}Pb is given in a paper by Holt et al. (Ho79), and since the results of the present work cannot unambiguously identify M1 strength in lead 208, the question of M1 strength in this isotope will not be discussed.

M1 strength in ^{206}Pb has been reported (Fa75) from electron scattering experiments, but at energies below the photoneutron threshold.

The isoscalar E2 resonance is well established in

both nuclei at 63 $A^{-1/3}$ MeV. In ^{208}Pb, this has manifested itself as structure on the low energy shoulder of the Giant Dipole Resonance in (γ,n) experiments (Ve70), as well as from inelastic scattering of electrons (Pi77), protons (Le73), ^{3}He(Mo73) and alpha particles (Yo76). In all these investigations, sum rule considerations were used in determining the multipole assignments.

Evidence for E2 (or possibly M1) strength, in addition to the contribution from the GDR has been found from previous measurements of the angular distribution of photoneutrons in both lead isotopes. These experiments are outlined below.

Measurements of the cross-sections of a few photoneutron transitions were made at 38 and 142 degrees for a natural lead target and the same experimental facility used in this work (Mc77). Asymmetry was found at all photon energies investigated, indicating E1:E2 or possibly E1:M1 mixing. A series of experiments, conducted in Israel (Bi79) were run concurrently with this study, and angular distribution measurements between 40 and 140 degrees were done for ^{206}Pb using nickel and chromium photons from neutron capture on nickel and chromium. Evidence for E1:E2 mixing was found and comparison was made with calculations based on the direct semi-direct model (Be79).

For lead 208, angular distribution measurements between 45 and 135 degrees were made in the giant resonance region, 9.9 to 11.2 MeV using the tagged photon techniques (Be79). The results were compared to predictions of the direct-semi-direct model by considering an E2 resonance at 10.8 MeV. In another experiment, at lower energies (7.4 to 8.4 MeV), both photoneutron yield and polarization were measured at 90^{0} and 135^{0} to identify spin and parity of individual levels (Mo79). Several E1, M1 and E2 transitions were found. The high resolution bremsstrahlung threshold technique was used for this study. The lead 208 work in the present experiment covers the region between the two investigations discussed above, 7.8 to 11.4 MeV.

In the following chapters, the details and results of this experiment are explained. The evidence for multipole mixing, seen by asymmetry in the angular distributions is presented, and an estimate of the degree of mixing is made based on the statistical collective model.

CHAPTER 2

THEORY

2.1 THE INTERACTION OF PHOTONS AND NUCLEI

2.1.1 PHOTO ABSORPTION PROCESSES

The photoneutron reaction is only one of several modes of nuclear photoexcitation. Photonuclear phenomena may be classified under two groups: absorption and scattering. At various photon energies certain types of interaction may predominate while others may be impossible. The total photoabsorption cross-section of a typical high A nucleus is shown in Figure 2.1, (Be76), and the structure over several energy regions is outlined below.

I. $E_\gamma < 6$ MeV

In this range, the photon wavelength is of the order of atomic distances; so, nuclear effects are small. The predominant nuclear interaction is Nuclear Thomson scattering which is the interaction of the photon with the dipole moment associated with the oscillation of the nucleus as a whole. At higher photon energies, resonance absorption interactions with individual low lying bound nuclear levels can occur.

II. 6 MeV $< E_\gamma <$ 9 MeV

Resonance excitation of individual unbound

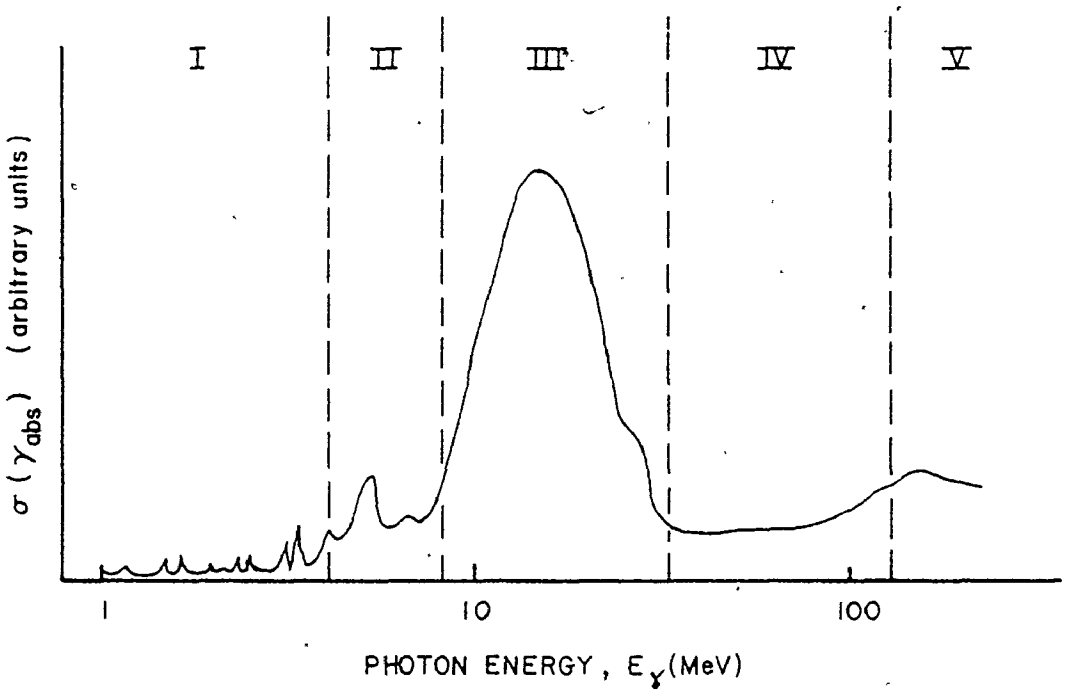

I	(< 6 MeV)	Photoexcitation of bound nuclear states
II	(6 to 9 MeV)	Excitation of unbound individual levels
III	(9 to 30 MeV)	Giant resonances - Collective excitation
IV	(30 to 100 MeV)	Short range inter-nucleon correlations
V	(> 100 MeV)	Excitations of individual nucleon resonances

Figure 2.1: Nuclear Photoexcitation Cross-section of a Typical High Z Nucleus (Be76)

nuclear levels predominates in this range which can be associated with nuclear shell model effects.

At energies above the neutron binding energy, the photoneutron interaction dominates the cross-section. Other phenomena include Delbrück scattering, Nuclear Rayleigh scattering and inelastic Nuclear Raman scattering. Collective nuclear modes may also be excited, as components of the M1 and E2 giant resonances are expected to be found in this region. The tail of the giant dipole resonance predominates.

III. 10 MeV < E_γ < 30 MeV

Above 10 MeV in heavy nuclei, the individual level structure of the cross-section disappears as the levels overlap and the massive structure known as the giant dipole resonance dominates. This wide resonance, with a maximum near 14 MeV in lead and a width of $\sim$ 10 MeV is the interaction between the photon and the nuclear electric dipole moment from the oscillation of protons and neutrons against each other. The photoneutron reaction is the major component of the total cross-section with other photo-particle reactions such as (γ,p), $(\gamma,2n)$ and (γ,np) contributing at higher energies.

IV. 30 MeV < E_γ < 100 MeV

When the photon wavelength is of the order of the nuclear spacing, the short range correlations between individual nucleons are affected. Particle production is still the major interaction, and the cross-section decreases smoothly with increasing energy.

V. E_γ > 100 MeV

The photoexcitation cross-section increases above the photopion threshold. Here, the photon wavelength is comparable to the size of a nucleon, so individual nucleon resonances can be excited.

2.1.2 EXCITATION OF A GIANT RESONANCE

The resonance photoexcitation of a nucleus in the energy range of photons used in this experiment (7 to 10 MeV) has been described by considering either the interaction of a photon with the collective motion of nucleons, or by the excitation of single unbound nuclear levels. Collective models can provide a visual explanation and are useful in classifying giant resonances by associating the various multipole resonances with different modes of oscillation of the nucleus.

The wide structure of a giant resonance, however, can be considered an envelope of many overlapping individual

states which are so closely spaced, especially in heavy nuclei, that they cannot be seen. In lighter nuclei and below the giant dipole resonance in heavy nuclei, however, part of the total strength of a given "giant" resonance excitation occurs in isolated single levels; so that, shell model effects must form part of the description of such structure. In general, a photon bringing in L units of angular momentum can promote a particle (a neutron, in a photoneutron reaction) out of its ground state level, leaving a 1 particle - 1 hole excitation. This causes a change in the nucleonic density and hence generates a variation δV_L in the nuclear potential. Associated with δV_L is the field operator F_L which acts on the nucleon in its ground state

$$F_L|0\rangle = \sum_n |n\rangle\langle n|F_L|0\rangle = \sum_n M_n^L|n\rangle \qquad 2.1$$

where $\sum_n M_n^L|n\rangle$ is a giant resonance collective state. Thus even a single level transition can be considered to lead to collective nuclear motion. Both the shell model (Sa74, Br59) and hydrodynamical models which consider groups of nucleons as fluids within the nucleus (Go48,St50), can predict the energies of the various multipole resonances.

The multipole nature of the excitation of a nucleus by an electromagnetic field can be illustrated by considering the Hamiltonian of the system

$$H_{total} = H_{nucleus} + H_{\gamma} + H'_{int.} \quad . \quad 2.2$$

The interaction Hamiltonian can be expressed in terms of the vector potential of the electromagnetic field $\vec{a}$, and the nucleus of A nucleons of charge e_i, mass M_i, momentum $\vec{p}_i$, spin $\vec{s}_i$ and magnetic moment μ_i:

$$H'_{int} = \sum_{i=1}^{A} \frac{e_i^2 |\vec{a}|^2}{2M_i c^2} - \frac{e_i}{M_i c} \vec{p}_i \cdot \vec{a} + \mu_i \vec{s}_i \cdot (\vec{\nabla} \times \vec{a}) \quad . \quad 2.3$$

The first term describes photon scattering while the last two represent photon absorption via electric and magnetic interactions. If the vector potential is expanded in a power series in r in the last two terms, the various electric and magnetic multipole components of the interaction can be identified.

For example, the electric dipole excitations can be isolated by using the first term in the power series expansion of $\vec{a}$ ($a_0 \vec{\varepsilon}$ where $\vec{\varepsilon}$ is the photon polarization vector) in the second term of equation 2.3:

$$H'_{E1} = \frac{-e a_0}{c} \sum_{i=1}^{Z} \vec{v}_i \cdot \vec{\varepsilon} \quad . \quad 2.4$$

Here the sum is over Z protons of charge e and velocity $\vec{v}_i = \vec{p}_i / M_i$. By separating the centre of mass motion, one can arrive at the following expression of the interaction (Ha64)

$$H'_{E1} = \frac{-e x_o}{c} \left(A(\vec{v}_{cm} \cdot \vec{\varepsilon}) + \frac{N}{A} \sum_{i=1}^{Z} (\vec{v}_i \cdot \vec{\varepsilon}) - \frac{Z}{A} \sum_{j=1}^{N} (\vec{v}_j \cdot \vec{\varepsilon}) \right) , \quad 2.5$$

where the three terms represent:

i) Nuclear Thomson scattering from the dipole oscillation of the nuclear centre of mass

ii) the interaction with Z protons of effective charge $q_p^{(E1)} = \frac{Ne}{A}$

iii) the interaction with N neutrons of effective charge $q_n^{(E1)} = - \frac{Ze}{A}$.

The latter two terms describe a collective oscillation of neutrons against protons, since the "effective charges" are of opposite sign. This collective motion has been associated with the isovector E1 or giant dipole resonance.

Collective oscillations of a nucleus, whether described by a microscopic shell model or a hydrodynamical model are useful in illustrating the various multipole giant resonances.

2.1.3 CLASSIFICATION OF GIANT MULTIPOLE RESONANCES.

The giant multipole resonances may be classified in a pictorial manner by considering the basic oscillations of a nucleus (Ha76). A giant resonance is specified by three properties:

(i) Nature of excitation : electric (E) or magnetic (M).

(ii) Mode of excitation : isoscalar or isovector.

(iii) Multipolarity : L = 0,1,2,...

In an electric excitation, no distinction is made between nucleons of different spin ($\Delta S=0$); whereas a magnetic excitation distinguishes between different spins ($\Delta S=1$). Nucleons of identical isospin behave identically in an isoscalar mode ($\Delta T=0$), but protons and neutrons are affected differently in an isovector transition ($\Delta T=1$). The nuclear symmetry of each oscillation is determined by the multipolarity.

A pictorial representation of the various collective nuclear oscillations associated with each multipole resonance is given in Figure 2.2. The isoscalar electric modes (EL_{is}) involve in-phase oscillations of all nucleons ($\Delta S=0, \Delta T=0$). EO_{is}, called a "breathing" mode, represents compression of the nucleus; it cannot be excited by a real photon, only by virtual photons in experiments such as inelastic electron

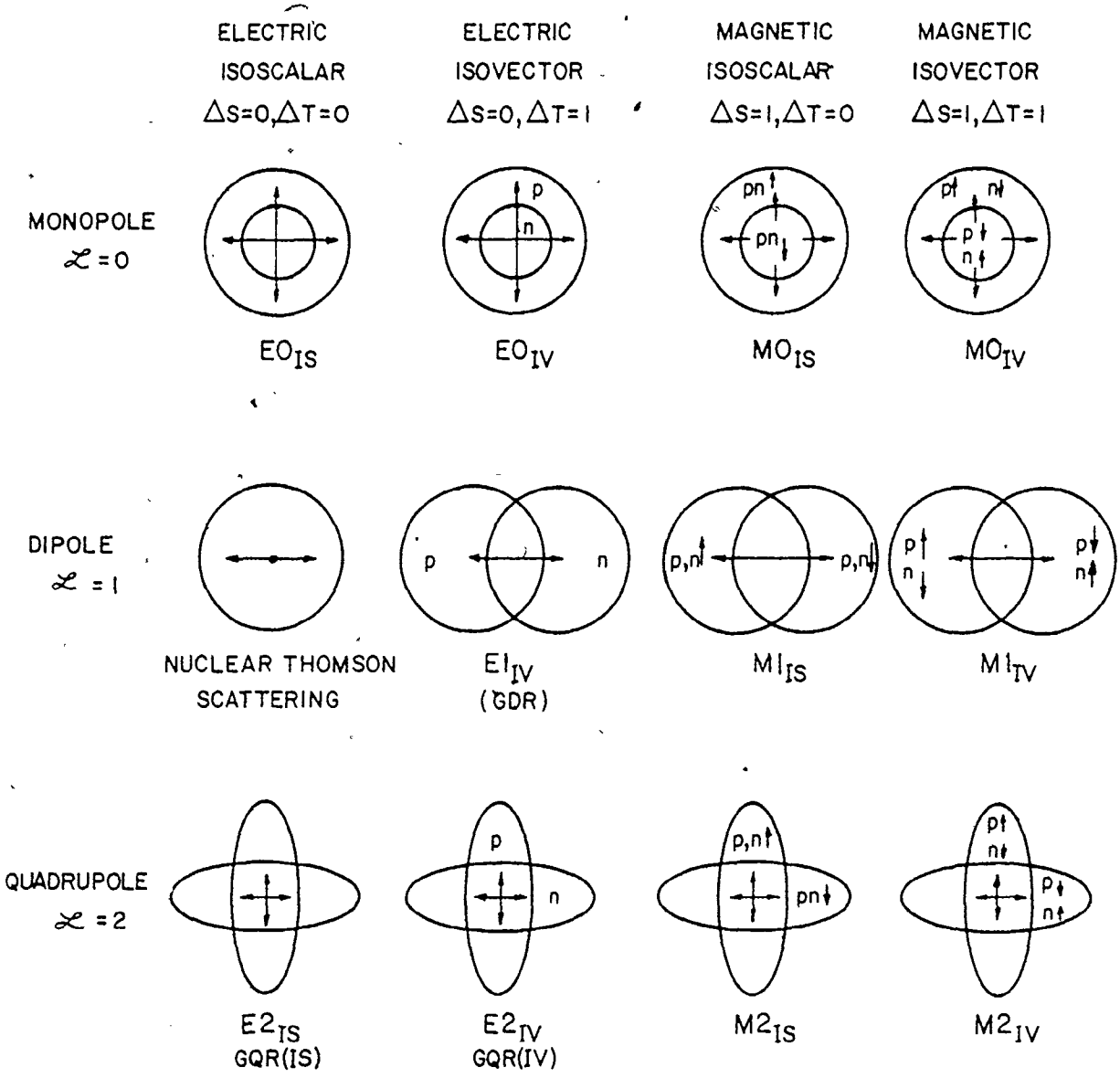

Figure 2.2: Collective Multipole Oscillations of the Nucleus. The nature of the collective nuclear oscillations, both Electric and Magnetic up to $\mathcal{L} = 2$ are shown.

scattering. As mentioned before, the El_{is} mode corresponds to Nuclear Thomson scattering. The isoscalar quadrupole resonance ($E2_{is}$ or GQR_{is}) has been observed below the GDR.

In the isovector electric modes (EL_{iv}), protons and neutrons oscillate out of phase ($\Delta S=0$, $\Delta T=1$). The giant dipole resonance (El_{iv} or GDR) and the isovector giant quadrupole resonance ($E2_{iv}$ or GQR_{iv}) above the GDR are both well established phenomena.

Isoscalar magnetic modes correspond to the oscillation of all spin-up nucleons against spin-down nucleons ($\Delta S=1$, $\Delta T=0$); whereas the isovector magnetic modes are spin-isospin oscillations ($\Delta S=1$, $\Delta T=1$). Since M0 transitions are forbidden, only the magnetic dipole and higher multipoles represent real excitations. The giant magnetic dipole resonance (GMDR) is expected below the GDR.

2.2 ANGULAR DISTRIBUTIONS

In photonuclear reactions, asymmetry about 90 degrees in the angular distributions is due to the interference between excitations of different electromagnetic multipoles. By considering electric dipole and quadrupole interactions only, in a direct photoneutron process, the sign of the asymmetry term (proportional to $\cos\theta$) is determined by the product of the

neutron effective charges, q_n^{E1} and q_n^{E2} (Ca75). Since these charges are

$$q_n^{E1} = -\frac{Z}{A}e \qquad 2.6a$$

$$q_n^{E2} = +\frac{Z}{A^2}e \,, \qquad 2.6b$$

the photoneutron angular distributions should be peaked at backwards angles in a direct reaction. This is not the case for many transitions.

Using a semi-direct process formalism (Ca75) in which the reaction proceeds through a "doorway state", forward peaked distributions could also be predicted, by including a semi-direct term in effective charges. In this work, the angular distributions are explained in terms of the statistical compound model of the nucleus such that the interaction proceeds randomly between many overlapping intermediate states (Pr62). This treatment implies an uncoupling of the photon and neutron amplitudes of the reaction matrix elements.

2.2.1 ANGULAR DISTRIBUTION COEFFICIENTS

The photoneutron reaction

$$\gamma + {}^{N}_{Z}A \rightarrow {}^{N}_{Z}A^{*} \rightarrow n + {}^{N-1}_{Z}(A-1) \,,$$

can be considered a compound interaction with an entrance channel specified by the photon multipolarity, the spin and parity

of both the target nucleus A and the intermediate state A^*; followed by an exit channel defined by the orbital angular momentum and spin of the neutron, and the spin and parity of the residual nucleus (A-1). The interaction is depicted in Figure 2.3 and the quantum numbers describing the reaction are listed here. The notation for the parameters used is basically that used by Carr and Baglin (Ca71), and Firk (Fi70), where

$J_A^{\pi A}$	is the spin and parity of the target nucleus ${}^{N}_{Z}A$ (0^+ for both lead 206 and 208),
p	is the nature of the photoexcitation, (p=0 for magnetic, and p=1 for electric),
L	is the photon multipolarity,
J^{π}	is the spin and parity of the intermediate level ${}^{N}_{Z}A^*$,
ℓ	is the neutron orbital angular momentum,
j_n	is the neutron spin (=½), and
$j_{A-1}^{\pi A-1}$	is the spin and parity of the residual nucleus.

The exit channel, consisting of the neutron and residual nucleus, is characterized by its spin,

$$\vec{s} = \vec{j}_{A-1} + \vec{j}_n$$

or

$$s = j_{A-1} \pm \tfrac{1}{2} . \qquad 2.7$$

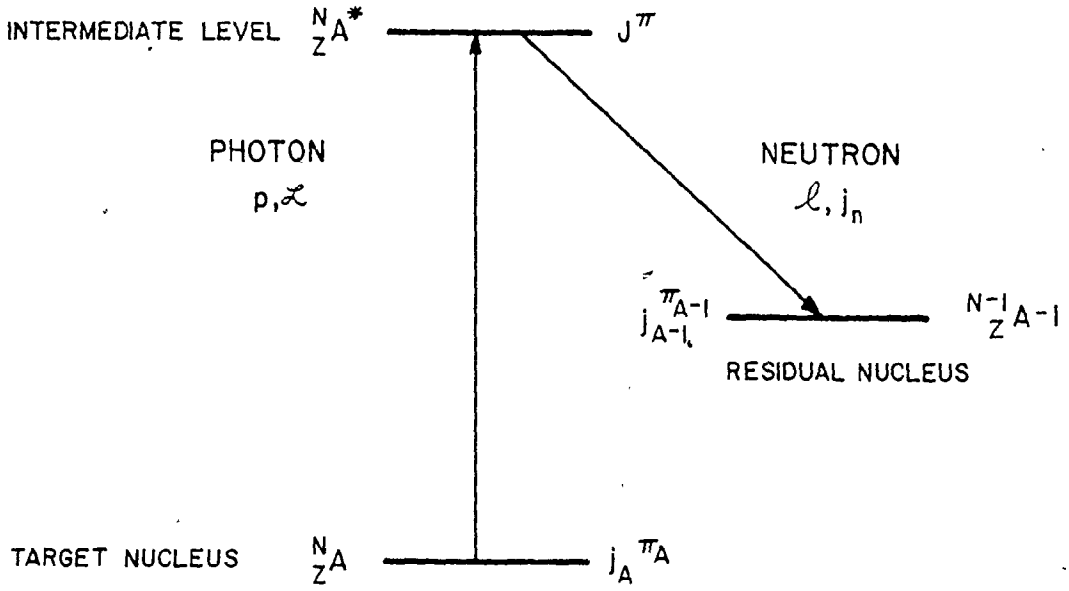

$j^{\pi_A}_A$ - spin and parity of the target nucleus (0^+)

p - nature of the excitation (E or M)

$\mathcal{L}$ - photoexcitation multipolarity

J^{π} - spin and parity of the intermediate level

ℓ - neutron orbital angular momentum

j_n - neutron spin ($\frac{1}{2}$)

$j^{\pi_{A-1}}_{A-1}$ - spin and parity of the residual nuclear level

Figure 2.3: Schematic of a Photoneutron Transition

There are several permitted reaction channels which contribute to a single photoneutron transition: there are different modes of photoexcitation (pL) which can lead to different intermediate levels J^{π}; neutrons of different orbital angular momentum may be emitted; and two channel spins are possible for each transition. Some restrictions on the quantum numbers must also be considered. The spin and parity of the target nucleus and the neutron spin are known, and only certain photoexcitations are considered (E1, E2 and M1). The remaining quantum numbers have other restrictions based on the rules governing parity and the addition of angular momenta. These restrictions are:

1. $J = L$, since the target nucleus is 0^+.
2. $\pi = -\pi_A \, (-1)^{p+L}$.
3. $|L-s| \leq \ell \leq L+s$.
4. ℓ is even if $\pi_{A-1} = \pi$,
   ℓ is odd if $\pi_{A-1} = -\pi$.

Thus, the nature and multipolarity of the photoexcitation determines uniquely the spin and parity of the intermediate level, and whether the neutrons are odd or even ℓ.

The quantum numbers <pLℓs> thus define uniquely

the permitted reaction channels for a given transition, specified by the photon energy and energy level of the residual nucleus. In Figure 2.4 the permitted reaction channels are shown for a residual nucleus of spin and parity $\frac{1}{2}^-$. For E1 excitation, the intermediate level is 1^- and neutrons of ℓ=0 or 2 (s and d-wave) are emitted. M1 excitation leads to a 1^+ intermediate level and ℓ=1 neutrons (p-wave); and for E2, J^π is 2^+ and ℓ can be 1 or 3 (p and f-wave). Channel spins of 0 or 1 are possible; but for s=0, only the <M1 p0> channel is non-zero because of the restrictions on ℓ. Thus there are six possible reaction channels <pLℓs> : <E1s1> <E1d1> <M1p0> <M1p1> <E2p1> and <E2f1> . The neutron orbital angular momentum is represented by the appropriate convention; s,p,d or f for ℓ = 0,1,2 or 3.

Interference between the different reaction channels is responsible for the angular variation of the differential cross-section, which can be expanded in terms of the interference between pairs of reaction channels of the same channel spin:

$$\frac{d\sigma}{d\Omega}(\Theta) \propto \sum_{\nu} \sum_{t_1 t_2} A_{t_1 t_2 \nu} \, \mathrm{Re}\left(\langle R_{t_1} \rangle^* \langle R_{t_2} \rangle \right) P_\nu(\cos\Theta)$$

$$= \sum_{\nu} a_\nu P_\nu(\cos\Theta) \quad , \qquad 2.8$$

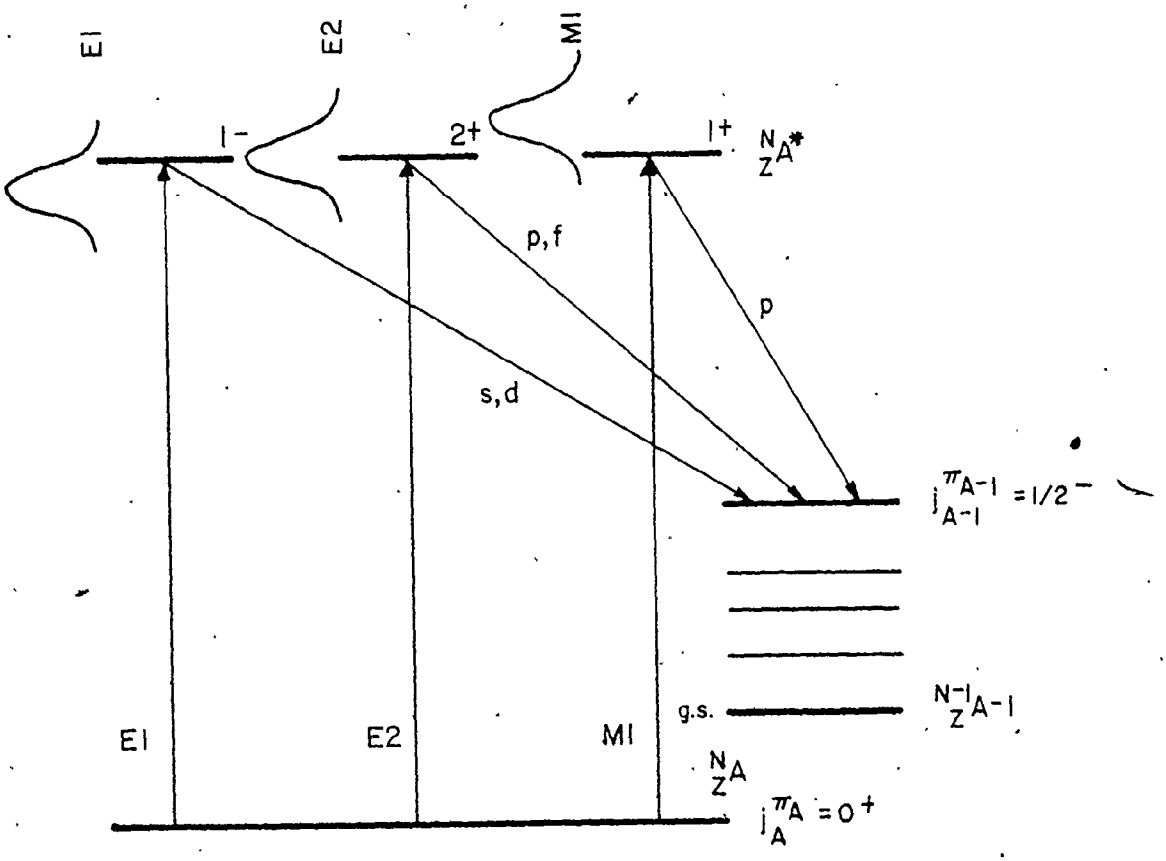

Figure 2.4: Interference between reaction Channels.
The transition from a 0^{+} target level to a $\frac{1}{2}^{-}$ residual level is shown assuming closely spaced E1, E2 and M1 levels of energy E_{γ}.

where $P_\nu(\cos\Theta)$ are the Legendre Polynomials,

$\langle R_{t_1} \rangle$ and $\langle R_{t_2} \rangle$ are the amplitudes of the matrix elements of channels t_1 and t_2, and

$A_{t_1 t_2 \nu}$ are the angular distribution coefficients.

Here, the coefficients a_ν are summed over all pairs of reaction channels for a given order ν and are also referred to as angular distribution coefficients, since they are the coefficients deduced from the experiment. The angle Θ is the photoneutron emission angle in the centre of momentum system, which is nearly equal to the angle in the laboratory system for the photon energies of this experiment. The maximum value of ν is 4 if only E1,E2 and M1 excitations are allowed, since ν is restricted by $\max(|\ell_1-\ell_2|, |L_1-L_2|) \leq \nu \leq \min(\ell_1+\ell_2, L_1+L_2)$.

2.9

Also, $\ell_1+\ell_2+\nu$ must be odd.

The expression for the differential cross-section is

$$\frac{d\sigma}{d\Omega} = \frac{\lambda_\gamma^2}{2(2j_A+1)} \sum_{t_1,t_2} \frac{(-1)^{s-j_A-1}}{4} (-1)^{p_1+p_2}$$

$$\times \mathrm{Re}\{\langle \ell s \varepsilon' | R_1 | p_1 L_1 \varepsilon \rangle^* \langle \ell_2 s \varepsilon' | R_2 | p_2 L_2 \varepsilon \rangle\}$$

$$\times \sum_{\nu=0}^{4} i^{\ell_1-\ell_2-\nu} Z(\ell_1 L_1 \ell_2 L_2; s\nu)$$

$$\times Z_\gamma(L_1 L_1 L_2 L_2; j_A \nu) P_\nu(\cos\Theta) , \qquad 2.10$$

where

$2\pi\lambda\!\!\!^{-}_{\gamma}$ is the centre of mass wavelength of the photon,

ε,ε' are quantum numbers describing the internal structure of the initial and final nuclear states,

Z and Z_γ are vector coupling coefficients, and the summation is over $p_1, p_2, L_1, L_2, \ell_1, \ell_2$ and s.

The vector coupling coefficients can be expressed in terms of 3-j and 6-j symbols; so that, the cross-section can be written as:

$$\frac{d\sigma}{d\Omega} = \frac{\lambda_\gamma^2}{8(2j_A+1)} \sum_{t_1 t_2} B_{t_1 t_2} \mathrm{Re}\{\langle p_1 L_1 \ell_1 s\rangle^* \langle p_2 L_2 \ell_2 s\rangle\}, \quad 2.11$$

where,

$$B_{t_1 t_2} = (-1)^{s-j_A-1}(-1)^{p_1+p_2} \times \sum_\nu [(2\ell_1+1)(2\ell_2+1)]^{\frac{1}{2}}$$

$$\times [(2L_1+1)(2L_2+1)]^{3/2} (2\nu+1)$$

$$\times \begin{pmatrix} \ell_1 & \ell_2 & \nu \\ 0 & 0 & 0 \end{pmatrix} \begin{pmatrix} L_1 & L_2 & \nu \\ -1 & 1 & 0 \end{pmatrix}$$

$$\times \begin{Bmatrix} \ell_1 & L_1 & s \\ L_2 & \ell_2 & \nu \end{Bmatrix} \begin{Bmatrix} L_1 & L_1 & j_A \\ L_2 & L_2 & \nu \end{Bmatrix} P_\nu(\cos\Theta)$$

$$= \sum_\nu A_{t_1 t_2} P_\nu(\cos\theta) \quad . \quad 2.12$$

Angular distribution coefficients may be calculated for any combination of $j_A^{\pi A}$ and $j_{A-1}^{\pi A-1}$, and are tabulated by Carr and Baglin (Ca71) for values of $j_A = {}^1/_2$, ${}^3/_2$ and ${}^5/_2$ of both parities. The contributions from interference between identical channels $t_1 = t_2$ must be multiplied by 2.

In Appendix II, the angular distribution coefficients for all residual levels with negative parity, up to $j = {}^7/_2^-$ are shown. These coefficients are valid for all observed transitions except one which involved a ${}^5/_2^+$ level in ^{207}Pb. The coefficients were either taken from (Ca71) or calculated using the above expressions.

Determining the angular distribution coefficients $A_{t_1 t_2 \nu}$ is straightforward but the complex matrix element amplitudes cannot be calculated directly. Even for the simplest case, with $j_A^{\pi A} = 0^+$ and $j_{A-1}^{\pi A-1} = {}^1/_2$, there are six matrix elements each with a magnitude and phase factor. Some assumptions regarding the matrix element amplitudes must therefore be made.

2.2.2 REACTION MATRIX ELEMENTS

The reaction matrix elements $\langle \ell \; s \; \varepsilon' | R | pL\varepsilon \rangle$ are complex amplitudes which cannot be determined exactly. Even elaborate fitting techniques can not be used to determine them uniquely because of the large number of unknowns in any transition.

The large number of matrix elements in the expansion of the cross-section can be reduced by considering E1-E2 or E1-M1 mixing, ignoring E2-M1 or three-way admixtures. This is reasonable because the E1 strength on the low energy tail of the Giant Dipole Resonance is well established, and a high resolution study (Ho79) up to 8.4 MeV showed that the strongest single level resonances were E1 in nature. Thus in the present work the E1-M1 and E1-E2 cases are treated separately when comparing to the experimental results.

If the interaction is considered to be indirect, the coupling between the photoexcitation and neutron emission parts of the matrix element may be weak, and the amplitude can be separated into an entrance and exit channel:

$$\langle \ell\ s\ \varepsilon' \,|R|\, p\ L\ \varepsilon \rangle = \langle p\ L\ \ell\ s \rangle = \langle pL \rangle \langle \ell s \rangle \quad . \quad 2.13$$

The quantum numbers ε' and ε describing the internal nuclear structure will be omitted in any further discussion, since nothing about their nature will be inferred. Since the photon energies are such that the excitation of the nucleus is collective, and since the direct model alone cannot predict the observed photoneutron distributions for some photon energies, the uncoupling of the matrix element should be a reasonable approximation.

A further simplification is made by defining the mixing ratios of the E2:E1 and the M1:E1 strengths:

$$\alpha = \frac{\langle E2\rangle^2}{\langle E1\rangle^2} \qquad 2.14$$

$$\beta = \frac{\langle M1\rangle^2}{\langle E1\rangle^2} \qquad 2.15$$

Associated with these mixing ratios are the phase factors

$$\langle E2\rangle = |\langle E1\rangle| \sqrt{\alpha}\, e^{i\delta} \qquad 2.16$$

$$\langle M1\rangle = |\langle E1\rangle| \sqrt{\beta}\, e^{i\eta} \; . \qquad 2.17$$

The determination of α and β which indicate the extent of E1:E2 or E1:M1 admixtures at various photon energies is the ultimate goal of this work.

The matrix elements of the exit channel $\langle \ell s \rangle$ define the configuration of the residual nucleus and the neutron. They too are complex amplitudes. For a given entrance channel, in the case where $\ell_1 = \ell_2$ in equations 2.11 and 2.12, the cross-section is of the form

$$\frac{d\sigma}{d\Omega}(pL\nu) = \sum_{\ell} \frac{d\sigma_{\ell}}{d\Omega} = \lambda^2 f(p,L,\nu) \sum_{\ell} \{(2\ell+1) \langle \ell s \rangle^2 \}. \qquad 2.18$$

This can be compared to the expression for neutron resonance scattering

$$\sigma_{\ell}^{\ell\pm\frac{1}{2}} = \pi\lambda^2(2\ell+1)T_{\ell}^{\ell\pm\frac{1}{2}}. \qquad 2.19$$

Then , the matrix elements $\langle \ell s \rangle^2$ could be considered to be related to neutron transmission probabilities $T_{\ell}^{\ell\pm\frac{1}{2}}$ where the plus or minus sign depends on the channel spin s. Calculations of these transition probabilities, which are functions of the centre of mass energy and the mass of the residual nucleus, have been done using a Perey-Buck optical model potential and are tabulated by Auerbach and Perey (Au62). Curves of the $T_{\ell}^{\ell\pm\frac{1}{2}}$ for s,p,d and f wave neutrons are shown in Figure 2.5 as a function of centre of mass energy for the ^{207}Pb residual nucleus. Since the total energy of the neutron and the recoiling nucleus is En $(\frac{A}{A-1})$, the centre of mass energy is essentially equal to the neutron energy En. To simplify the angular expansions, the matrix element magnitudes of the exit channel are assumed to be proportional to the corresponding transition probability

$$\langle \ell s \rangle^2 \propto T_{\ell}^{\ell\pm\frac{1}{2}} \qquad 2.20$$

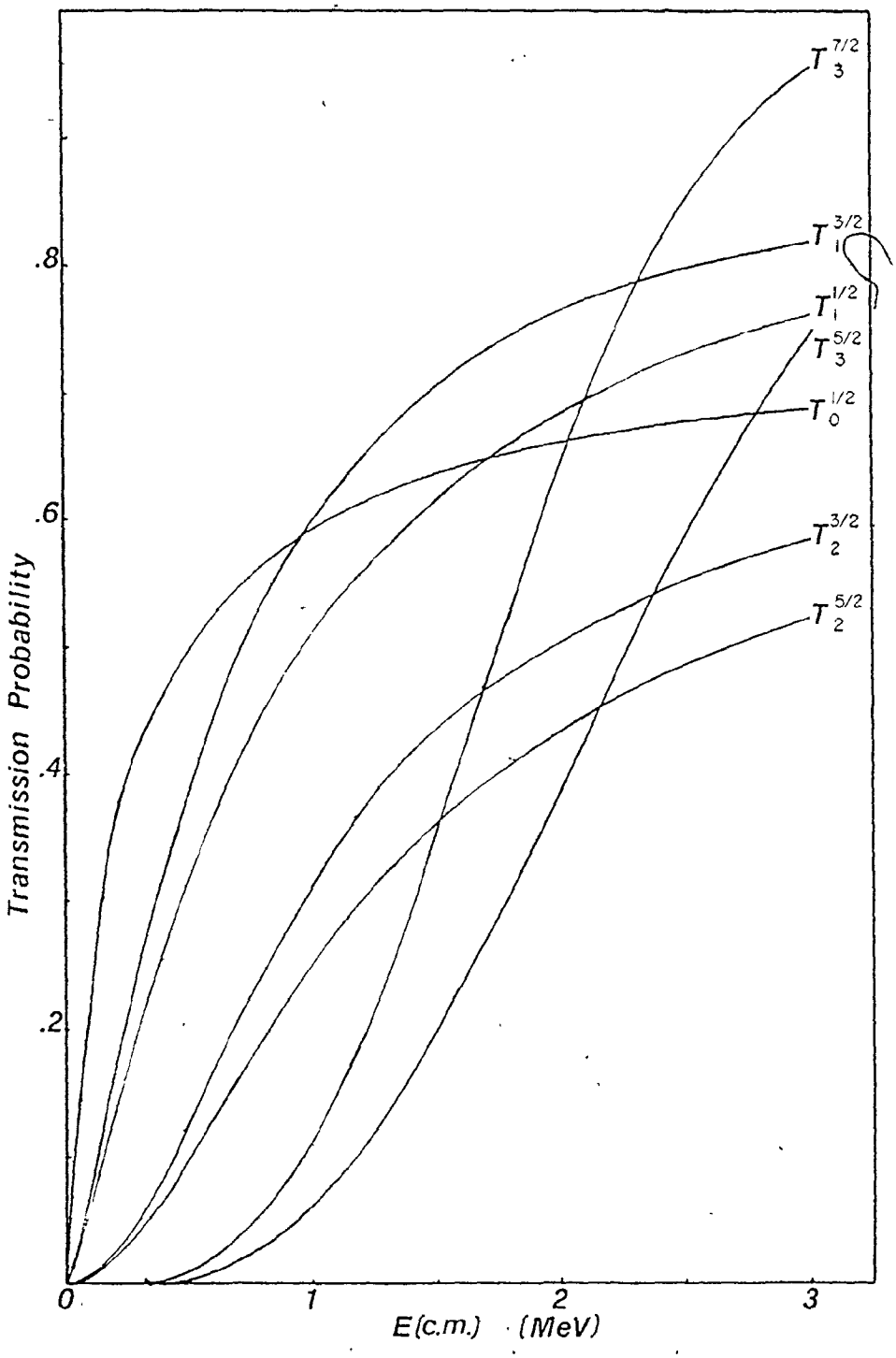

Figure 2.5

Neutron Optical Model Transition Probabilities for A=207 (Au62)

This assumption considers only the ground state potential and may not be as valid for transitions to excited states of the residual nucleus.

There is also a phase shift factor associated with the matrix element amplitude of the exit channel:

$$<\ell s> = (T_{\ell}^{\ell \pm \frac{1}{2}})^{\frac{1}{2}} e^{i\phi_{\ell}} \quad , \qquad 2.21$$

where ϕ_{ℓ} is the phase angle. For interference between exit channels,

$$<\ell_1 s> <\ell_2 s> = (T_{\ell_1}^{\ell_1 \pm \frac{1}{2}} T_{\ell_2}^{\ell_2 \pm \frac{1}{2}})^{\frac{1}{2}} e^{i\Delta_{\ell_1 \ell_2}} . \qquad 2.22$$

As an approximation, phase angles for hard sphere neutron scattering are used (Ho79). These phase angles, ϕ_{ℓ}, can be found by solving the Schrödinger wave equation for a neutron in a hard sphere potential (Ly68). The outgoing and ingoing solutions are

$$O_{\ell}(r) = - kr\, n_{\ell}(kr) + i\, kr\, j_{\ell}(kr) \qquad 2.23a$$

$$I_{\ell}(r) = - kr\, n_{\ell}(kr) - i\, kr\, j_{\ell}(kr) \qquad 2.23b$$

where $j_{\ell}(kr)$ and $n_{\ell}(kr)$ are spherical Bessel and Neumann functions respectively, and k is the centre of mass wave number

$(\hbar^{-1})\sqrt{2mE}_{cm}$. The shift factor is the real part of the logarithmic derivative of the outgoing wave evaluated at the nuclear radius a,

$$\phi_\ell = \mathrm{Re}\left(\frac{kr}{O_\ell} \frac{dO_\ell}{d(kr)} \right)_{r=a} . \qquad 2.24$$

The nuclear radius is determined by the off-resonance neutron scattering cross-section, and an expression for the radius is given by (Ho79)

$$a = 1.4\ (A^{1/3} + 1)\ \ \mathrm{fm} . \qquad 2.25$$

The expressions for the phase angles for $\ell \leq 3$ are (Ma63):

$$\text{s-wave} \qquad \phi_0 = -\ \rho \qquad 2.26a$$

$$\text{p-wave} \qquad \phi_1 = -\ \rho + \frac{\pi}{2} - \cot^{-1}(\rho) \qquad 2.26b$$

$$\text{d-wave} \qquad \phi_2 = -\ \rho + \pi - \cot^{-1}\left(\frac{\rho^2-3}{3\rho}\right) \qquad 2.26c$$

$$\text{f-wave} \qquad \phi_3 = -\ \rho + \frac{3}{2}\pi - \cot^{-1}\left(\frac{\rho(\rho^2-15)}{6\rho^2-15}\right), \qquad 2.26d$$

where $\rho = ka$. There is an ambiguity in the ϕ_ℓ values since the inverse cotangent of a number has two values which

differ by π. A value for each angle was chosen which gave the correct sign of the a_2 term in the angular distributions. The choice for each ϕ_ℓ was consistent in all transitions. The phase angles, which are smooth functions of neutron energy, assuming a does not vary, are shown in Figure 2.6 for the residual nucleus ^{207}Pb.

2.2.3 THE ANGULAR DISTRIBUTION FOR $^{\pi A-1}_{jA-1} = \frac{1}{2}^-$

As an example, the cross-section for this transition can be obtained from equation 2.8, using the angular distribution coefficients $A_{t_1 t_2 \nu}$ from Appendix II , and the matrix elements from the assumptions of section 2.2.2. The expression is in terms of the coefficients a_ν, where

$$a_\nu = \sum_{t_1, t_2} A_{t_1 t_2 \nu} \, \mathrm{Re}\{ \langle R_{t_1} \rangle^* \langle R_{t_2} \rangle \} . \qquad 2.27$$

Using the real part of the interference of the matrix elements reduces the factor $e^{i\delta} e^{i\Delta_{\ell_1 \ell_2}}$ to $\cos(\delta + \Delta_{\ell_1 \ell_2})$ if only E1-E2 mixing is assumed. A constant term in each coefficient is omitted since the ratios of the a_ν's will be used to determine the mixing ratio α and the phase angle δ. The coefficients up to $\nu=3$ are listed here; the $\nu=4$ term is omitted because of the large errors in determining a_4 in the experiment.

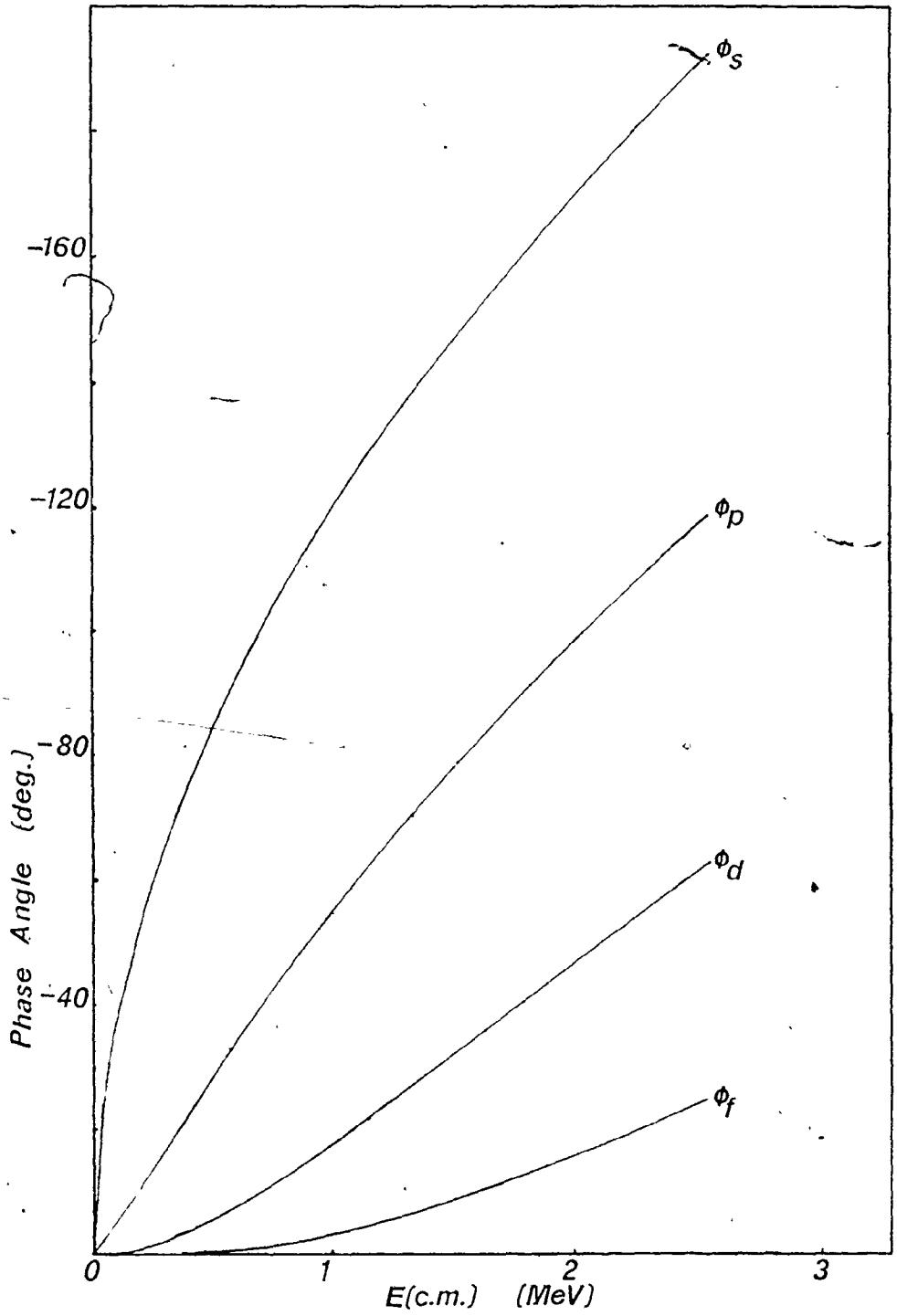

Figure 2.6

Hard Sphere Scattering Phase Angles for A = 207, r = 9.68 fm. (Ma63)

Thus, for a $\frac{1}{2}^-$ state of the residual nucleus, assuming E1-E2 mixing, the expressions for the angular distribution coefficients are:

$$a_0 = 3(T_0^{1/2} + T_2^{5/2}) + 5\alpha\,(T_1^{3/2} + T_3^{7/2}) \qquad 2.28a$$

$$a_1 = \sqrt{\alpha}\{9.487(T_0^{1/2}T_1^{3/2})^{1/2}\cos(\delta+\Delta_{sp}) - 1.342(T_2^{5/2}T_1^{3/2})^{1/2}\cos(\delta+\Delta_{dp}) + 9.859(T_2^{5/2}T_3^{7/2})^{1/2}\cos(\delta+\Delta_{df})\} \qquad 2.28b$$

$$a_2 = 4.243(T_0^{1/2}T_2^{5/2})\cos(\Delta_{sd}) - 1.5T_2^{5/2} + \alpha(1.5T_1^{3/2} + 2.857T_3^{7/2} - 1.75(T_1^{3/2}T_3^{7/2})^{1/2}\cos(\Delta_{pf})) \qquad 2.28c$$

$$a_3 = \sqrt{\alpha}\{8.05(T_2^{5/2}T_1^{3/2})^{1/2}\cos(\delta+\Delta_{dp}) + 7.746(T_0^{1/2}T_3^{7/2})^{1/2}\cos(\delta+\Delta_{sf}) - 4.382(T_2^{5/2}T_3^{7/2})^{1/2}\cos(\delta+\Delta_{df})\}. \qquad 2.28d$$

Values of a_0, a_1, a_2 and a_3 are determined experimentally from the angular distribution measurements. Using the assumptions described in this section, the neutron transmission probabilities and phase angles can be chosen from the curves in Figures 2.5 and 2.6. There are three unknowns in these expressions, one of which is the omitted constant of proportionality which can be

eliminated by considering the ratios $\frac{a_1}{a_0}$, $\frac{a_2}{a_0}$ and $\frac{a_3}{a_0}$. From these expressions, as well as the expression for the interference factor defined below, the photon multipole mixing ratio α, and phase difference δ can be inferred.

An alternative determination of these parameters involves the interference factor or asymmetry parameter for the angular distribution, defined as:

$$I(E_\gamma, E_x, \theta) = \frac{a_1 P_1(\cos\theta) + a_3 P_3(\cos\theta)}{a_0 + a_2 P_2(\cos\theta)} \qquad 2.29$$

$$= \frac{\frac{d\sigma}{d\Omega}(\theta) - \frac{d\sigma}{d\Omega}(\pi-\theta)}{\frac{d\sigma}{d\Omega}(\theta) + \frac{d\sigma}{d\Omega}(\pi-\theta)}$$

The interference factor is calculated at $\theta=55^0$ where $P_2(\cos\theta)$ is nearly zero; so that, there is no contribution from the a_2 term to the experimental error in I(Lo78).

CHAPTER 3

THE EXPERIMENTAL SYSTEM

The measurement of the angular distributions of individual photoneutron transitions requires an intense source of high energy monochromatic photons and a neutron detection system with both reasonable counting efficiency and energy resolution. Good geometry is also necessary to achieve good angular resolution.

Neutron capture on materials placed in the core of a nuclear reactor can provide intense sources of high energy photons which are essentially monochromatic. These capture gamma ray sources must be chosen to provide strong components with energies greater than the photoneutron thresholds of lead 206 and 208. The capture gamma ray spectra must also be simple to produce uncomplicated photoneutron spectra. Nickel and chromium were chosen because they had several well separated intense lines in the energy region of 7-11 MeV.

A high resolution Helium 3 fast ionization chamber was used to detect photoneutrons. It provided good counting efficiency with sufficiently high energy resolution to allow identification of individual photoneutron transitions.

Good geometry was obtained by extracting a well collimated intense photon beam using a beam port facility. The separated lead targets were placed in the beam and the neutron detector could be rotated about the sample to keep the detector-target solid angle constant at all positions. The target-detector separation was chosen to be five inches, which enabled detection of photo-neutrons emitted from 20 to 160 degrees. Smaller separations would decrease this range as well as lowering angular resolution, whereas larger distances would decrease counting efficiency due to decreased solid angle.

3.1 THE BEAM PORT FACILITY

To minimize data acquisition times, the intensity of the photon beam had to be maximized. Placing the neutron capture gamma ray source directly in the core of the nuclear reactor and extracting a beam of photons offered a considerably higher photon flux than extracting a beam of thermal neutrons and using an external capture gamma source. A first order comparison of the two methods, assuming the attenuation of thermal neutrons or high energy photons could be made approximately equal, shows that for core to photon source and source to target distances of 2 metres and a source area of 10^{-3} m^2, the factor of increased photon flux using the incore source and a source target distance of 4 m

$$f \approx \left(\frac{4\pi x 2^2}{4\pi x 4^2}\right) \times \frac{4\pi x 2^2}{10^{-3}} \approx 10^4 \quad . \qquad 3.1$$

The McMaster Nuclear Reactor is a 5 Megawatt rated pool type, light water moderated and cooled reactor using 93 percent enriched ^{235}U fuel. Power levels of 1 and 2 Megawatts were used throughout the experiment giving a thermal neutron flux of the capture gamma source of 2.5 to 5×10^{12} neutrons/cm^2/s. The source was positioned at the edge of the core adjacent to the face of the beam port as shown in Figure 3.1.

Nickel and chromium were used as the photon sources because of their strong components above the photoneutron thresholds of the lead isotopes. The source container, shown in Figure 3.2, consisted of an outer holder and an interchangeable inner box, both made from 65ST grade aluminium. The outer source holder was placed in the grid plate of the reactor in an outer fuel element position and was held in position by a guide pin. The inner source holder could be transferred to and from the outer sleeve using normal fuel handling equipment, and the source not being used could be stored indefinitely below the surface of the pool.

Each source holder contained four metal rods, 2.5 cm in diameter and 15 cm long, held vertically in a square array. One source contained 2.6 kg of 99.5% nickel (INCO 200, International Nickel Company), and the other was

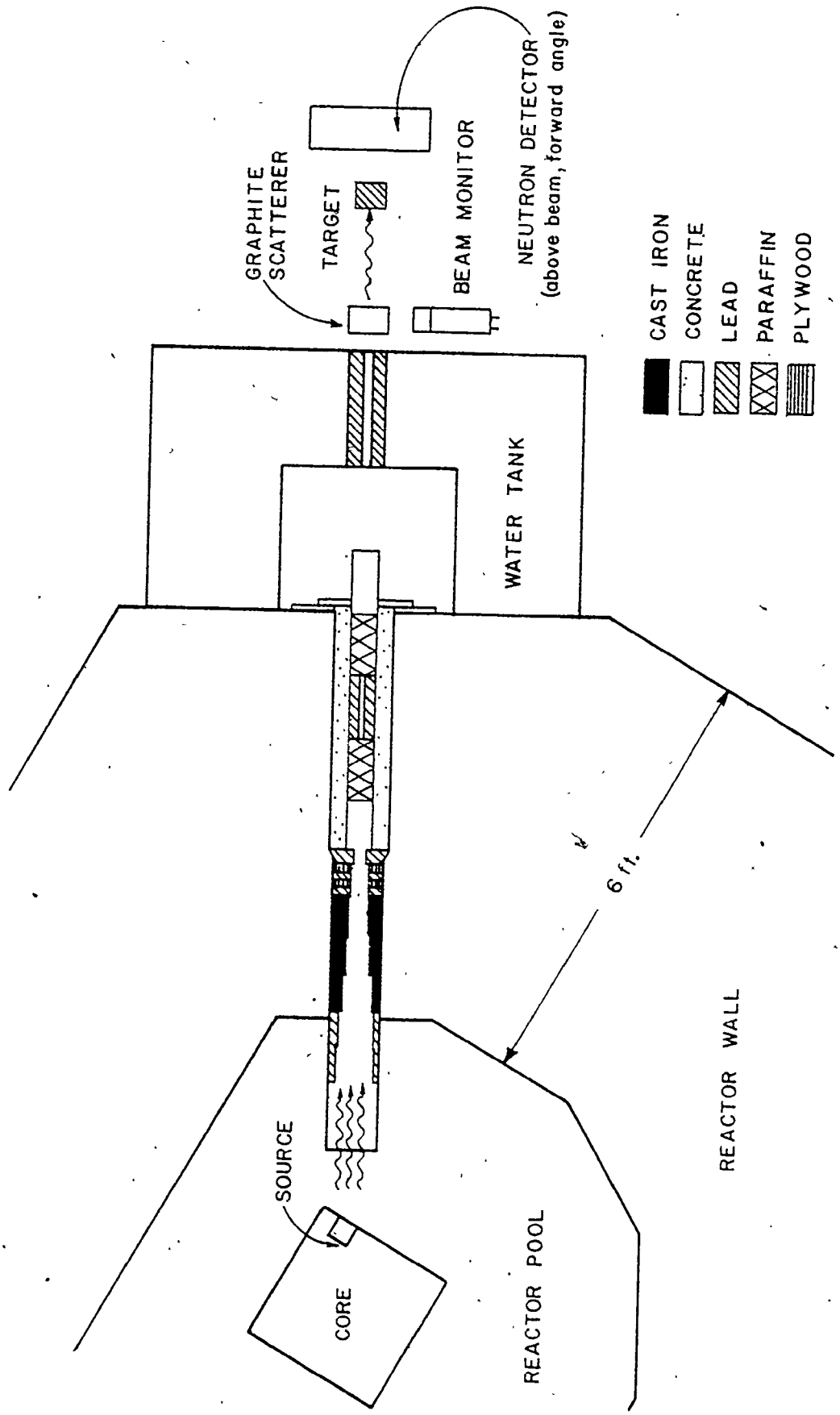

Figure 3.1: The photoneutron experimental facility.
The reactor, beam port, target and detector are shown in an overhead view.

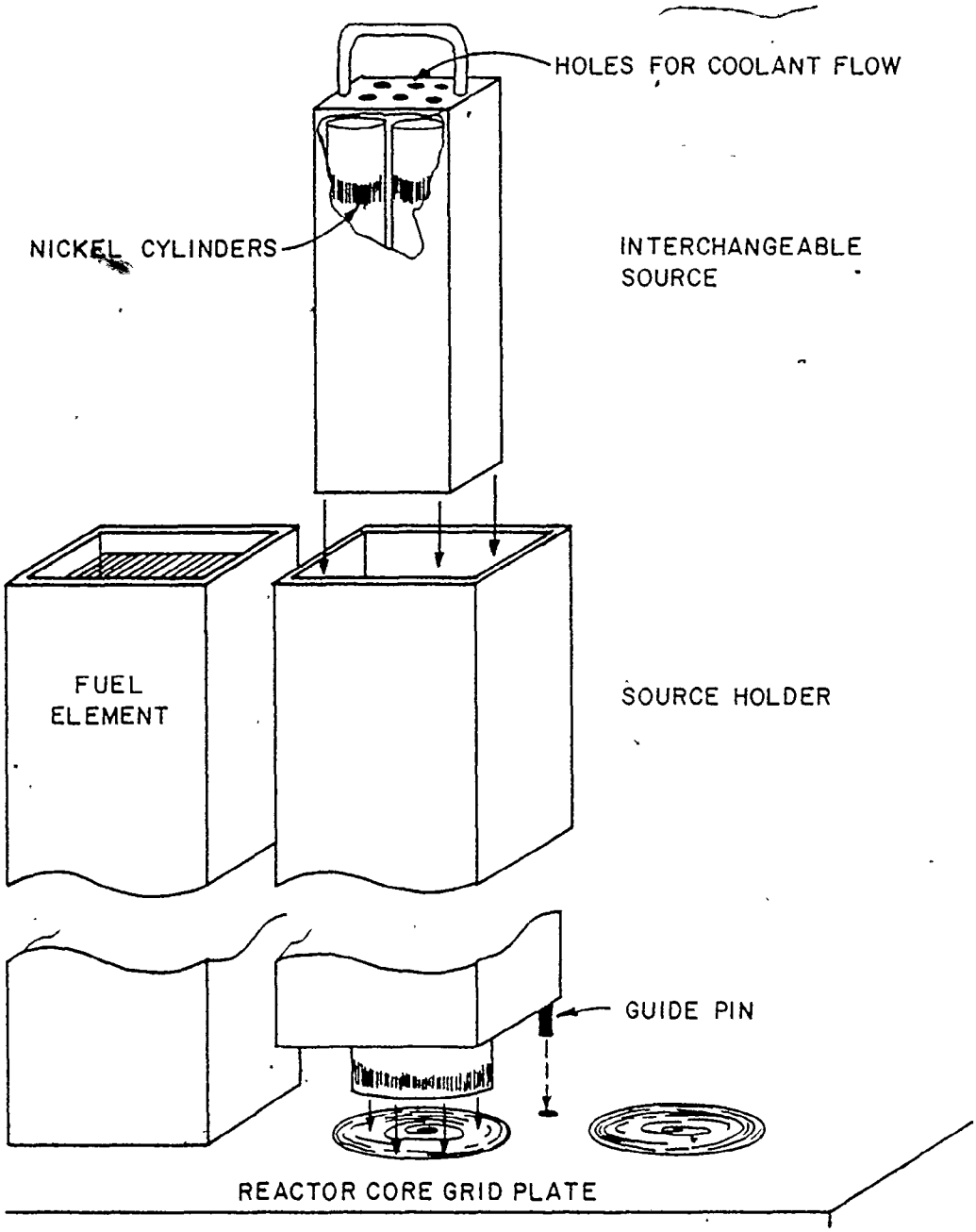

Figure 3.2
Neutron Capture Gamma Ray Source Holder.

2.1 kg of 99.6% chromium (VP Chromium-Materials Research Corporation, Orangeburg, New York). Holes were placed in the top and bottom of the source containers to allow the cooling water flowing down through the core to dissipate the heat generated in the source.

A collimated beam of photons was obtained by a series of stepped rings of iron, barytes concrete and lead, in a hollow beam port as shown in Figure 3.1. At the target position the beam diameter was 2.5 cm. Two 28 cm plugs of borated wax were placed inside the beam port to remove fast neutrons and harden the beam. Fast neutrons in the beam could scatter from the lead target to the detector producing a high energy continuum in the photoneutron spectra. As a check for high energy neutron scattering, an aluminium scatterer was placed in the lead target position and a spectrum of scattered neutrons at 40 degrees was recorded (Figure 3.3). No photoneutrons contributed to the spectrum because the Q-value for aluminiumis 13.1 MeV, well above any of the nickel photon energies. The measured rate of scattered neutrons was low, aboutone count per minute between 300 and 2500 keV or about 0.4 counts per channel per 100 minutes. No structure is seen in the scattered neutrons, and since the neutron scattering cross-sections are of a similar magnitude for lead and aluminum, there

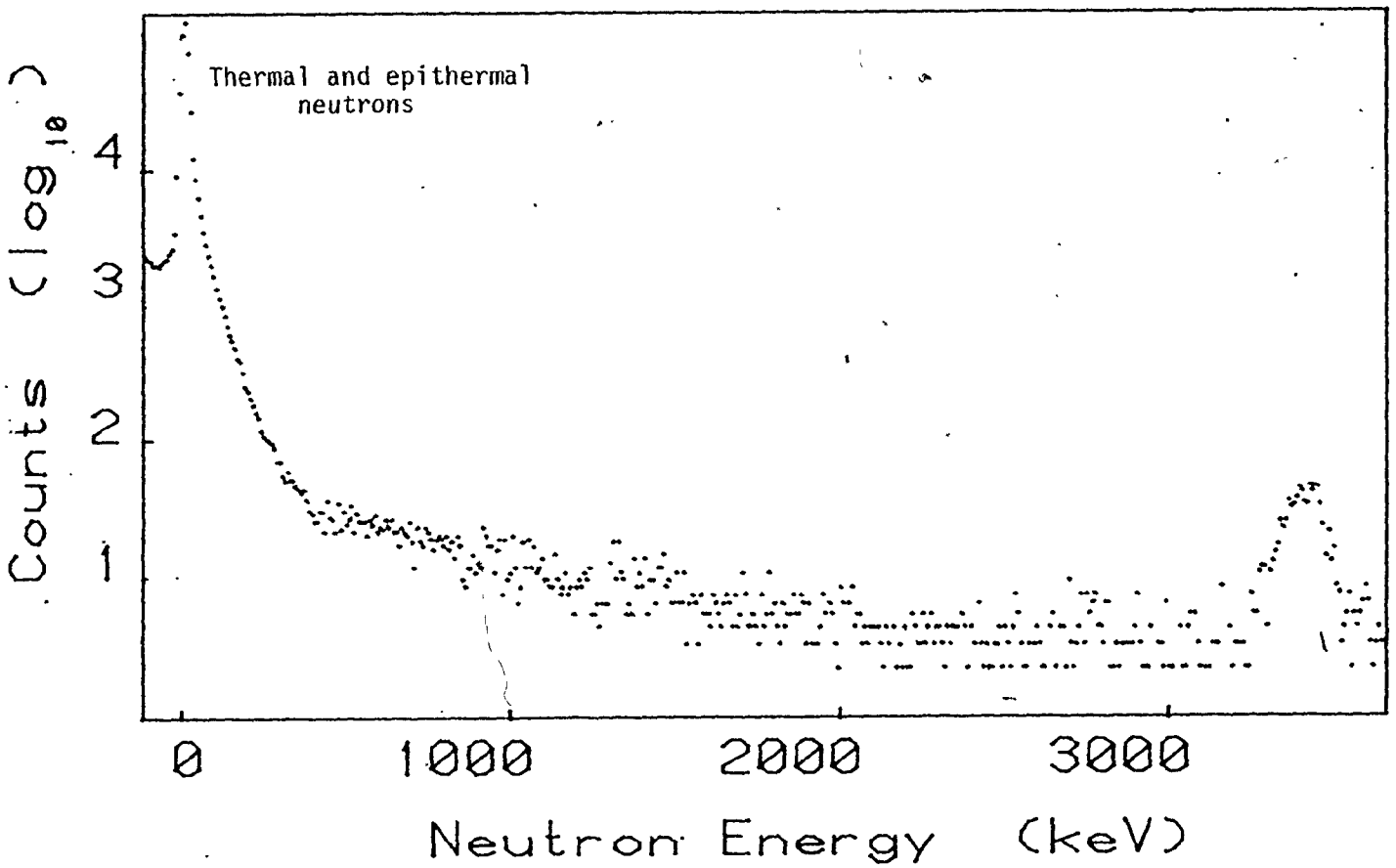

Figure 3.3 : Neutron Spectrum with Aluminium Target in Beam.
The photon source is nickel, detector setting is 40 degrees, counting time is 46 hr.
This spectrum is representative of background, since the (γ,n) threshold for Aluminium is 11.3 MeV. Also visible is the high energy structure peculiar to the detector.

should be no significant contribution of scattered neutrons to the photoneutron spectra.

In all the photoneutron spectra, and also in the scattered neutron spectra of Figure 3.3, there is a large peak corresponding to thermal and epithermal neutrons. The high $^{3}He(n,p)^{3}H$ cross-section at low neutron energies is the main reason, with some contribution from ^{3}He recoils from high energy neutron scattering in the detector. There was also an intermittent source of neutrons from an adjacent beam port which could reach the detector after being thermalized and scattered. To reduce this contribution to the thermal neutron peak, a wall of borax and paraffin was placed between the detector and the adjacent beam port.

3.2 TARGET DETECTOR GEOMETRY

The targets of separated lead isotopes were placed on a tray in the photon beam directly beneath the helium-3 detector. Both targets were small metal cylinders and were obtained on loan from ERDA, Oak Ridge National Labs, Oak Ridge, Tennessee. The lead 206 target had a purity of 99.8% and a mass of 47.1 g, and the lead 208 target was 99.14% isotopically pure with a mass of 40.7 g. The isotopic analysis and physical characteristics of the targets are outlined in Table 3.1.

The positioning of the targets in the beam was important because the beam intensity was not constant over its 2.5 cm diameter, and because the targets were smaller than the beam. Any movement of the target within the beam would change the intensity of the photons incident on the target. The best position of the targets within the beam was found by maximizing the rate of photons scattered from the target into a 3.8 cm diameter NaI detector, and this position was not changed throughout each experiment. An intensity profile of the beam was made (Mc77) by scanning a photograph of the beam taken with KODAK X-ray film with a densitometer and by digitizing the exposure of the film. The resulting digitized contour plot of beam intensity is shown in Figure 3.4. Some spreading of the beam would occur due to small angle scattering from the graphite slab used for the beam monitoring.

To ensure identical target-detector geometry at all angles, a movable rotating frame was built to hold the helium-3 detector (Figure 3.5). The detector was positioned above the target with its axis horizontal and perpendicular to the beam. The cylindrical lead targets were aligned in the same direction on the axis of rotation of the detector holder. Thus, the distance from the centre of the target to any point in the detector was the

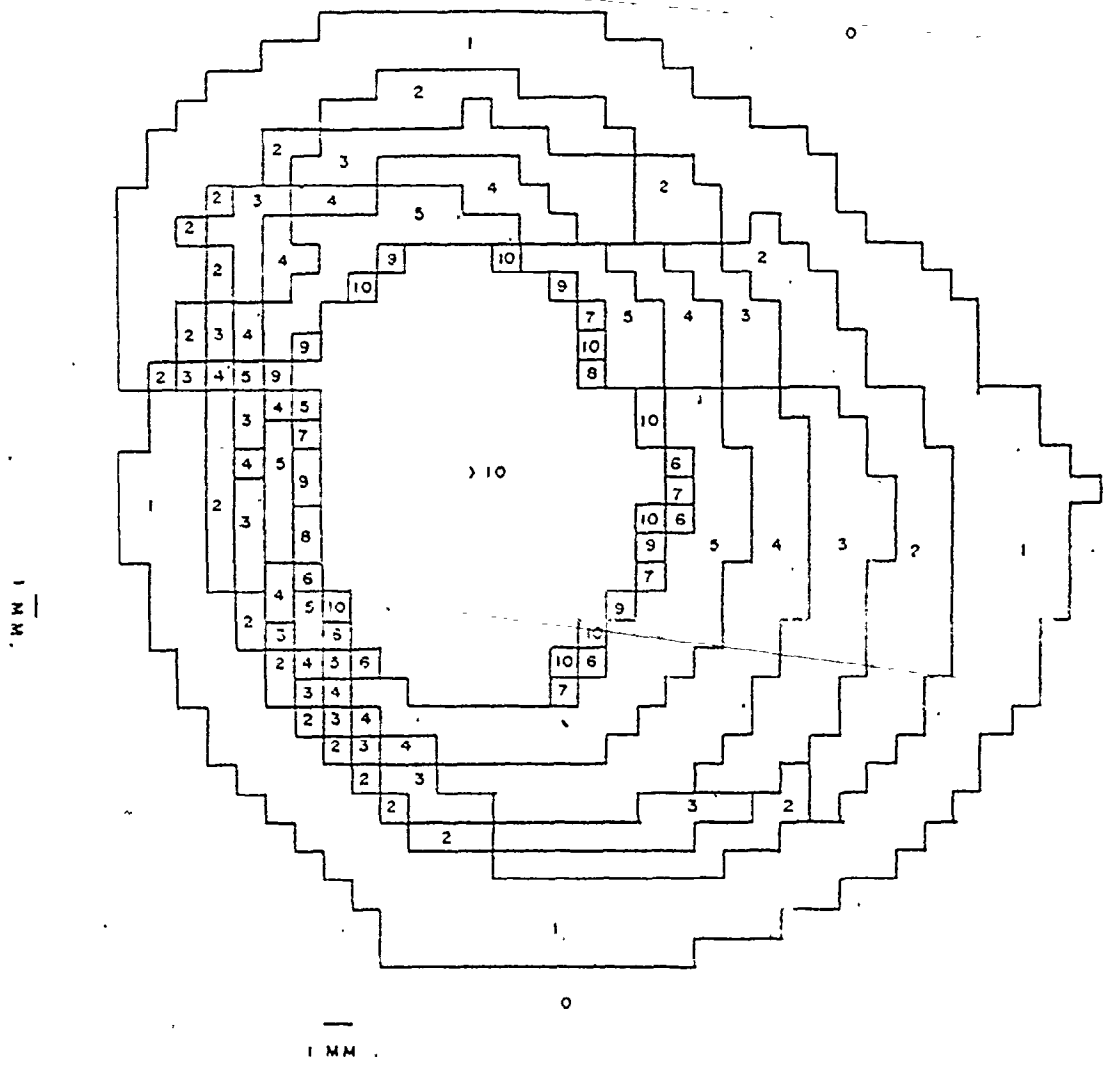

Figure 3.4 Contour Profile of the Beam Intensity
The numbers denote relative intensity as determined in Reference (Mc77).

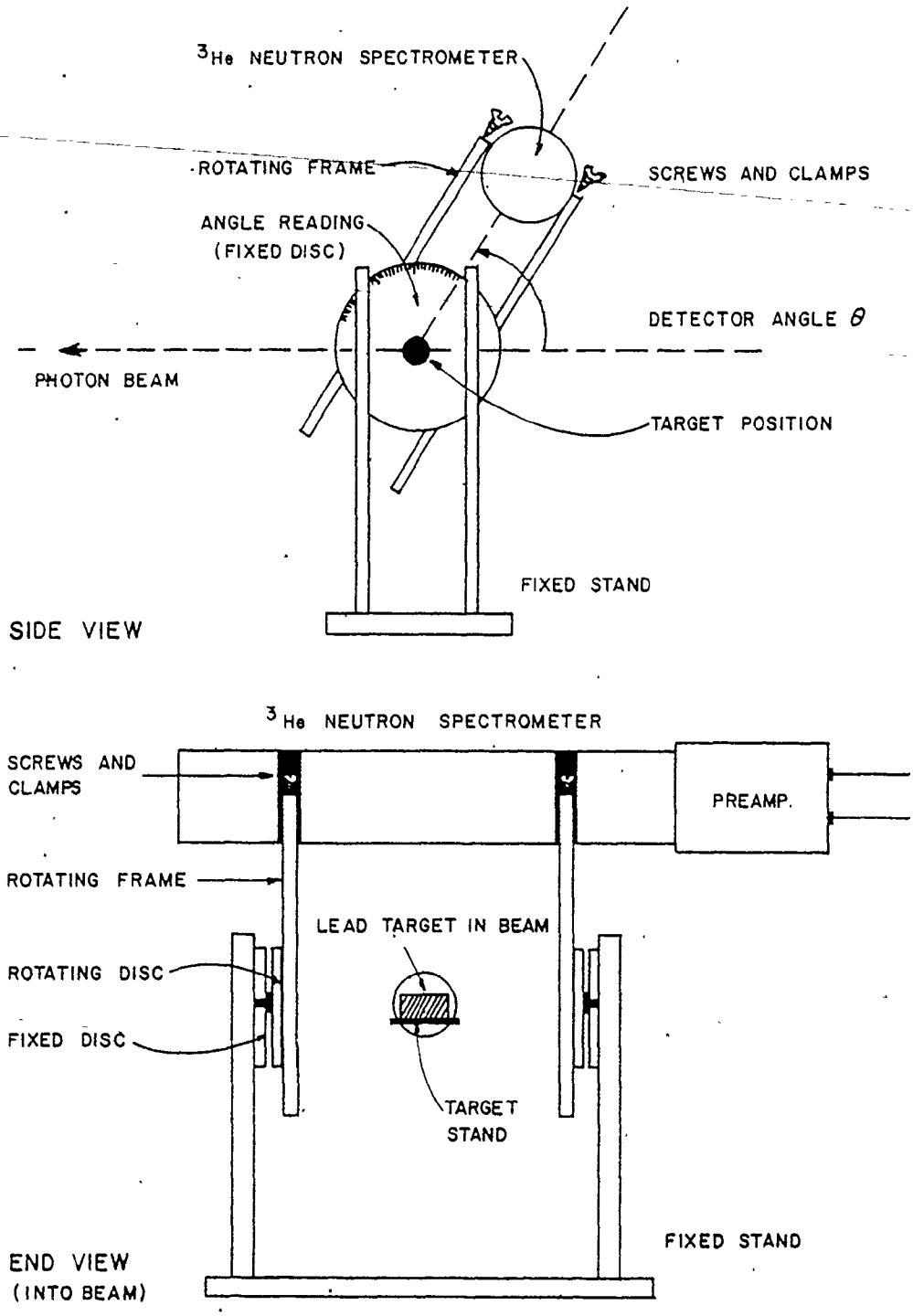

Figure 3.5

The rotatable neutron detector holder.

same at all angles. A direct reading of the angle between the beam axis and the line joining the centres of the target and detector was obtained from a protractor attached to the rotating stand. Using a target-detector separation of five inches allowed spectra to be recorded between 20 and 160 degrees. At more acute forward and backward angles, the detector would intersect the beam.

The detector could not be moved to 160 degrees because the stand supporting the lead targets obstructed it. Thus, at this angle, the lead target had to be re-positioned on a different stand. Care was taken to reproduce the target position within the beam as precisely as possible, but a small error could be introduced at this angle due to a small change in the intensity of incident photons on the target. The measurement at 160 degrees was always the first or last made in each angular distribution experiment, so the target was never moved between measurements from 20 to 140 degrees.

Because of the finite detector size, there was a spread in the angle of emission of detected neutrons. This could be reduced by a larger target-detector distance but at the expense of counting rate. The spread in neutron

emission angles was considered in the spectral analysis (section 4.4).

3.3 THE HELIUM 3 SPECTROMETER

The helium 3 detector used in this experiment made possible the high resolution investigation of the photoneutrons produced in the lead targets. Little of the theory of Helium 3 ionization chambers will be presented in this work, this having been explained in detail in previous work (Mc77). A simple explanation of the basic operation of the detector will be given specially as it relates to this work.

3.3.1 NEUTRON DETECTION

Neutrons are detected by means of a nuclear reaction between neutrons and ^{3}He gas

$$n + {}^{3}He \rightarrow p^{+} + {}^{3}H^{-} + Q$$

and by the collection of the charged reaction products through an applied voltage. There are both advantages and disadvantages of using a helium 3 detector. Among the advantages are a positive Q value (+784 keV), so that, low energy neutrons can be observed. The Q value is small allowing good energy resolution, since the actual energy resolution depends on the energy deposited in the detector

En + Q. The energy resolution was found to be 18 keV for thermal neutrons increasing to 35 keV for 2 MeV neutrons. There are no low lying excited states of ^{3}H which can be reached in the $^{3}He(n,p)$ reaction, so neutrons of a given energy will not produce extra peaks in the spectrum. The (n,p) cross-section for ^{3}He (Figure 3.6) (Ba64) is smooth showing no resonance structure up to 5 MeV, and the cross-section over the energy range of most neutrons encountered in this experiment (.3 to 3 MeV) is relatively constant. The ^{3}He spectrometer also has no competing charged particle reactions besides (n,p) for neutron energies below 4.5 MeV, the (n,d) threshold. Finally photon cross-sections of ^{3}He are very low, so pulse pile-up due to photon interactions is minimized.

There are two undesirable effects in using a ^{3}He detector. At low neutron energies (< 100 keV), the (n,p) cross-section rises dramatically resulting in a large efficiency for the detection of thermal and epithermal neutrons. This may obscure any low energy photoneutron peaks. To reduce this effect, a shield consisting of 2 mm of boron nitride between two 0.5 mm sheets of cadmium was wrapped around the detector. Secondly, the neutron elastic scattering cross-section is very high, so that events below the neutron energy can appear in the spectrum.

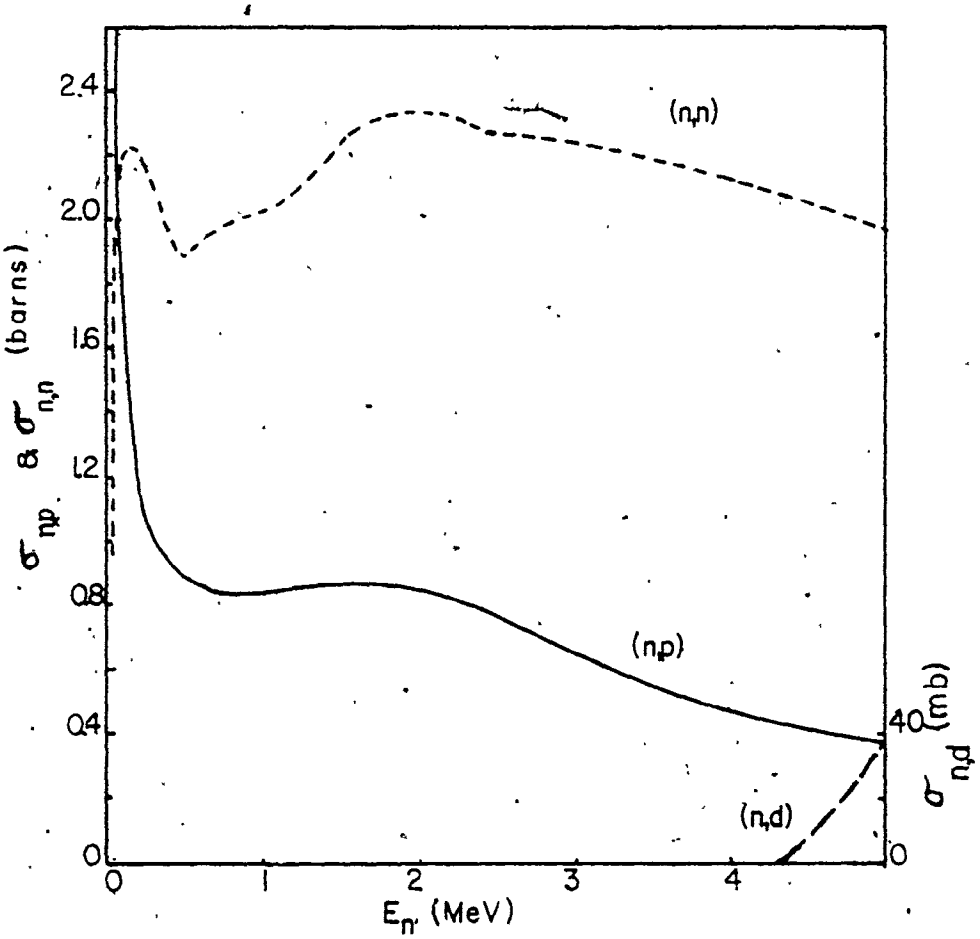

Figure 3.6

The $^{3}He(n,p)^{3}H$ cross-section.
Taken from Reference Batchelor and Parker (Ba64).

A neutron can lose between 0 and $\frac{3}{4}$ of its energy in an elastic collision with a ^{3}He atom so that an energy between 0 and $\frac{3}{4}$ En may be detected. Most of such events occur below the 764 keV energy corresponding to thermal neutrons but for En > 1.018 MeV, elastic scattering can lead to events above the thermal peak which can obscure low energy neutron groups. Detection of the elastically scattered neutrons also contribute to a low energy tail on the true peak. A combination of these drawbacks leads to a large continuous background level which rises with decreasing neutron energy.

An anomalous effect, peculiar to the detector used in this work can be seen in all spectra (Figure 3.3), even at zero reactor power or with the detector in a different building. Three peaks at 3.55, 4.30 and 4.54 ± .05 MeV, well above any observed photoneutrons, always exhibited a constant rate. A study of these anomalous peaks (Mc77) could not identify their origin; but since the events were statistical and independent of detector location, the likely origin is an unknown impurity in the detector gas or walls. Because no photoneutrons were expected in this energy range, this structure did not affect the spectral analysis.

3.3.2 CHARGE COLLECTION

A neutron with energy En interacting with ^{3}He can produce charged particles p^{+} and $^{3}H^{-}$ with total energy En + 764 keV. If these energetic particles can be stopped within the detector volume, they will produce ions and electrons which can be collected producing a voltage proportional to the energy En + 764 keV.

The electrons and ions move due to an applied electric potential towards the anode and cathode respectively. The electrons have a mobility of about 100 to 1000 times that of the heavier ions; so they tend to be collected first. The voltage induced at the anode thus increases rapidly until all the electrons have been collected($t_e \approx 1\mu s$), then increases more gradually as the slower ions reach the cathode ($t_i \approx 1ms$). The pulse eventually decreases as the preamp capacitor discharges. In order to do pulse counting the helium 3 detector is operated as a fast ionization chamber in which the clipping time is intermediate between t_e and t_i. In this type of detector the entire electron signal is collected but only a small fraction of the ion signal.

The problem with this type of detector is that the charge collected depends on the position of formation of

an ion pair. If an electron-ion pair is formed near the cathode the electron is collected by the anode and a similar charge is induced on the cathode by the nearby positive ion, so that almost the full voltage $q/_C$ appears across the counter after 1 μsec. Conversely, if the ion pair was formed near the anode the electron is collected but a charge of -q is induced on the anode as well, making the net voltage across the counter very small. This induction effect is eliminated by placing a fine mesh Frisch grid around the central anode wire at a large positive voltage. Almost all of the electrons are still collected quickly but the positive ions formed between the grid and the cathode can no longer induce a charge on the anode, resulting in a constant pulse size. Only ion-electron pairs formed in the small volume between the grid and the anode will be affected by charge induction.

The detector's cylindrical geometry makes the maximum charge collected a more weakly varying function of position of ion formation than for a parallel plate geometry. Increased electron mobility is also attained by the addition of methane gas to the detector volume. The above features combine to make the voltage pulse rise time and hence height, less dependent upon the position of ion formation.

The two products of the initial reaction, p^+ and $^3H^-$, leave a track of ions and electrons as they slow down. If the track is roughly parallel to the anode wire, the distribution in risetimes is extremely narrow for all track lengths. However, a radial track will produce a range of lower rise times which is dependent on energy. The actual voltage pulse produced by the detector is the sum of the contributions from all these ion pairs.

Thus, the detector acts as a fast ionization chamber which generates fast risetime voltage pulses with a height proportional to the energy En + 764 keV. The effect of risetime variation with track position and orientation, although minimized by the above mentioned features, can still be seen as a low energy tail on the photoneutron peaks due to incomplete charge collection. Other contributions to this low energy tail are the detection of neutrons initially elastically scattered by ^3He and events in which either the proton or triton track lie partially beyond the active detector volume. This is known as the wall effect if a particle formed inside the active volume is stopped outside, and the end effect if a particle formed outside is stopped inside. Reduction of this low energy tail is possible using risetime discrimination of the measured

events or by detection criteria more sophisticated than pulse height analysis.

3.3.3 THE FNS-I SPECTROMETER

The helium 3 detector used in this experiment was manufactured by Seforad Applied Radiation Ltd. of Emek Hayarden, Israel. Its features are shown in Figure 3.7. The cylindrical chamber had an active volume of 276 cm^3, filled with six atmospheres of ^3He gas, with three atm. of argon stopping gas and a small amount of methane to increase the electron mobility. The anode wire extended along the detector axis and was kept at +3000 volts with respect to the detector case or cathode. The anode was surrounded by a Frisch grid kept at +850 volts. Two guard electrodes in the form of cylindrical rings at either end of the anode and kept at the same voltage, were used to make the electric field more uniform across the active volume and to stop electrons formed beyond the active volume from reaching the anode.

The detector casing was stainless steel with an outer diameter of 5.08 cm and a length of 502 cm, of which 150 cm was the length of the active volume defined by the guard electrodes. To shield the detector from thermal neutrons, the casing was covered by two 0.5 mm thick

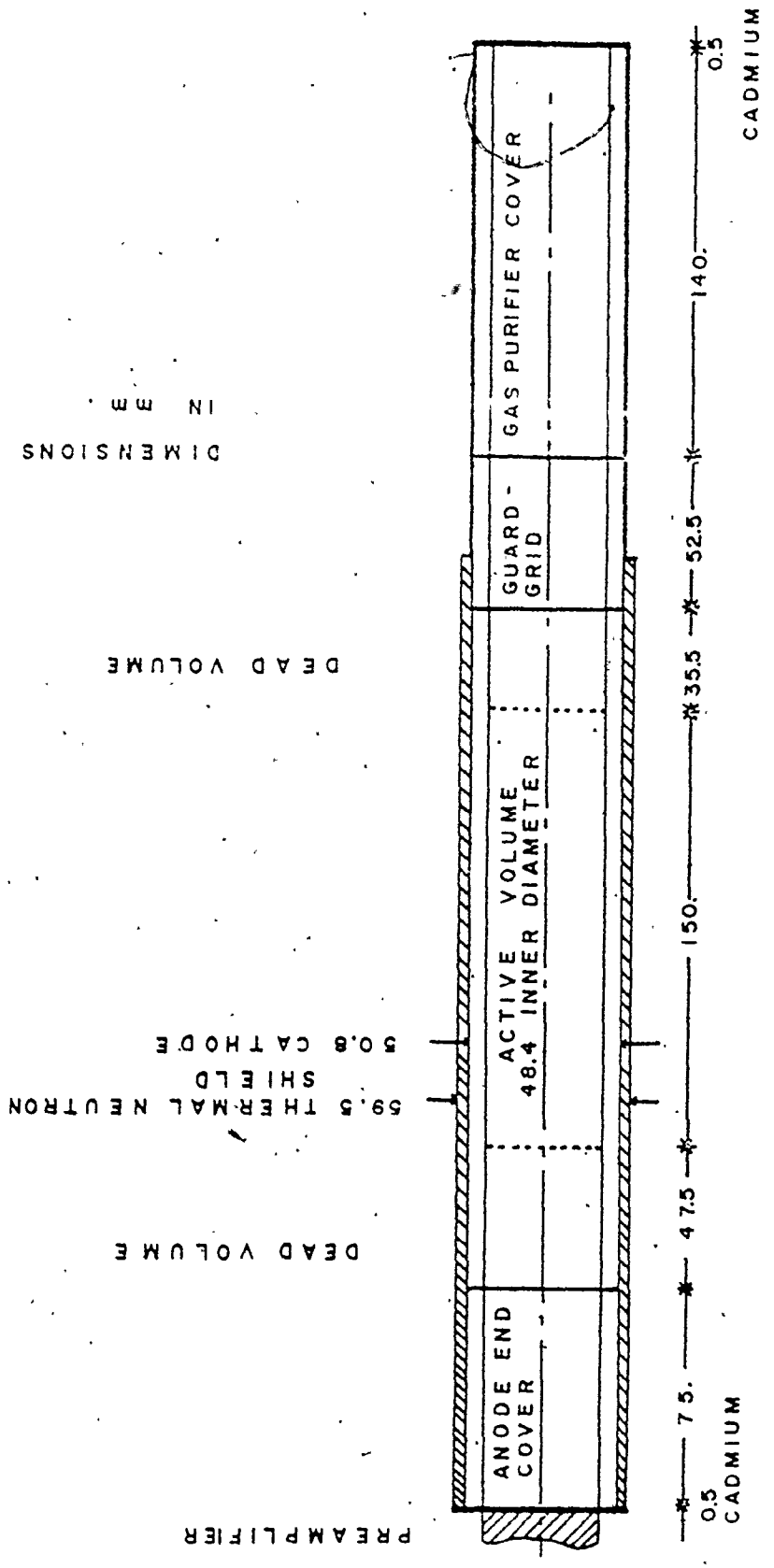

Figure 3.7 Specifications of the FNS - 1 ^{3}He Neutron Ionization Chamber

sheets of cadmium encasing 2 mm of boron nitride powder, resulting in a reduction factor of 50 to 100 in thermal neutrons with only 3 per cent attenuation of 1 MeV neutrons.

3.4 ELECTRONICS

The electronic system consisted of a preamplifier which was part of the detector, a pulse amplifier, an anode bias high voltage supply, a constant voltage pulser to monitor gain and a multichannel analyser. The system is shown in Figure 3.8.

The SR101 preamplifier was an integral part of the ^{3}He spectrometer. Its first stage, a low noise FET, integrated the collected charge from the ionizing particles. A voltage amplifier with a gain of ten in the second stage gave an output signal of similar magnitude to that of a Ge(Li) detector; so that a normal spectroscopy amplifier could be used. Preamplifier noise was responsible for an energy resolution of about 10 keV. AC coupling to the collector was necessary because of the high anode voltage.

The anode was kept at +3000 volts by an AEC 1000 high voltage supply. This voltage was divided in the detector preamplifier to keep the grid at +850 volts, rather than using a separate supply. To protect against

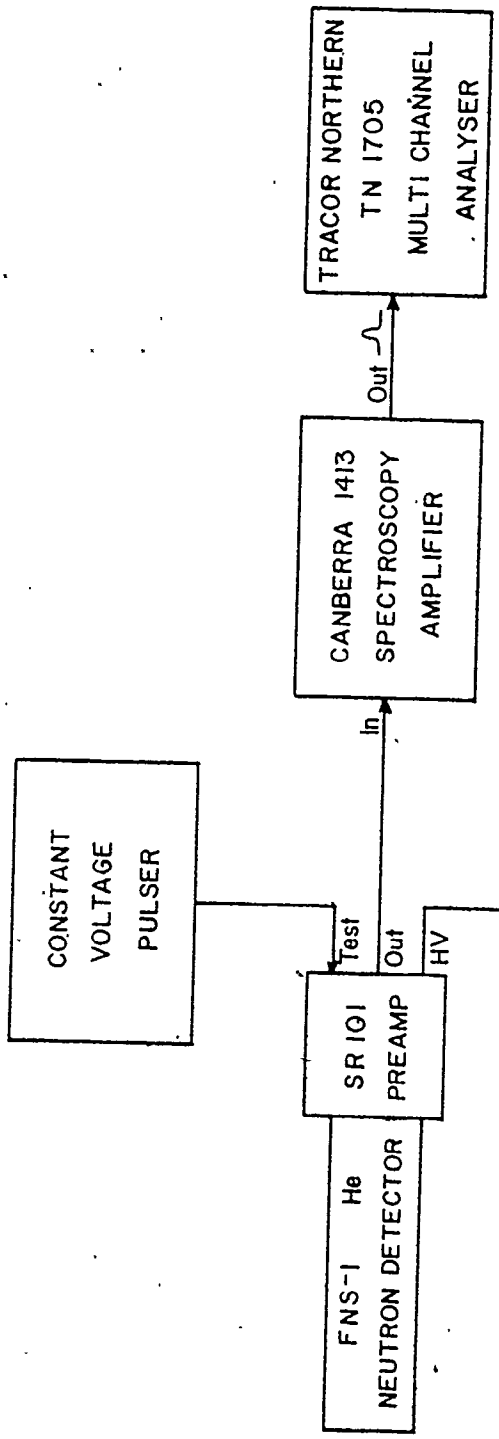

Figure 3.8
The Electronics for Neutron Counting.

damage to the preamplifier FET due to rapid voltage changes during power failures and surges, a long time constant discharge capacitor was used.

To monitor the system gain, a pulser signal was fed into the test input of the preamplifier. At a rate of five pulses per second, the pulser signals generated a large peak in the spectra at 4.7 MeV, well above the energies of the photoneutrons. Together with the large epithermal neutron peak, the pulser was used to account for and correct any shifts in gain between spectra. The shape of the pulser peak was also used to determine the extent of pulse pile-up in the photoneutron peaks. It was also used as a separate indication of dead time in the multichannel analyser.

The preamplifier signal was fed via a short cable to the input of a Canberra spectroscopy amplifier (Model 1413). The short cable was necessary to increase signal to noise ratio as well as not to increase the preamplifier discharge time by adding to its capacitance. Unipolar output with an 8 usec shaping time constant and active baseline restoration was input to a Tracor Northern multi-channel analyser, model TN1705. A 1024 channel group size was used with a gain of 8.05 keV per channel, chosen such that there were two channels at full width half maximum of the epithermal neutron peak (16 keV). Analyser dead

time was reduced by setting a low level discriminator just below the epithermal neutron peak, eliminating much of the gamma ray and helium recoil events. Live time was recorded in the first channel of the analyser. The contents of the multichannel analyser, typically a spectrum collected over a one day period, could then be transferred directly to computer memory for storage and analysis.

3.5 THE BEAM MONITOR

To determine the photoneutron reaction rates, the photon beam intensity, which changes due to fluctuations in reactor power, must be monitored for each spectrum.

Nothing in the photoneutron spectra can be used as a measure of the beam strength due to changes in the detector position, and the uncertain contribution to the various photoneutron spectral features from sources other than the photon beam.

A system to measure photons either directly in the beam or scattered from it was more reliable. Direct measurement would isolate the contributions of the various high energy photons which could produce photoneutrons in lead, but the beam intensity was too high at full reactor power. Measuring the intensity of photons scattered from the

beam was chosen instead. The system, shown in Figure 3.9, consisted of a 2.5 cm thick slab of graphite placed at the beam port exit and a shielded 1.5 inch sodium iodide detector. The mean angle of scattering of the detected photons was 90 degrees. Placing the scatterer upstream of the target eliminated the effects of moving or changing the target, which would also be a problem if the lead targets were used as scatterers. The graphite slab was kept as far away as possible from the lead target and detector to minimize forward angle Compton scattering to the detector and target. A 9 MeV photon scattered from the graphite to the lead could lose no more than 0.5 keV since the maximum scattering angle was 0.15 degrees. The graphite slab caused an attenuation of only eight percent for 9 MeV photons.

For photon energies between 7 and 11 MeV, Compton scattering and pair production are the major photon interactions and at 90 degrees, the radiation from both effects yields similar energies; 511 keV for pair production and 480 keV for Compton scattering. A window was set around these energies by putting the NaI output through an SCA to a scaler. A ^{22}Na source (511 keV) was used to set this window, which was widened to include the Compton scattered photons.

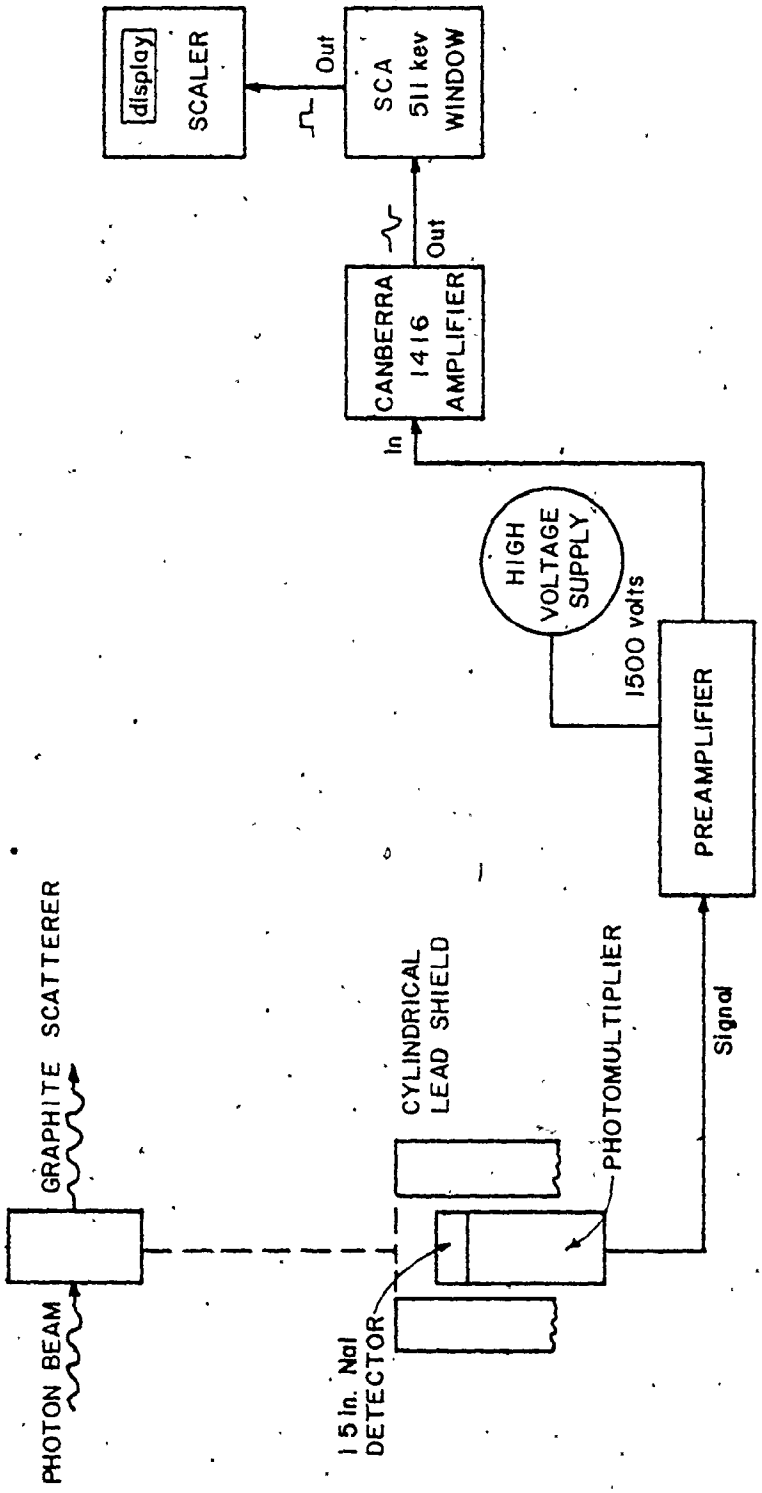

Figure 3.9
The Beam Monitor System.

About twenty percent of the counts in the window were from sources other than the graphite slab. Most of this was due to scattering or pair production from other materials such as the beam port exit pipe and, as such was also proportional to the beam strength. The background rate during a reactor shutdown was only three percent of the original intensity. Most of this would be due to radioactive ^{41}Ar in the air of the reactor building. Its half-life is 1.8 hours; so its activity is constant except after a prolonged reactor shutdown. Care was taken not to use the beam monitor for reaction rate normalization for the first few hours following a long shutdown, even though the effect on spectra acquired for one week periods was small.

CHAPTER 4

DATA ANALYSIS

Because of the nature of the experimental arrangement it was possible to investigate over thirty different photoneutron transitions in lead 206 and 208 from nickel and chromium targets. Recording photoneutron spectra at several angles allows one to obtain the angular distributions for each transition.

By comparison with theoretical angular distributions, an estimate of the extent of photon multipole mixing could be made at seven energies between 7 and 11 MeV.

Analysis of the data consisted of three main steps:

1. The acquisition of the 28 photoneutron spectra (2 targets, 2 sources, 7 angles).
2. Determination of reaction rates for all transitions at each angle.
3. Determination of the angular distribution function for each transition.

Throughout the data acquisition and for most of the analysis, a NOVA 2 minicomputer (Data General) was used. Data could be transferred from the analyser to disk

memory using a spectrum handling program in a PDP-15 computer, which acted as a link. Manipulation of the spectra stored on disk, determination of peak areas, calculation of angular distribution functions and most other analysis were done using BASIC language programming on the NOVA.. For output, both a CRT display and a teletype were used; and for visual display of data, a graphics display and an x-y plotter were used. Transfer of data to magnetic tape was also possible through the link to the PDP-15 computer. Figure 4.1 is a block diagram representation of this system.

4.1 DATA ACQUISITION

The counting rates for the experiment were low, requiring data acquisition times of the order of a week before reasonable counting statistics could be obtained in most of the observed transitions. Because of slow gain drifts in the detection system and occasional sudden jumps in the gain, it was inadvisable to count continuously for a week. Instead, spectra of a day's duration were taken and transferred from the multichannel analyser to disk memory as well as to a backup magnetic tape. If a gain jump occurred, no more than one day's counting would have to be discarded.

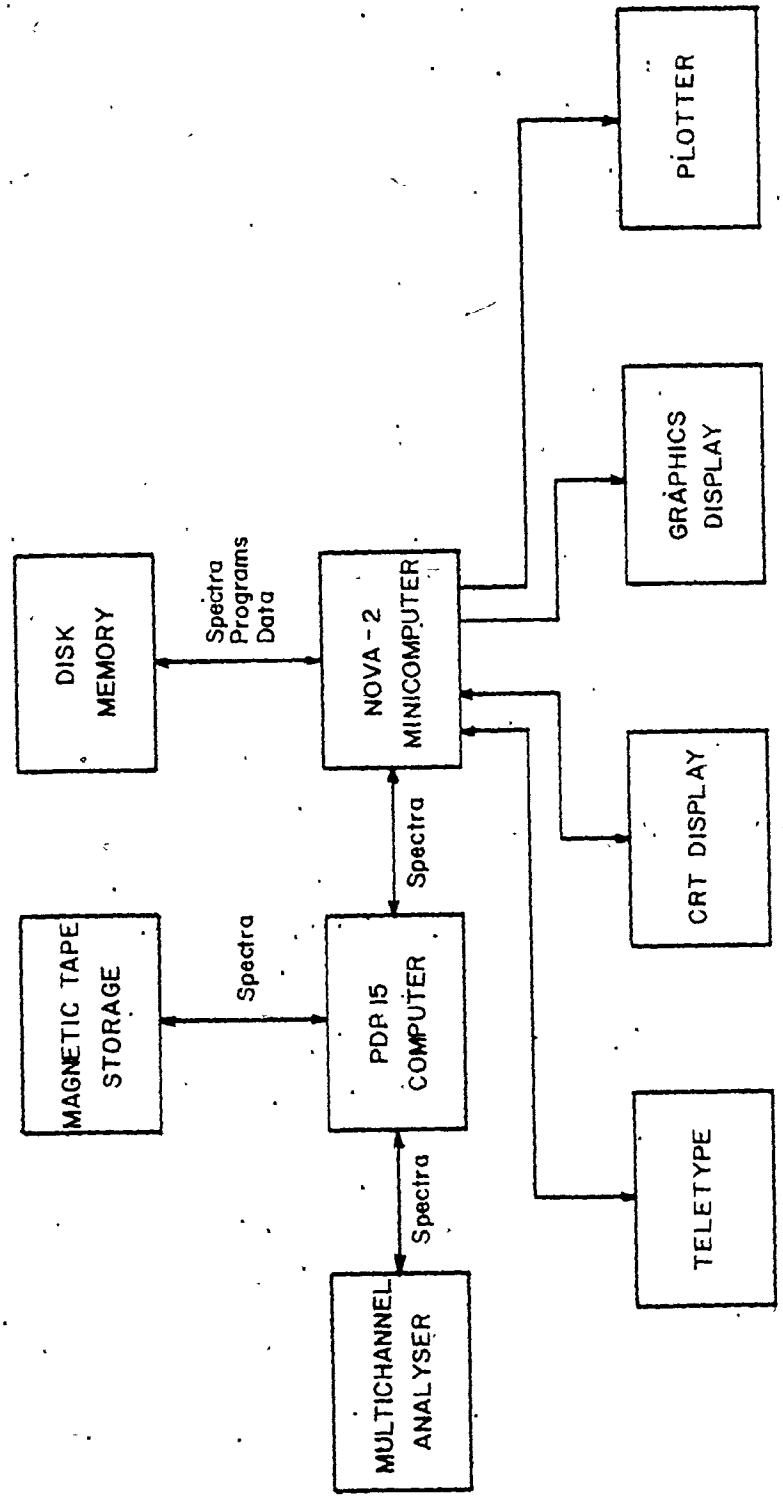

Figure 4.1 Data Acquisition System Block Diagram

A shift and add routine was used to sum the single day spectra. Each spectrum could be read in turn from the disk and added to the first spectrum after shifting the data to match the gain and zero shifts. The shift and add algorithm used the centroids of the thermal neutron and pulser peaks of both spectra to determine a gain and zero shift. If the first spectrum had thermal and pulser centroids T_1 and P_1, then a subsequent spectrum (the i^{th}) with centroids T_i and P_i could be added to the first after changing its gain and zero shift as follows:

$$g = \frac{P_1 - T_1}{P_i - T_i} \qquad \text{gain factor} \qquad (4.1)$$

$$z = P_1 - gP_i \qquad \text{zero offset correction.} \qquad (4.2)$$

The gain correction is valid only for changes in the amplifier. If the pulser voltage shifted, an incorrect gain shift would be made. If a large pulser shift occurred with no similar shift in the neutron peaks, the spectrum was discarded. Only in the unlikely event of simultaneous offsetting shifts in the amplifier and pulser, could such a pulser shift not be noticed. Small pulser shifts of a channel or two were not significant because its voltage was much higher than the photoneutron signals, whose shifts would not be noticeable.

4.2 IDENTIFICATION OF NEUTRON GROUPS

The photoneutron transitions, seen as peaks in the photoneutron spectra, could be identified from the known photon energies of nickel and chromium (Ra67), the Q-value of the (γ,n) reaction (Wa71), and the level energies of the residual nuclei (Le78). The expected neutron energies in the spectra could be obtained from

$$E_n = \left(\frac{A}{A+1}\right)\left(E_\gamma - Q - E_x\right), \qquad (4.3)$$

by using all combinations of the photon energy E_γ and the level energy of the residual nucleus E_x. Using monoisotopic samples made peak identification simpler.

The system gain was known from previous calibration; so the measured neutron energies could be matched with the expected values. Some photoneutron transitions were too weak to be observed because of a low photon intensity or an unfavourable spin configuration of the residual level; and since lengthy data acquisitions would have been required, they could not all be investigated.

4.3 REACTION RATES

The counting rate of a photoneutron transition was proportional to the differential cross-section because the counting efficiency was the same at all detector angles; so, these rates could be used for the determination of angular distribution functions. The energy difference in

photoneutrons from forward to backward angles was small enough to ignore energy dependent detector efficiency. Pulse pile-up did distort the peak shapes at extreme angles, but this effect could be corrected. Thus, a measure of the exact reaction cross-sections was not necessary to determine the angular distributions.

A separate experiment was made to check for any variation of counting efficiency with neutron emission angle. A photon resonance was found in ^{49}Ti at 8884 keV (Be78) which matched the strongest high energy photon from the chromium source. The ground state transition was expected to yield an angular distribution which was symmetric about 90^{o}; so a measurement was made of the reaction rates from 20^{o} to 160^{o}. As expected, the angular distribution function was found to have this symmetry indicating that there was no important angular dependence on the counting efficiency, which could bias the measurements. This experiment is outlined in Appendix I.

4.3.1 DETERMINATION OF PEAK AREAS

For various reasons, the calculation of peak areas was not completely straightforward. Firstly, counting statistics were sometimes poor due to the low count rates for some peaks. The peak shape could change due to pulse pile-up, resulting in a high energy tail which was hard

to distinguish from the background. This high energy tail often appeared with the peaks in the spectra taken at 20° and 160° where the detector was almost in the photon beam. The low energy tails due to different pulse risetimes as explained in section 3.4 were always present but could be accounted for in peak area determination by carefully describing the peak shape. Fortunately, because of the small number of different photon energies and the wide spacing of the levels in the residual nuclei, the photoneutron peaks were on the most part easily resolved. However, because of the 20 to 40 keV widths of the photoneutron peaks some doublets and even triplets were found, making separation of the different transitions necessary.

Most important was the nonlinear background especially at low neutron energies. This effect was due mostly to Helium-3 recoils in the detector as well as some low energy neutron background. This component can be seen in Figure 3.3 with an aluminum target which produced no photoneutrons. Except for the rapid rise in background near the thermal neutron peak, no structure was found in the background continuum which could have conceivably resulted from resonance absorption in materials such as the detector casing. These effects combined to give

uncertainties in peak areas, in some cases as high as 15-20%, but more typically 3-8%.

To remove the background from beneath a photoneutron peak, a second or third order least squares fit was made to the contents of the channels on either side of the peak. Third order fits were done around low energy peaks where the background was steepest. The background contribution to each channel, B_i, determined from the fit

$$B_i = b_0 + b_1 i + b_2 i^2 (+ b_3 i^3) \qquad (4.4)$$

was then subtracted point by point from the original spectrum Y_i, giving the counts in each channel C_i due to the photoneutrons. The value of C_i was set to zero if negative or if $C_i < \sqrt{Y_i}$ which meant the background was within a standard deviation of the contents of channel i. The peak area was then the sum of all these counts with an associated error

$$\sigma^2_{Area} = \sum_i \left[Y_i + \sum_{j,k=0}^{3} \sigma^2_{jk} \left(\frac{\partial B_i}{\partial b_j}\right)\left(\frac{\partial B_i}{\partial b_k}\right) \right], \qquad (4.5)$$

determined from the variance covariance matrix of the fit.

For some of the isolated high energy photoneutron peaks where the background levels were very low, the data were plotted by hand and a smooth curve was drawn through

the background. In this case the error in the peak was taken as

$$\sigma^2_{Area} = \sum_i (Y_i + B_i) \quad . \qquad (4.6)$$

Background subtraction was most difficult at 20° and 160° where pulse pile-up added a long high energy tail to the photoneutron peaks which could not be easily determined from the background in some cases (Figure 5.2). Because the tail extended over many channels, the peak areas after background subtraction were low since the background fits were so close to the tail. The pulse pile-up also produced the same effect on the pulser peak and because there was no background in this region, the fraction of counts in the tail could be determined by comparison with a pulser peak with no tail (at 90°). Then if the photoneutron peak area was taken, exclusive of the high energy tail, this fraction of the peak area could be added. In this case, errors were larger, and because they could not be accurately calculated conservatively large errors were used. Only two spectra had sufficiently large high energy tails to warrant this correction.

Peak area determination was not as simple for unresolved doublets or multiplets. Nonlinear least squares fitting has traditionally been used to separate

the components (Mc76), but in this work an iterative deconvolution algorithm based on Bayes' theorem was used. The algorithm has been described by Kennett (Ke78), so will not be described here except to explain the concept.

If the contents of the k^{th} channel of the measured spectrum M_k is considered as a convolution of the true spectrum T with the response function of the detection system R as follows,

$$M_k = \sum_i R_{ki} T_i \tag{4.7}$$

then the corresponding deconvolution

$$T_i = \sum_k R_{ik} M_k \tag{4.8}$$

can be expressed in terms of known quantities, if the above values are treated as probabilities. M_k (and T_i) can be considered as a measure of the probability of an event occurring in channel k (or i), and the response function R_{ki} is the conditional probability of an event occurring in channel k of the measured spectrum, given that it came from channel i of the true spectrum.

The reverse conditional probability R_{ik} of the deconvolution can be expressed in terms of Bayes' theorem

$$R_{ik} = \frac{R_{ki} T_i}{\sum_j R_{kj} T_i} \tag{4.9}$$

and by substituting the expressions of (4.7 and 4.9) into (4.8), an expression for T_i can be written which lends itself to an iterative solution

$$T_i(n+1) = T_i(n) \sum_k \left[\frac{R_{ki} M_k}{\sum_j R_{kj} T_j(n)} \right] , \qquad (4.10)$$

where $T_i(n+1)$ is the contents of the i^{th} channel of the true spectrum after $(n+1)$ iterations. This deconvolution method is superior to linear algorithms because as probabilities, no negative values are generated; and because noise amplification is reduced (Ke78a,b).

Of course, the response function must be known, but since the true spectrum must consist of extremely narrow photoneutron peaks, almost delta functions compared to the 20-40 keV observed peak widths, the response function is simply the peak shape. The photoneutron peak width varies considerably with neutron energy, and the algorithm is very sensitive to the response function; so, the deconvolution must be done on a small region of the spectrum where the resonse function can be considered constant.

After typically 512 iterations, the photoneutron peaks could be reduced to two channels with the total peak area and centroid conserved. A fast Fourier transform approach to the deconvolution was used to reduce computation time.

In Figure 4.2, a portion of a photoneutron spectrum is shown after background subtraction, together with the deconvolved spectra after 16, 256, and 512 iterations.

The response function was obtained by fitting a photoneutron peak to a Gaussian shape convolved with a low energy exponential tail. Provision was also made to include the high energy tail to account for pulse pile-up at extreme angles.

4.3.2 COUNTING TIMES

Both live and clock time were recorded for each spectrum and dead time losses of 0.3 to 1.4 percent were found. The reaction rates, however, had to be normalized to the beam intensity as measured by the sodium iodide beam monitor.

For each detector angle a beam monitor count rate was determined by taking the time weighted average of the count rates of the individual spectra. The peak areas at each detector angle were then normalized to their beam monitor count rates, and divided by the counting time to give the peak reaction rate in counts per minute. Because of the constant counting efficiency these values were proportional to the differential cross-section.

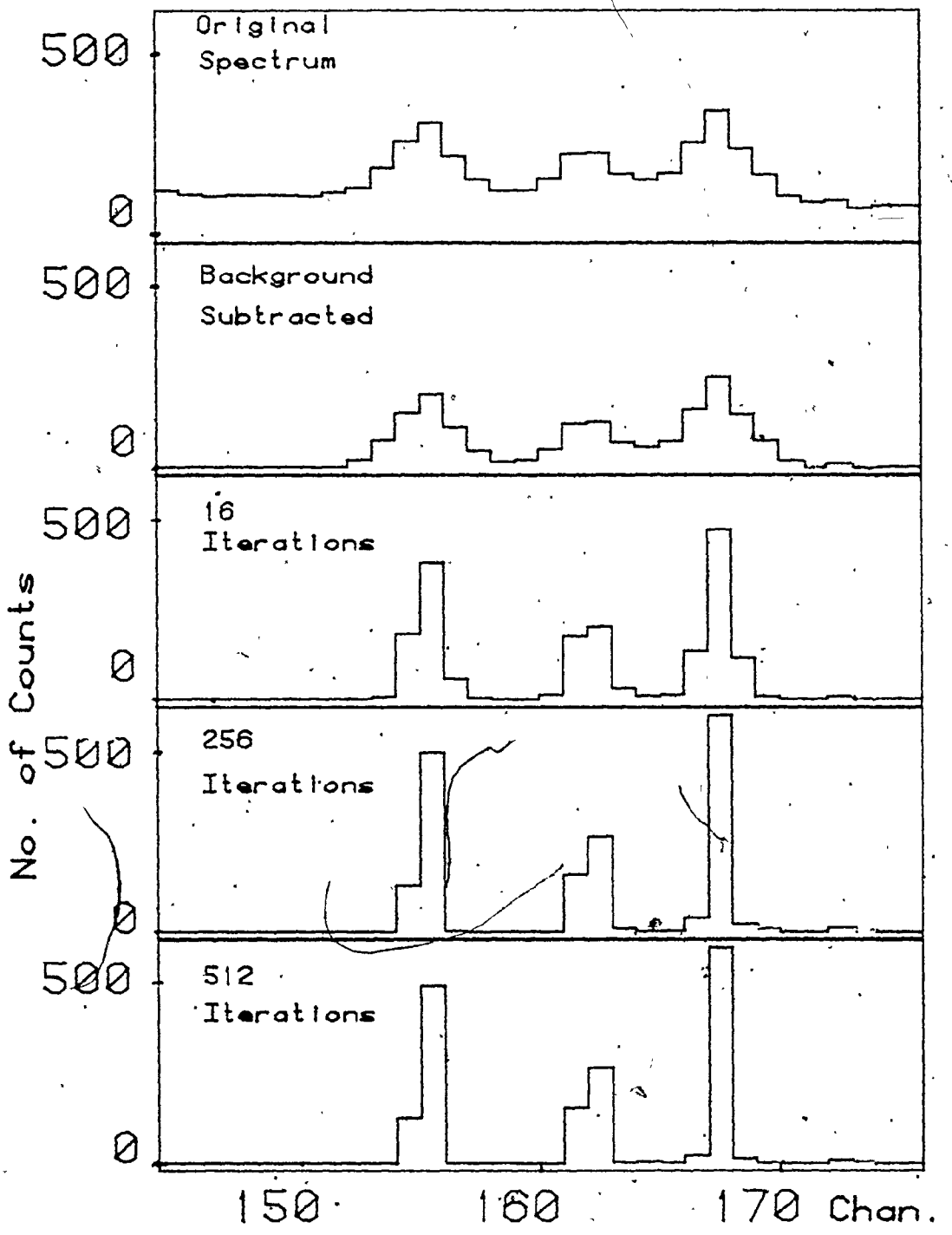

Figure 4.2 Spectral Deconvolution Using Bayes Theorem
A portion of a Photoneutron spectrum is shown with background removed, together with the deconvolved spectra after 16, 256 and 512 iterations; as described in Section 4.3.1.

4.4 THE ANGULAR DISTRIBUTIONS

The reaction rates for different photoneutron transitions showed distinct individual angular dependence. To investigate the physical significance of this angular dependence, an angular distribution function $\omega(\Theta)$ was determined. A power series fit to the angle Θ or cos Θ would be possible, but to give physical significance to the function, an expansion using the Legendre polynomials $P_\nu(\cos\Theta)$ was used:

$$\frac{d\sigma}{d\Omega}(\cos\Theta) = \sum_\nu a_\nu P_\nu(\cos\Theta) \qquad (4.11)$$

All fits were taken up to $\nu=3$ because of large errors in higher order terms with no improvement in fit. As mentioned in Chapter 2, ν cannot be greater than 4 if only E1, E2 and M1 photon multipolarities are considered.

By fitting reaction rates instead of differential cross-sections, a constant term appears in equation (4.11); but since the derived angular distribution coefficients a_ν are normalised to a_0, this will not be of concern; and so, is left out of the following discussions.

The physical significance of the angular distribution coefficients is examined in Chapter 2 and is summarized here.

a_0 - DC level, the sum of intensities of all possible reaction channels,

a_1 - forward or backward asymmetry, indicates the extent of mixing or interference of odd-even ℓ neutrons, hence E1-E2 or E1-M1 mixing,

a_2 - peakedness - indicates odd-odd and even-even ℓ neutron interference, but with no photon multipole mixing,

a_3 - similar to a_1 asymmetry, a non-zero value implies E1-E2 mixing, it has no E1-M1 contribution.

If the reaction rate were known at precisely determined values of Θ then a least squares fit could be made to the first four Legendre polynomials to deduce the best values of the angular distribution coefficients.

However, because of the finite detector size, there is a large spread in the photoneutron emission angle. The mean scattering angle is not necessarily the same as the angular setting of the detector. Clearly a fit of the reaction rates to determine the angular distribution coefficients cannot be done directly without considering these angular spreads and their effect.

4.4.1 SPREAD IN PHOTONEUTRON EMISSION ANGLES

The target-detector geometry determined the nature

of the distribution of measured neutron emission angles. An angular intensity function $S_{\Theta_D}(\Theta)$, representing the probability of detecting a photoneutron emitted at an angle Θ was determined for several detector angular positions Θ_D.

To determine $S_{\Theta_D}(\Theta)$, the target was treated as a point source of photoneutrons and the active volume of the detector was divided into small equal volume segments. The emission angle was calculated for each volume element, and a histogram of the number of volume elements for equal intervals $\Delta\Theta$ was tabulated after weighting each volume element's contribution for solid angle ($1/r^2$). Using one degree intervals, since the maximum spread was of the order of twenty degrees, this histogram normalized to unity, $S_{\Theta_D}(\Theta_i)$, was used as a digital representation of $S_{\Theta_D}(\Theta)$.

The angle of photoneutron emission and solid angle for a volume element was determined from geometry shown in Figure 4.3. The active volume of the detector is a cylinder of length ℓ and radius r_0 with its centre C a distance d from the target O. The line OC and the photon beam axis define the detection setting angle Θ_D in the vertical plane. A volume element at point A is specified by the detector's cylindrical coordinates

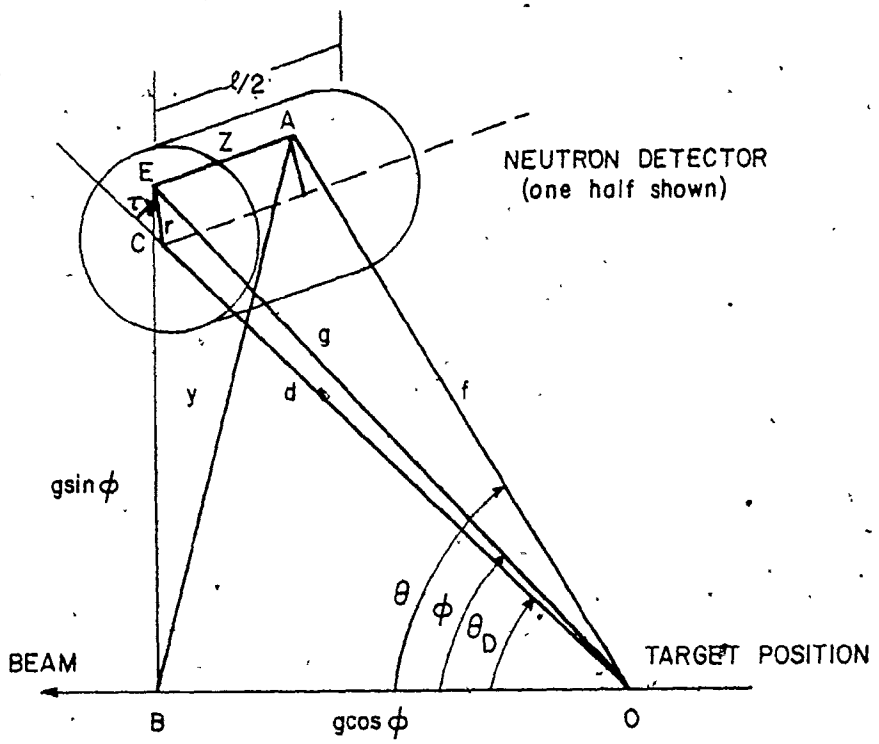

$$\phi = \theta_D + \tan^{-1}\left(\frac{r \sin \tau}{d + r \cos \tau}\right)$$

$$g = \left((r \sin \tau)^2 + (d + r \cos \tau)\right)^{\frac{1}{2}}$$

$$f = \left(g^2 + z^2\right)^{\frac{1}{2}}$$

$$y = \left((g \sin \phi)^2 + z^2\right)^{\frac{1}{2}}$$

$$\theta = \cos^{-1}\left(\frac{f^2 + (g \cos \phi)^2 - y^2}{2fg \cos \phi}\right)$$

Figure 4.3 Determination of the Angular Spread in Photoneutron Detection The detector setting is θ_D and a volume element (point A) at an angle θ and a distance f from the target is shown. The angular spread $s_{\theta_D}(\theta)$ is generated by summing over all volume elements weighted according to their solid angle ($\propto 1/f^2$). Within the detector, r varies from 0 to the detector radius R, z varies from 0 to $\ell/2$, and τ varies from 0 to 2π.

(r,τ,z) where the radius r can vary from 0 to r_0; the angle τ varies from 0 to 2π (from the line OC) and z varies from 0 to $\ell/2$. Only one half of the detector is considered because of symmetry.

To determine the photoneutron emission angle Θ, the polar angle in the vertical plane must be determined,

$$\phi = \Theta_D + \tan^{-1}\left(\frac{r \sin \tau}{d+\cos \tau}\right) , \qquad (4.12)$$

and the distance of the line OE calculated,

$$g = \left[(r\sin\tau)^2 + (d+r\cos\tau)^2\right]^{\frac{1}{2}} . \qquad (4.13)$$

The distance, OA, from the target to the volume element, is

$$f = (g^2 + z^2)^{\frac{1}{2}} . \qquad (4.14)$$

which determines the solid angle weighting factor.

The triangle OBA defines the emission angle Θ; the length OB is $g\cos\phi$, OA is determined from 4.14, and the third size AB is

$$y = \left((g\sin\phi)^2 + z^2\right)^{\frac{1}{2}} . \qquad (4.15)$$

The cosine law is used to determine θ

$$\theta = \cos^{-1}\left\{\frac{f^2 + (g\cos\phi)^2 - y^2}{2fg\cos\phi}\right\} \qquad (4.16)$$

Seventy-two thousand equal volume elements were considered, with 180 subdivisions of r, 20 subdivisions for z and 20 for r. The histograms were generated using the NOVA microcomputer and are shown in Figure 4.4 for the detector settings 20^0, 40^0, 60^0 and 90^0. At detector settings beyond 90^0, the angular spreads are mirror images of the spreads at the corresponding forward angle setting ($180^0 - \theta_D$).

It can be seen that the widths of the angular spreads are significant. Also, at the angles furthest from 90^0, the mean of the distribution is quite different from the detector setting.

Clearly, the measured reaction rates cannot be fitted directly using the Legendre polynomials and give meaningful results. The measured reaction rates are in fact the true rates or cross-sections $\frac{d\sigma}{d\Omega}(\cos\theta_D)$ of equation 4.11 convolved or distorted by the response function $S_{\theta D}(\theta)$. If the Legendre polynomials were also convolved with the same response function, the measured reaction rates could be fitted to the resulting functions to arrive at the angular distribution coefficients of

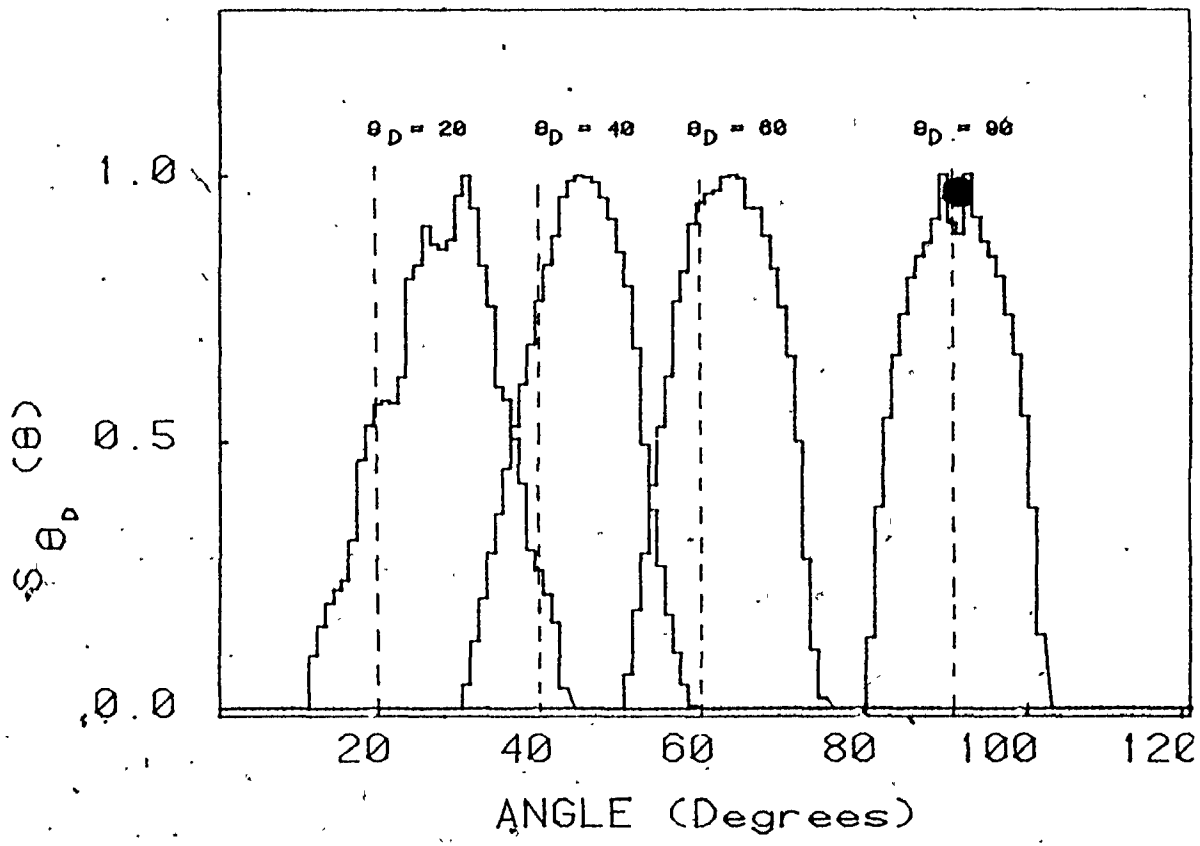

Figure 4.4 Detector Angular Spreads $s_{\theta_D}(\theta)$ at Detector Settings of 20,40,60 and 90 Degrees. The histograms were generated in 1 degree intervals as described in Section 4.4.1.

equation 4.11. If both sides of equation 4.11 are convolved with $S_{\theta_D}(\theta)$, the measured cross-section may be expressed as:

$$\frac{d\sigma}{d\Omega}(\cos\theta_D)_{meas.} = \int_0^{\pi} \frac{d\sigma}{d\Omega}(\cos\theta)\, S_{\theta_D}(\theta)d\theta$$

$$= \sum_{\nu} a_{\nu} \int_0^{\pi} P_{\nu}(\cos\theta) S_{\theta_D}(\theta)d\theta, \qquad (4.17)$$

and thus can be expanded in terms of polynomials $Q_{\nu}(\cos\theta)$ defined as:

$$Q_{\nu}(\cos\theta_D) = \int_0^{\pi} P_{\nu}(\cos\theta)\, S_{\theta_D}(\theta)d\theta, \qquad (4.18)$$

or using a discrete histogram in steps of one degree:

$$Q_{\nu}(\cos\theta_D) = \sum_{\theta_i=0}^{180^o} P_{\nu}(\cos\theta_i) S_{\theta_D}(\theta_i) \; . \qquad (4.19)$$

Fitting the measured reaction rates to the Q_{ν} functions,

$$\frac{d\sigma}{d\Omega}(\cos\theta)_{meas.} = \sum_{\nu} a_{\nu}\, Q_{\nu}(\cos\theta), \qquad (4.20)$$

generates the same parameters a_ν as the fit of the true rates with the Legendre polynomials in equation 4.11.

4.4.2 CALCULATION OF THE $Q_\nu(\cos\theta)$ FUNCTIONS.

The Q_ν values were determined at every ten degrees from 0 to 180 using equation 4.19. Since the angular spread histograms $S_{\theta_D}(\theta_i)$ were normalized, Q_0 was a constant = 1 for all θ, the same as P_0. Least squares fits of the Q_ν values in power series of $\cos\theta$ were made, and are shown in Table 4 together with the corresponding expressions for the Legendre polynomials. Graphical comparisons shown in Figure 4.5, point out the similarities between the two types of functions.

4.4.3 THE ANGULAR DISTRIBUTION FUNCTION AND ASYMMETRY PARAMETER.

From these fits to the measured reaction rates at seven detector settings, an angular distribution function was determined for every transition:

$$\omega(\theta) = 1+a_1P_1(\cos\theta)+a_2P_2(\cos\theta)+a_3P_3(\cos\theta). \qquad (4.21)$$

The coefficients are normalized to a_0. The errors in the parameters are determined from the variance-covariance

--- $Q_2(x) = 1.341x^2 - .481$ --- $Q_4(x) = 3.404x^4 - 3.144x^2 + .336$
—— $P_2(x) = 1.5x^2 - .5$ —— $P_4(x) = 4.375x^4 - 3.75x^2 + .375$

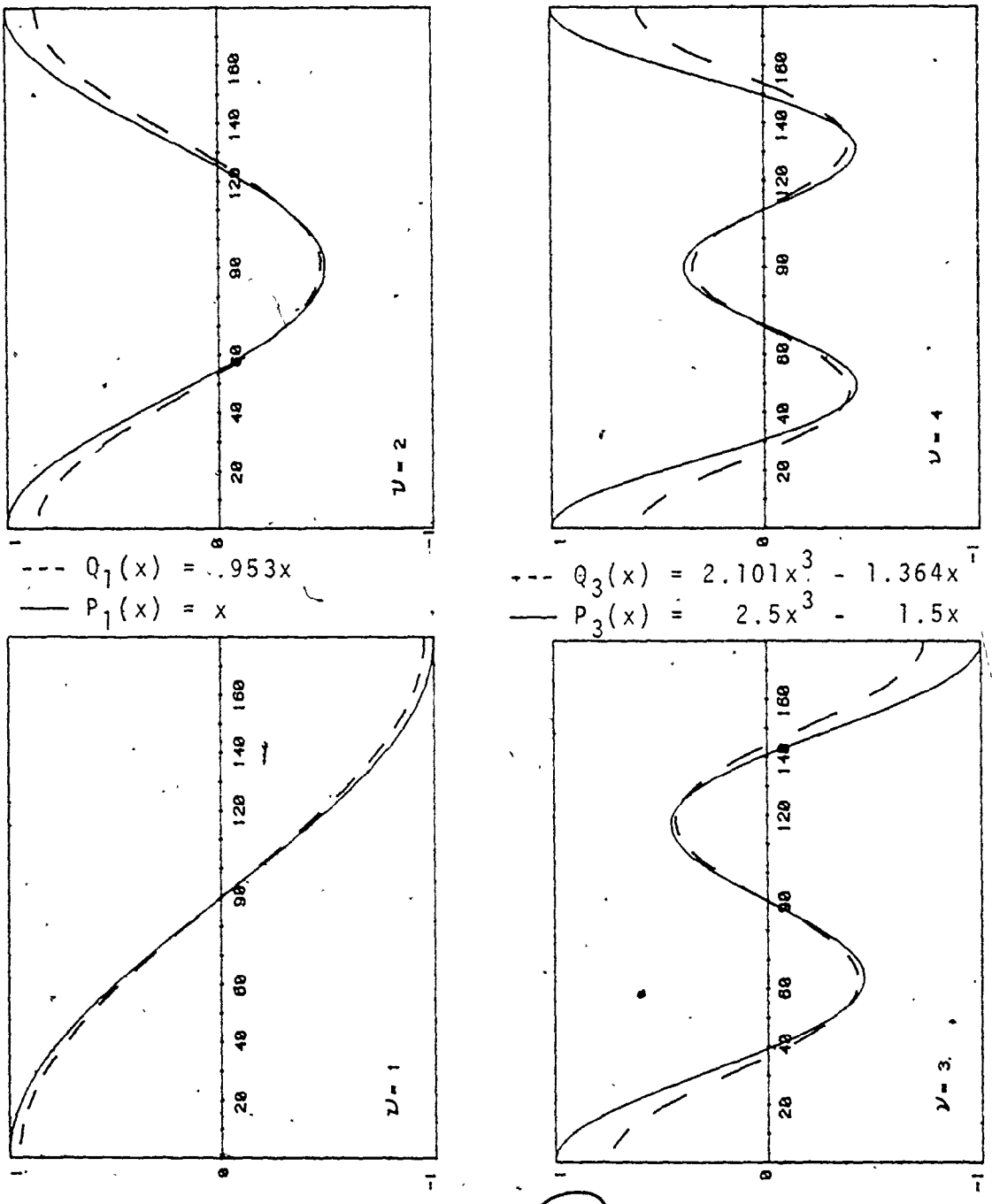

Figure 4.5 The Modified Legendre Polynomials

matrix of the fit which depends on the errors in the measurements at each angle. Because of the non-orthogonality of the Q_ν functions, there is a significant covariance contribution to the errors in the angular distribution coefficients. As mentioned in chapter 2, an indication of the extent of E1-E2 or E1-M1 mixing is the asymmetry parameter or interference factor defined as:

$$I_{E_\gamma,E_x}(\theta) = \frac{\frac{d\sigma}{d\Omega}(\theta) - \frac{d\sigma}{d\Omega}(\pi-\theta)}{\frac{d\sigma}{d\Omega}(\theta) + \frac{d\sigma}{d\Omega}(\pi-\theta)}$$

$$= \frac{a_1 P_1(\cos\theta)+a_3 P_3(\cos\theta)}{a_0+a_2 P_2(\cos\theta)} \quad . \qquad (4.22)$$

This function is a maximum at 0^0 and is zero at 90^0; so, an intermediate value was chosen. An angle of 55^0 is useful (Lo78) because $P_2(\cos 55^0) \approx 0$, eliminating the a_2 contribution to the uncertainty in I. A non-zero asymmetry parameter is evidence for multipole mixing although a small value of I is not in itself an indication of little or no mixing.

CHAPTER 5

RESULTS AND DISCUSSION

In this chapter, the results are presented for lead 206 and lead 208 in two separate sections. All photoneutron spectra are shown as well as the angular distributions for each observed transition. For each transition with a known unambiguous final state spin, calculations of the E2:E1 mixing ratio are given, based on the formalism of section 2.2. For photon energies where M1 contributions could not be ruled out due to a non-zero a_3 term, an alternate measure of the M1:E1 mixing ratio is given. Consistency within the various transitions for each photon is then the criterion for the choice of E2 or M1 strength.

5.1 LEAD 206

5.1.1 The Photoneutron Spectra

Figures 5.1 to 5.4 show the photoneutron spectra for the ^{206}Pb target. In Figures 5.1 and 5.3, detailed spectra taken at 90 degrees, using the nickel and chromium sources respectively are shown. The transitions are identified, knowing the system gain and the expected neutron energies

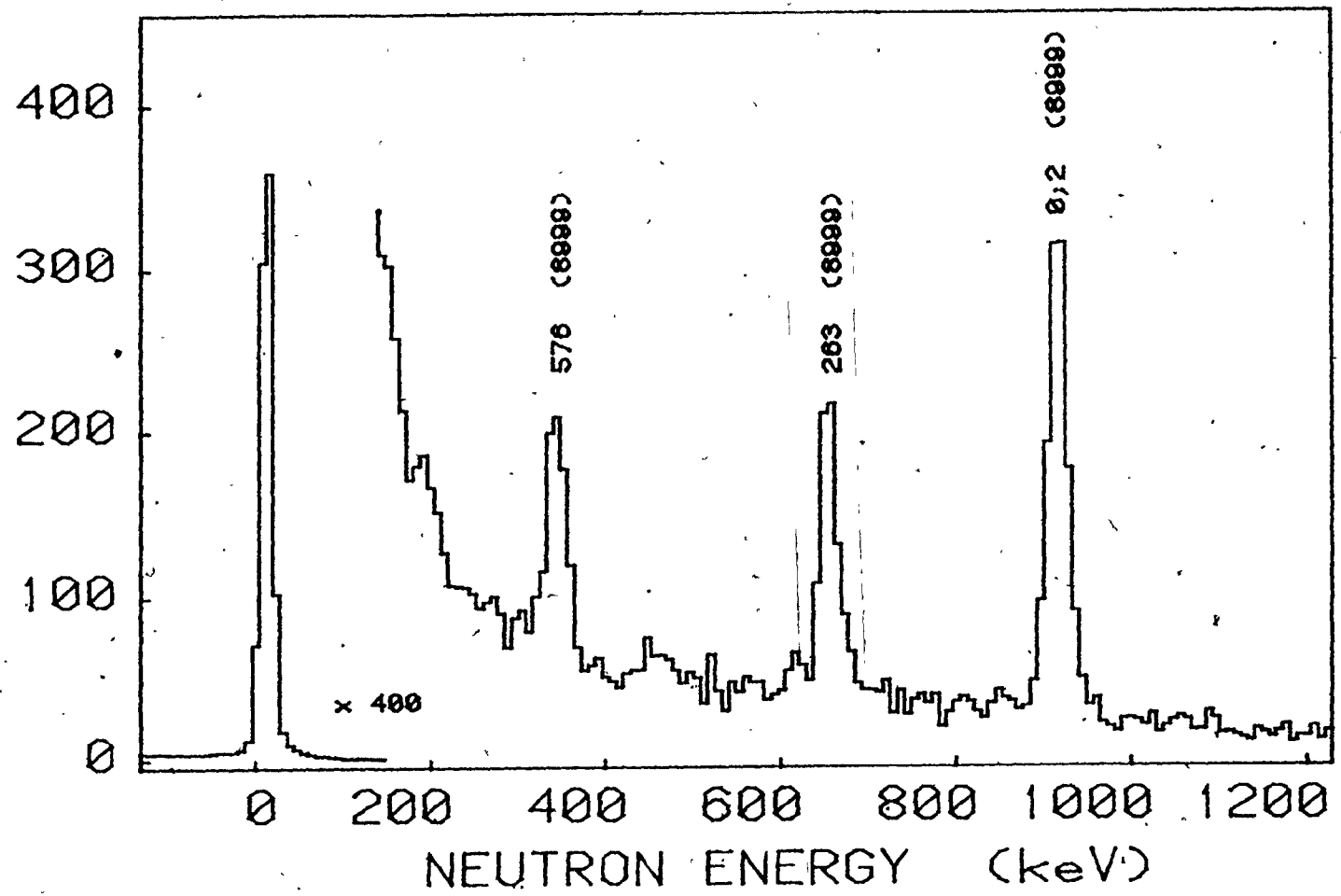

Figure 5.1 Photoneutron Spectrum of Pb-206 with Nickel Source at 90 degrees
Transitions are identified by photon energy E_γ and energy of the residual level of Pb-205, E_x.

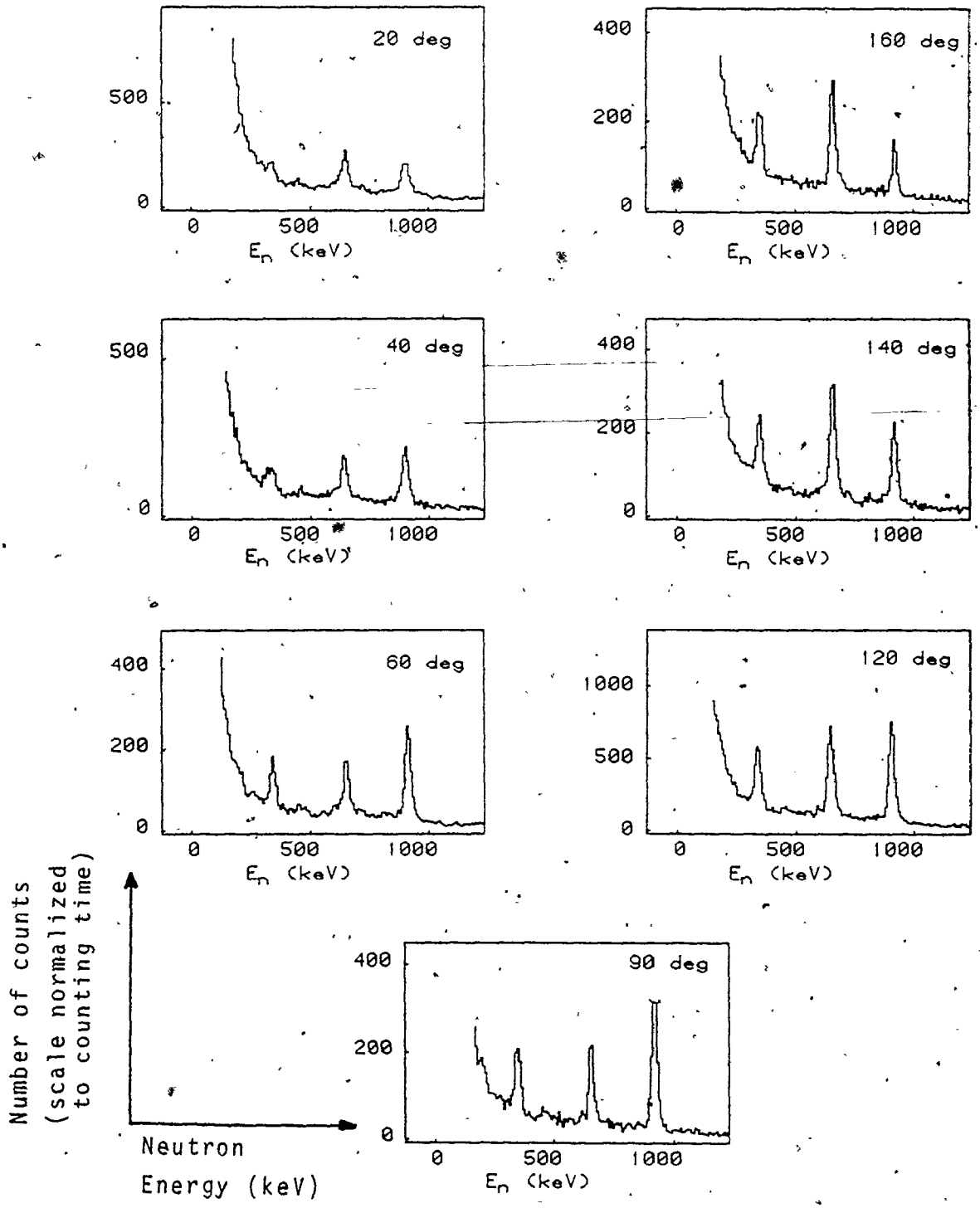

Figure 5.2 Photoneutron Spectrum of Pb-206 with Nickel Source at all Angles

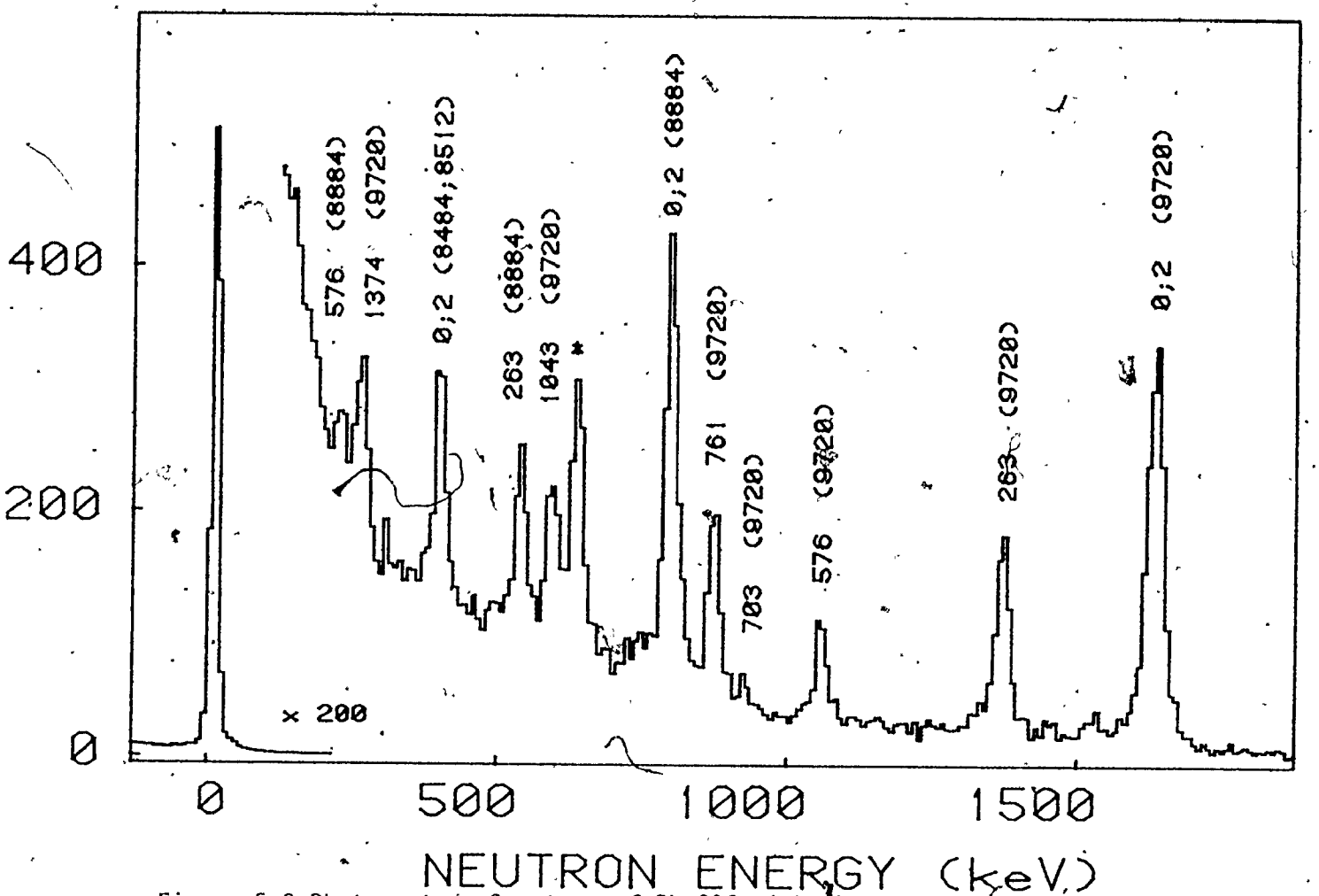

Figure 5.3 Photoneutron Spectrum of Pb-206 with Chromium Source at 90 degrees
Transitions are identified by the photon energy E_γ and the energy of the residual level of Pb-205, E_x. The transition (*) is from the 9720 keV photon to three unresolved levels in Pb-205 at 988, 999, and 1014 keV.

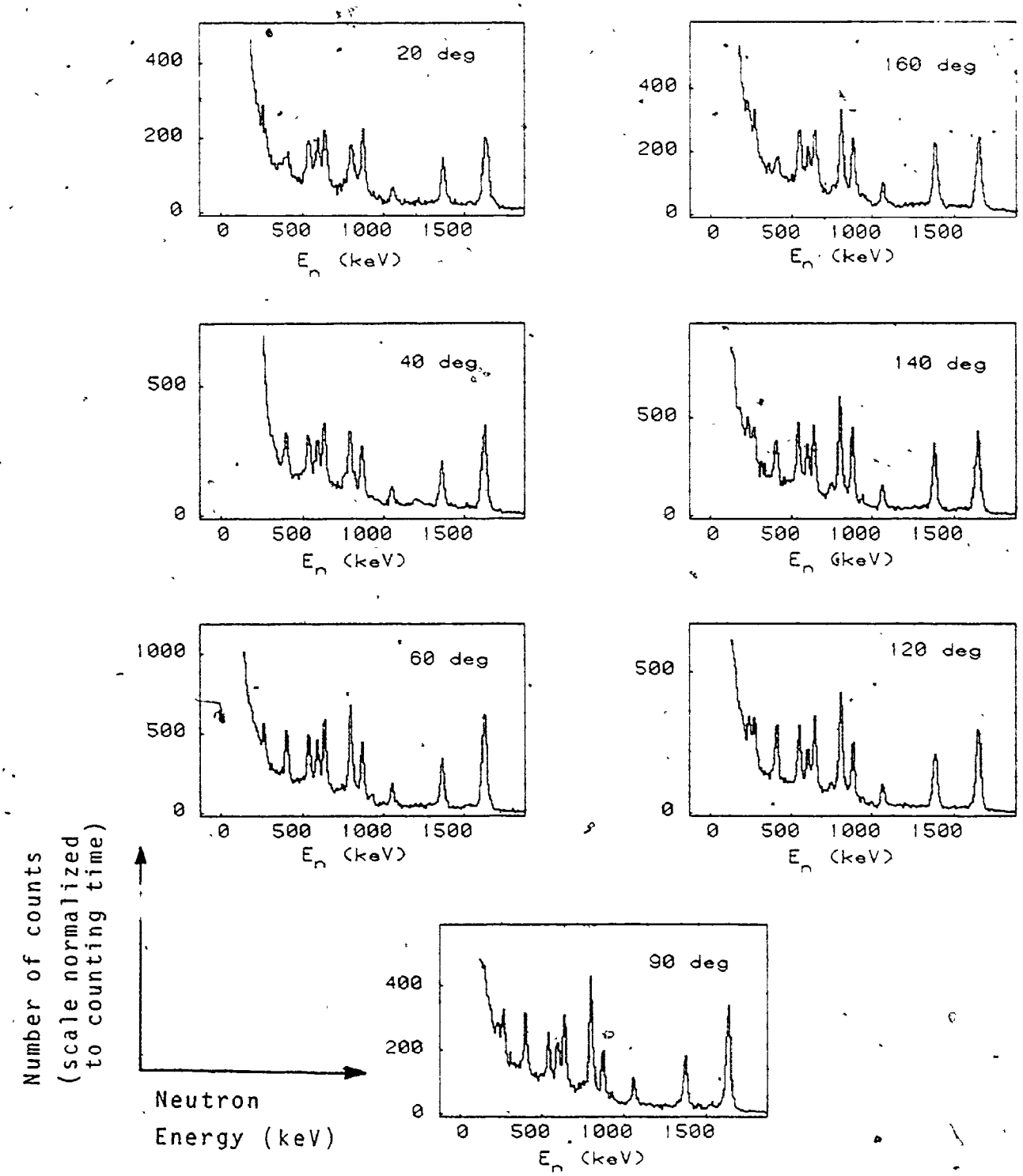

Figure 5.4 Photoneutron Spectrum of Pb-206 with Chromium Source at all Angles

$$E_n = \frac{A}{A-1} (E_\gamma - E_x - Q), \qquad (5.1)$$

for the various combinations of photon energy E_γ and ^{205}Pb level energy E_x, listed in Table 5.1. Here, A=206 and the reaction Q value is 8090 keV.

For the angular distribution determinations, spectra were recorded at 20, 40, 60, 90, 120, 140, and 160 degrees, and all seven spectra are shown in Figure 5.2 for the nickel source, and in Figure 5.4 for chromium. For visual purposes the number of counts are scaled according to the data acquisition times; so, the variation in cross-section can be seen for each transition as a function of neutron emission angle.

The counting rates for each transition are listed for each angle in Tables 5.2 to 5.4 as follows:

a) Transitions for E_γ = 8999 keV (nickel) Table 5.2A

b) Transitions for E_γ = 9720 keV (chromium) Table 5.3A

c) Transitions for other chromium photons, E_γ = 8884 keV and doublet at 8484, 8512 keV Table 5.4A.

5.1.2 THE ANGULAR DISTRIBUTIONS

By fitting the measured reaction rates at the seven angles to the modified Legendre Polynomials $Q_\nu(\cos\theta)$, described in section 4.4, the angular distribution coefficients α_ν from the expansion of the differential cross-section

$$\frac{d\sigma}{d\Omega}(\theta) = \sum_\nu \alpha_\nu P_\nu(\cos\theta)$$

were determined. These coefficients, up to $\nu=3$ and normalized to α_o, are listed in Tables 5.2B to 5.4B for each transition, together with the tables of the measured reaction rates. Along with the angular distribution coefficients, the asymmetry parameter $I(E_\gamma,\theta)$ at $\theta = 55^o$ is given.

In Figures 5.5 to 5.8, the measured reaction rates and the fitted angular distribution functions $\sum_\nu \alpha_\nu Q_\nu(\cos\theta)$ are shown. The plots are grouped so that all the transitions leading to the same level of the residual nucleus are shown in the same figure. In Figure 5.5, the angular distributions for all transitions leading to the unresolvable ground state (spin $\frac{5}{2}^-$) and 2 keV (spin $\frac{1}{2}^-$) levels of ^{205}Pb are shown.

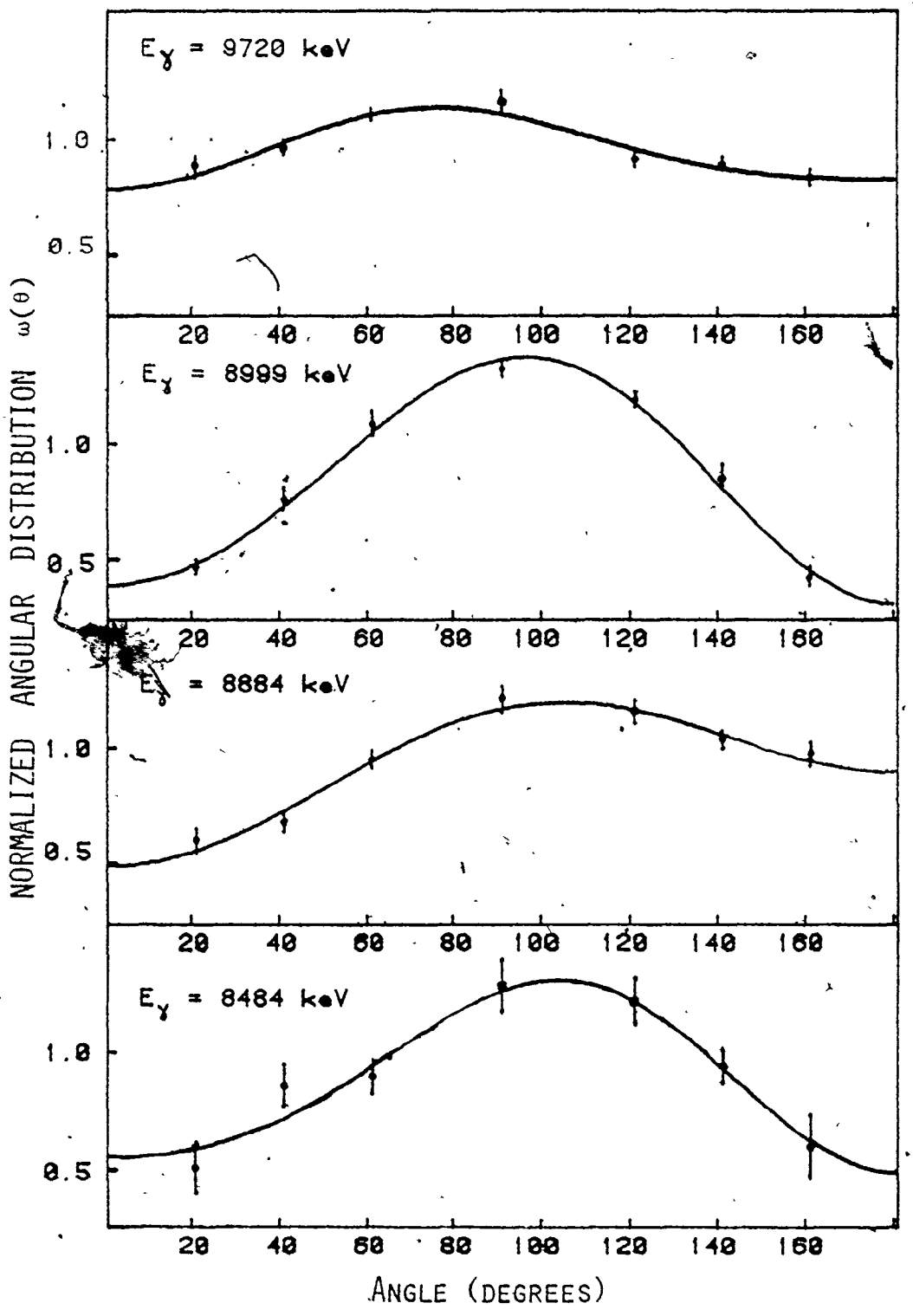

Figure 5.5 Pb-206 (γ,n) Angular Distributions
Transitions to the ground state, 2 keV doublet
of P , for E_γ - 9720, , keV

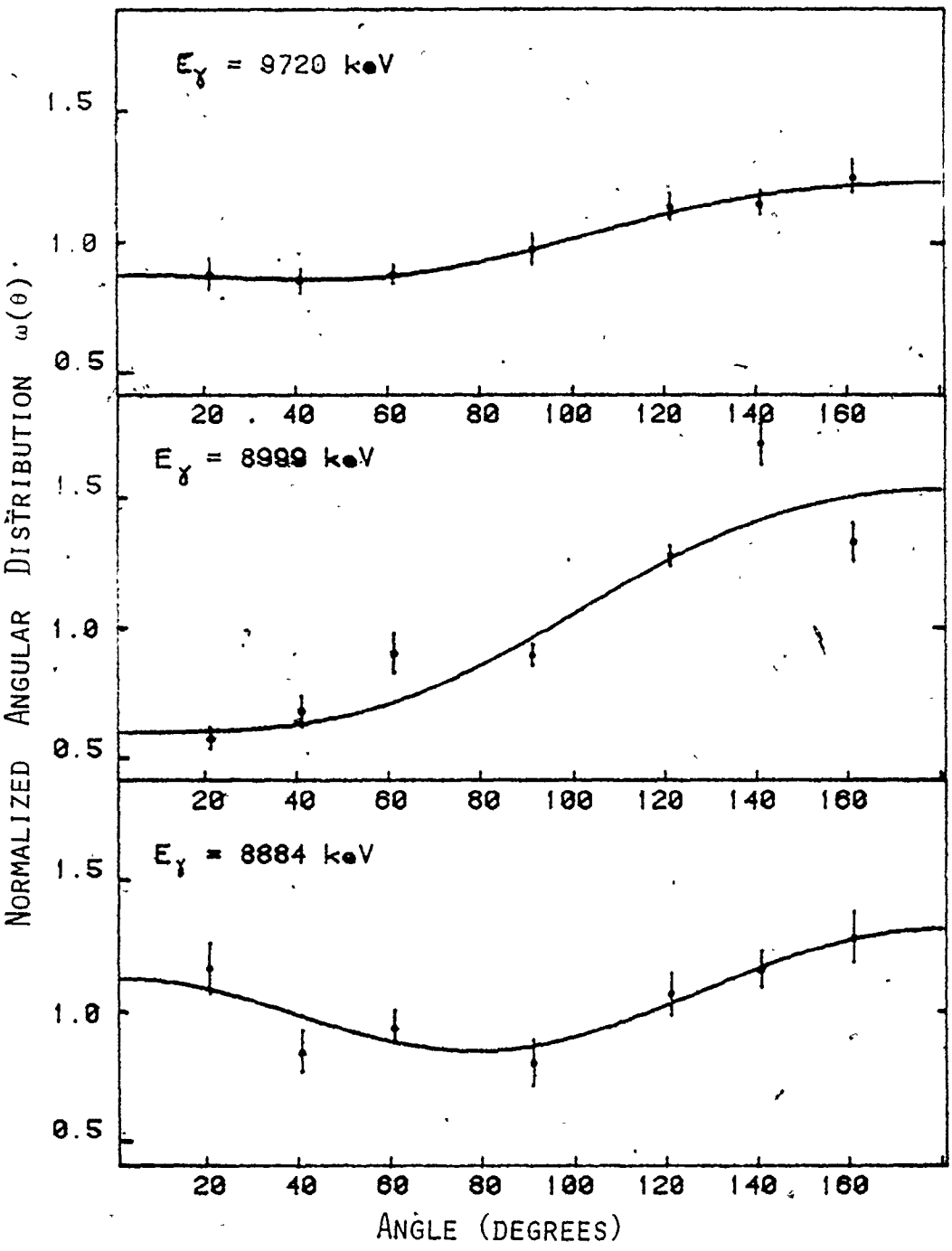

Figure 5.6 Pb-206 (γ,n) Angular Distributions
Transitions to the 263 keV level of Pb-205,
for E_γ = 9720,8999,8884 keV.

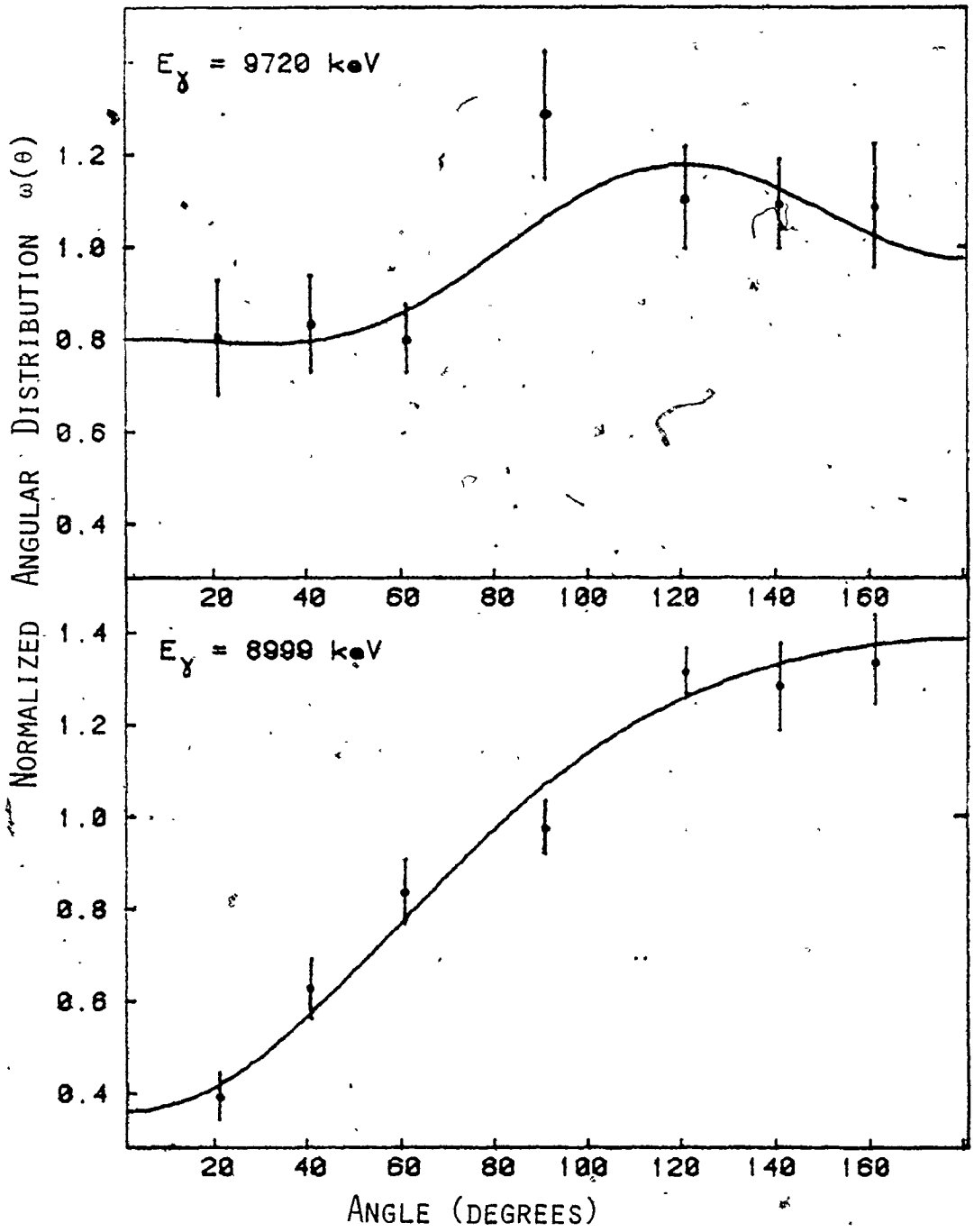

Figure 5.7 Pb-206 (γ,n) Angular Distributions
Transitions to the 576 keV level of Pb-205,
for E_γ = 9720,8999 keV.

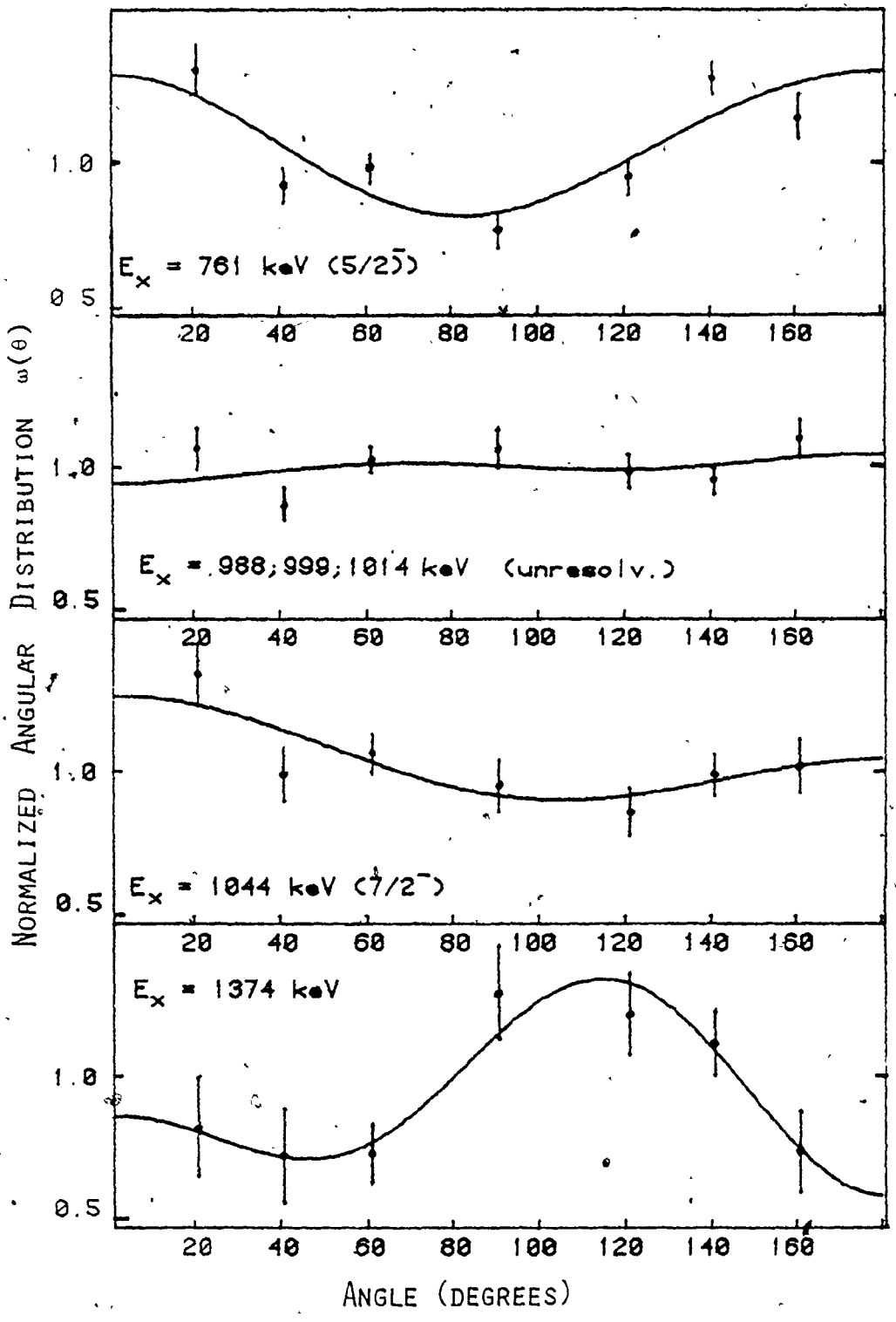

Figure 5.8 Pb-206 (γ,n) Angular Distributions
Transitions for E_γ = 9720 keV, to Pb-205 levels
at 761, 1044, 1374 keV and unresolved triplet

Since these levels had different spins, an expansion of the coefficients in terms of reaction matrix elements was not feasible. Figures 5.6 and 5.7 show the angular distributions for each observed transition to the 263 keV and 576 keV levels respectively. Both have spin $\frac{3}{2}^-$. Transitions were also observed for the 9720 keV photon to higher energy levels in ^{205}Pb. The angular distributions for these transitions are shown in Figure 5.8.

In Figure 5.9, the angular distribution coefficients and asymmetry parameter are shown as a function of photon energy for the transitions to the 0,2 keV doublet, 263 and 576 keV levels of ^{205}Pb. Any trends in the parameters with photon energy must be made with caution, because a particular photon energy may be close to a narrow resonance. The values of a_1 and I for the two $\frac{3}{2}^-$ levels are largest at 8999 keV which could indicate the presence of a nearby E2 (or M1 resonance).

These results can be compared with similar measurements made concurrently with this work in Israel (Bi79). There is a significant discrepancy in the forward angle cross-section seen in the transitions to the ground + 2 keV states of ^{205}Pb for the following photon energies: 8484 keV, 8884 keV

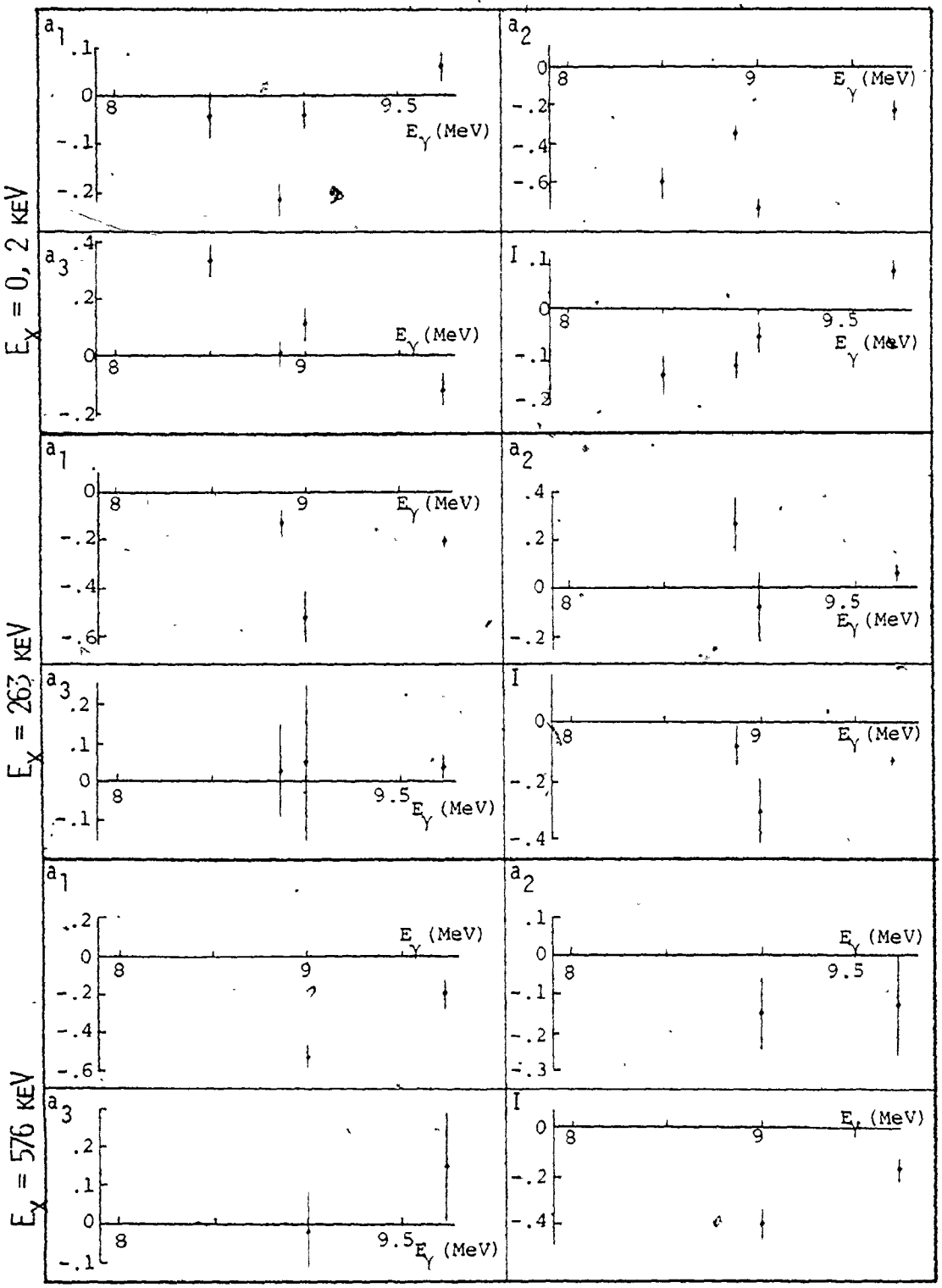

Figure 5.9 Variation of Angular Distribution Coefficients a_υ and Asymmetry Parameter $I(E_\gamma,55°)$ with Photon Energy for $^{206}Pb(\gamma,n)^{205}Pb$

and 8999 keV. In each of these three transitions, but not at 9720 keV, the forward angle cross-sections relative to 90 degrees are higher in the present work, giving flatter angular distributions. The reasons for this discrepancy are not known. Pulse pileup at forward angles due to photons scattering from the beam would generate smaller peak areas; so, this effect is unlikely. In the other experiment, no measurements were made below 40 degrees, but the shape of their curves would not account for the discrepancy. The lack of similar effect at 9720 keV would tend to eliminate a systematic error in measurement.

5.1.3 MULTIPOLE MIXING

The existence of an asymmetry about 90 degrees in the angular distribution is sufficient to indicate the mixing of at least two photon multipoles. By examining Figure 5.9 and Tables 5.2 to 5.4, non-zero values of the asymmetry terms, a_1, a_3 and $I(E_\gamma, 55^o)$ are found at all photon energies studied, confirming multipole mixing. Non-zero values of a_3 at photon energies of 8484, 8512, 8999 and 9720 keV imply that the mixing is E2:E1, if three way admixtures can be ruled out. The possibility of M1 contribution at 8884 keV cannot be eliminated.

Using the angular distribution coefficients of Appendix II in equation 2.12, the E2:E1 mixing ratio α is calculated from the experimentally determined coefficients a_ν. The neutron transmission probabilities and phase angles used in the reaction matrix element approximations are listed in Table 5.5 for all observed transitions in ^{206}Pb. If M1:E1 mixing is considered, the mixing ratio β can be determined as an alternative.

As an example, the equations for the transition E_γ = 8999 keV, E_x = 576 keV, $j^{\pi A-1}_{A-1} = 3/2^-$ are shown below, assuming E2:E1 mixing. By considering the ratios a_1/a_0, a_2/a_0 and a_3/a_0, the constant of proportionality is removed, leaving two unknowns: α, the mixing ratio of E2 to E1 strength, and the E2:E1 phase angle δ:

$$\frac{a_1}{a_0} = -.52\pm.07 = \frac{\sqrt{\alpha}\ (2.99\cos(\delta+52^0) - .62\cos(\delta+17^0) + .29\cos(\delta+1^0))}{1.64 + 2.57\alpha} \qquad (5.2)$$

$$\frac{a_2}{a_0} = -.15\pm.13 = \frac{.23 - .30\alpha}{1.64+2.57\alpha} \qquad (5.3)$$

$$\frac{a_3}{a_0} = -.20\pm.11 = \frac{\sqrt{\alpha}(.33\cos(\delta+70^0) + .61\cos(\delta+17^0) + .02\cos(\delta+1^0))}{1.64 + 2.57\alpha} \qquad (5.4)$$

The asymmetry parameter $I(55^0)$ can also be used:

$$I(55^0) = \frac{a_1 P_1(\cos 55^0) + a_3 P_3(\cos 55^0)}{a_0 + a_2 P_2(\cos 55^0)}$$

$$-.27 \pm .05 = \frac{\sqrt{\alpha}\,(1.72\cos(\delta+52^0) - .59\cos(\delta+17^0) + .16\cos(\delta+1^0) - .13\cos(\delta+70^0)}{1.64 + 2.57\alpha} \qquad (5.5)$$

At first glance, the expression for a_2/a_0 would appear to give a value of α which was independent of the phase angle δ. However, because of the similarity of the expressions for a_2 and a_0, α is found to be extremely sensitive to a_2/a_0; in this case, α can range from positive to negative infinity over the range $a_2 \pm \Delta a_2$. Similar results were found for most transitions; so, the a_2 term was not used in the calculating of α.

The expressions for a_1/a_0 and $I(E_\gamma, 55^0)$, which had smaller experimental uncertainties than a_3/a_0, could be used to determine an upper and lower bound for α. Simultaneous solution of equations 5.2 and 5.5 was not possible, but for a given angle δ, these equations are quadratics in $\sqrt{\alpha}$. A plot of α vs. δ is shown in Figure 5.10 for the above example. The three curves represent the solution using the

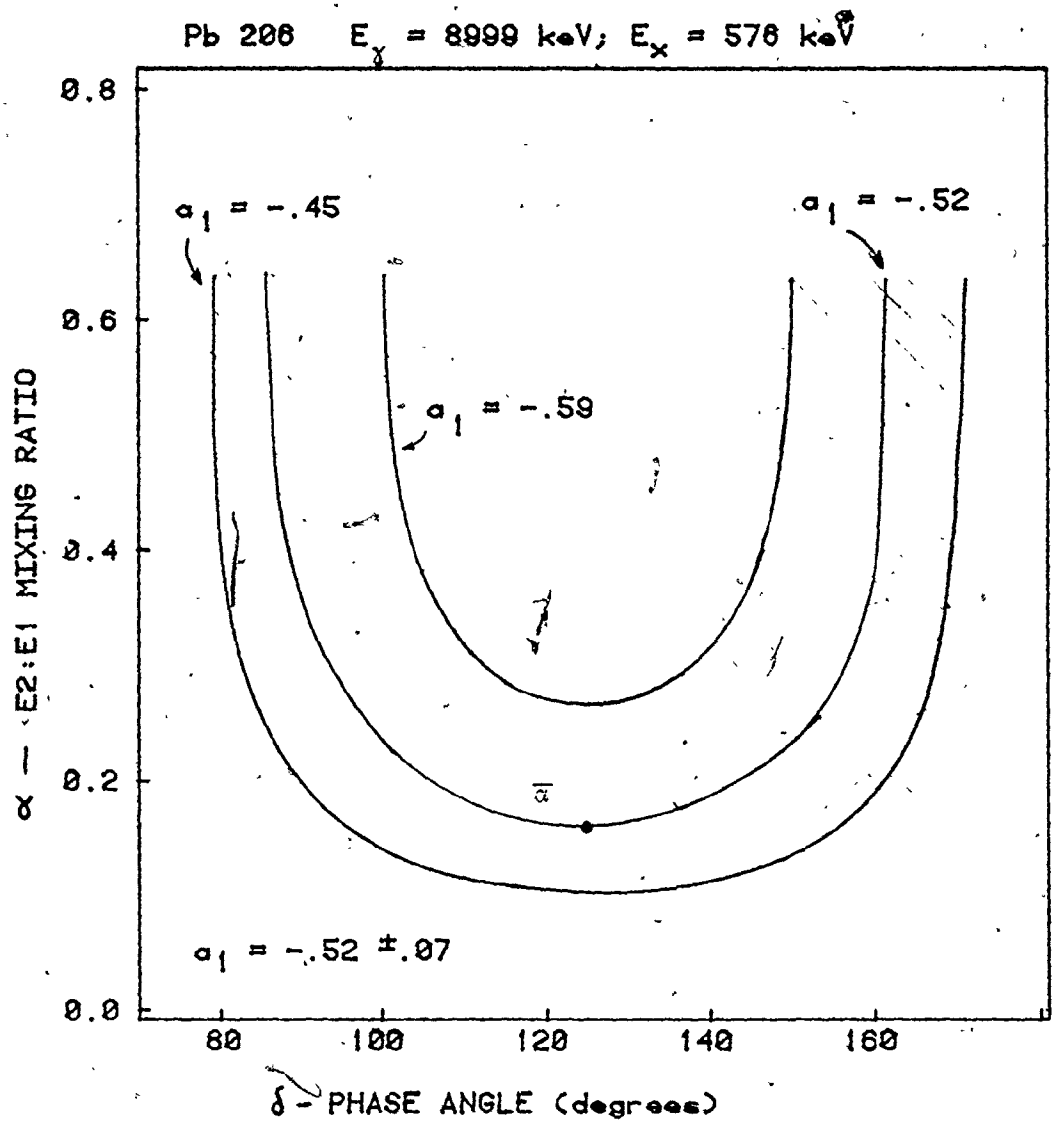

Figure 5.10 E2 : E1 Mixing Ratio and Phase Angle for a_1 Coefficient

experimentally determined value of a_1 and the two limits $a_1 \pm \Delta a_1$. The solution is real for $87^0 < \delta < 164^0$ and the shaded region provides a range of possible values for α, in this case $.10 < \alpha < .64$. There is another range of phase angles ($267^0 < \delta < 344^0$) which gives values of α much greater than 1, but since the tail of the giant dipole resonance is the dominant feature in this energy range, these solutions are not considered. Plots of α vs δ for other transitions all show the same features, a fairly flat portion over most phase angles which rises very quickly at either end. The upper and lower bound values for the mixing ratio and the range of phase angle are listed in Table 5.6 for all transitions where the final spin state is unambiguous. Also, since the mixing ratio is reasonably constant over most of the range in δ, the minimum value of α is also listed for the middle of the three curves specified by the experimentally determined value of a_1. This is shown as $\bar{\alpha}$ in Figure 5.10 and is useful as a comparison between different photon energies, but is not to be taken as an average or most likely value of the mixing ratio. The uncertainty in this value is taken from the upper and lower curves and for the transition described above, $\bar{\alpha} = .16^{+.10}_{-.04}$.

Ideally, the mixing ratio should be the same for all transitions involving the same photon energy, unless there is strong coupling between the reaction entrance and exit channels. The values of α and δ from Table 5.6 do show reasonable consistency between the different transitions from the expressions for α_1 and $I\ (E_\gamma, 55^o)$ at each photon energy. By including all the values from Table 5.6, the following mixing ratios are predicted:

$$E_\gamma = 9720 \text{ keV}, \quad .05<\alpha< .25$$

$$E_\gamma = 8999 \text{ keV}, \quad .12<\alpha< .58$$

$$E_\gamma = 8884 \text{ keV}, \quad .002<\alpha< .59 \ .$$

Since M1:E1 mixing cannot be discounted for $E_\gamma = 8884$ keV, the mixing ratio would be $.001<\beta< .99$.

Summarizing the lead 206 results, the largest mixing ratio is found at 8999 keV, and since the a_3 term for the ground state transition is non-zero, this indicates that this region is likely near some concentration of E2 strength. An E2:E1 mixing ratio of at least .05 is necessary to explain the observed asymmetries in all the transitions from $E_\gamma = 9720$ keV. At 8884 keV, the absence of a non-zero a_3

term indicates that E2 or M1 mixing may be present with minimum mixing ratios of .002 and .001 respectively. The upper limits to the mixing ratios are less meaningful than the lower values, since α is relatively constant near its minimum value over most of the range in phase angle.

5.2 LEAD 208

5.2.1 THE PHOTONEUTRON SPECTRA

The observed photoneutron transitions for the strongest photons of the nickel and chromium sources are shown in Table 5.7.

As in the last section for lead 206, the photoneutron spectra collected at 90 degrees are shown in detail with each transition identified. These are displayed in Figures 5.11 and 5.13 for the nickel and chromium sources respectively. The spectra at all seven angles are presented in Figures 5.12 and 5.14, again scaled according to counting time to illustrate the variation of cross-section with angle for all transitions. The measured peak counting rates are listed in Tables 5.8 to 5.12 as follows:

a) Transitions for E_γ = 8999 keV (nickel) Table 5.8A
b) Transitions for E_γ = 8533 keV (nickel) Table 5.9A
c) Transitions for E_γ = 9720 keV (chromium) Table 5.10A
d) Transitions for E_γ = 8884 keV (chromium) Table 5.11A
e) Transitions for other lines of nickel and chromium Table 5.12A.

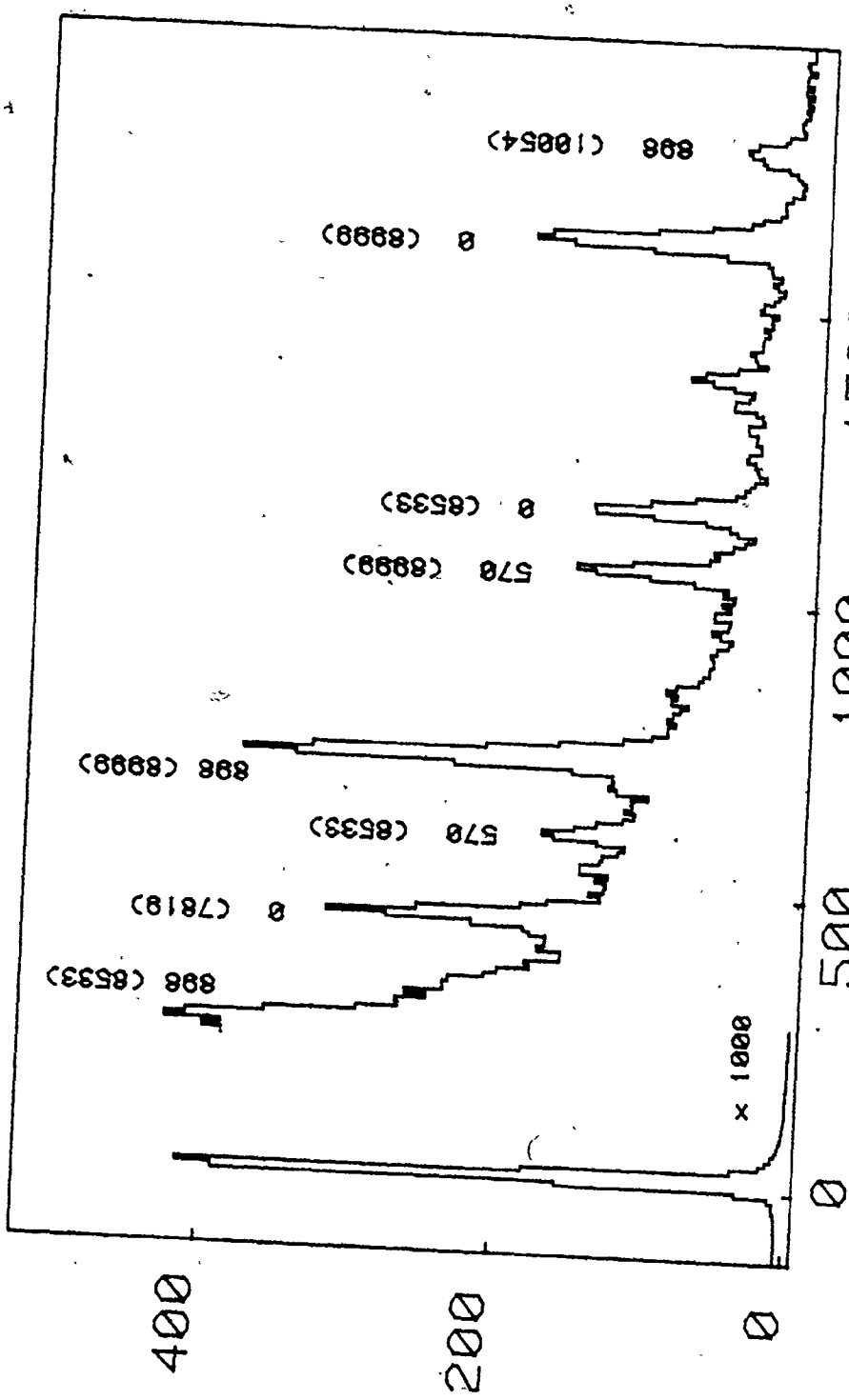

Figure 5.11 Photoneutron Spectrum of Pb-208 with Nickel Source at 90 degrees

Transitions are identified by photon energy E_γ and energy of the residual level of Pb-207, E_x.

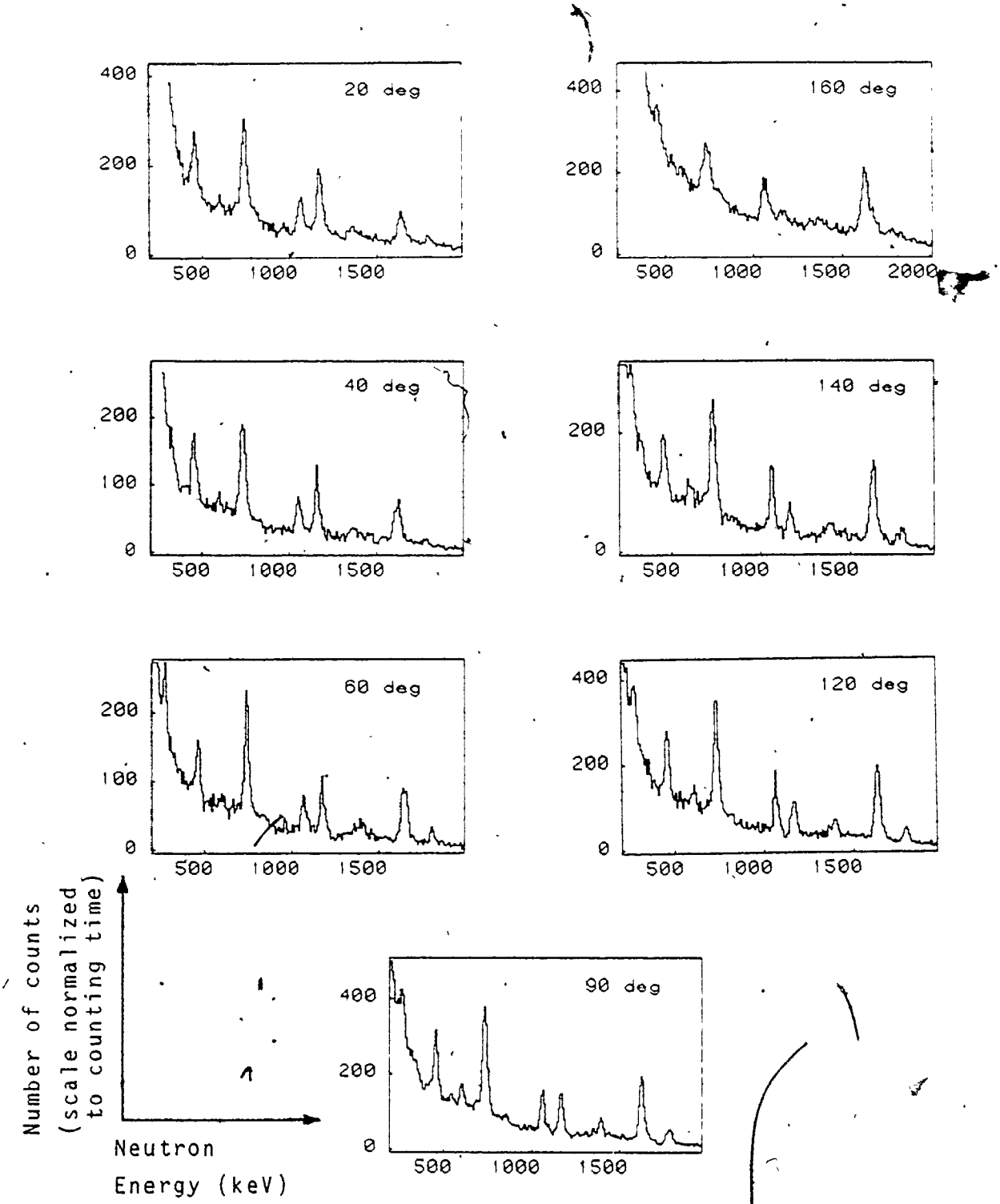

Figure 5.12 Photoneutron Spectrum of Pb-208 with Nickel Source at all Angles

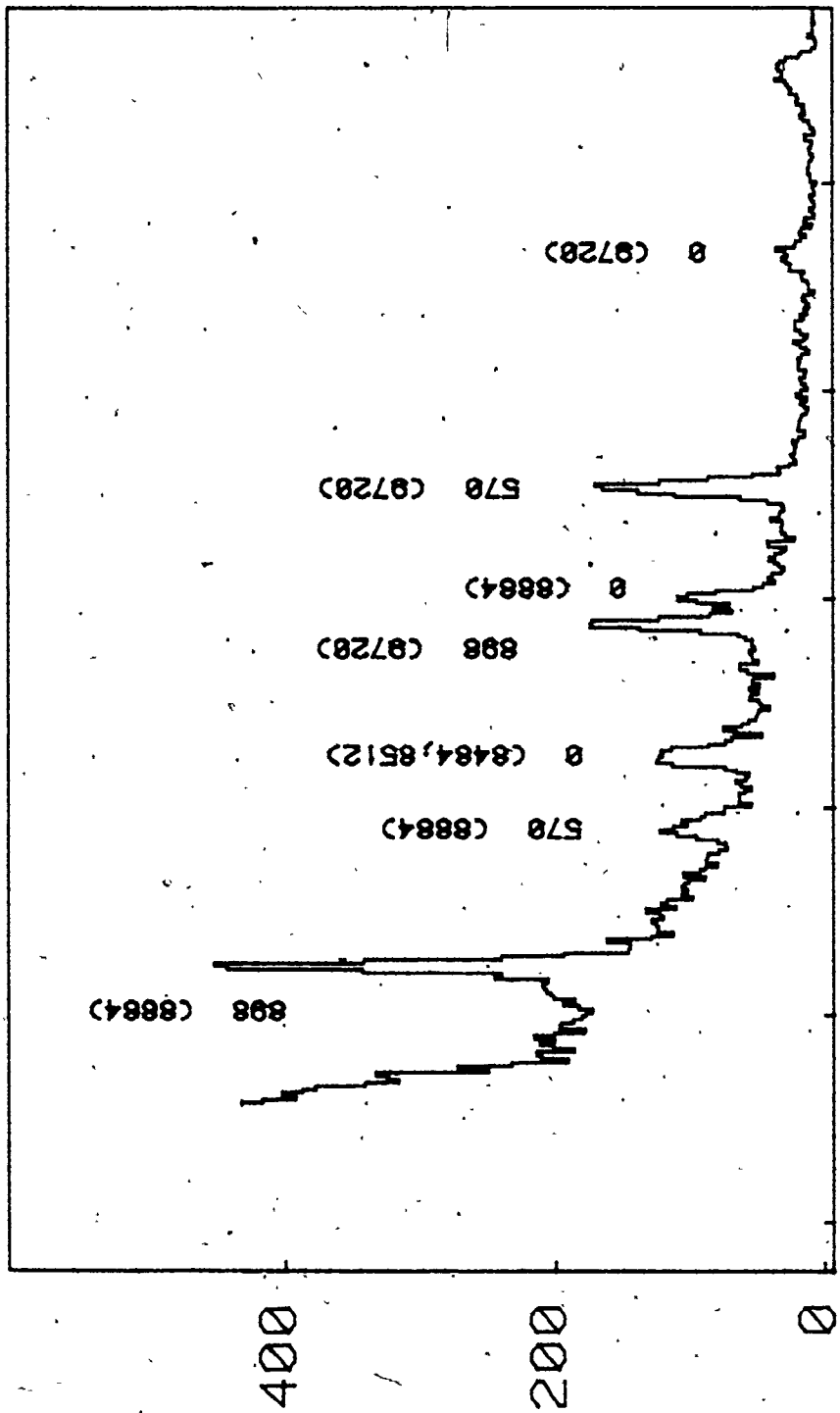

Figure 5.13 Photoneutron Spectrum of Pb-208 with Chromium Source at 90 degrees

Transitions are identified by photon energy E_γ and energy of the residual level of Pb-207, E_x.

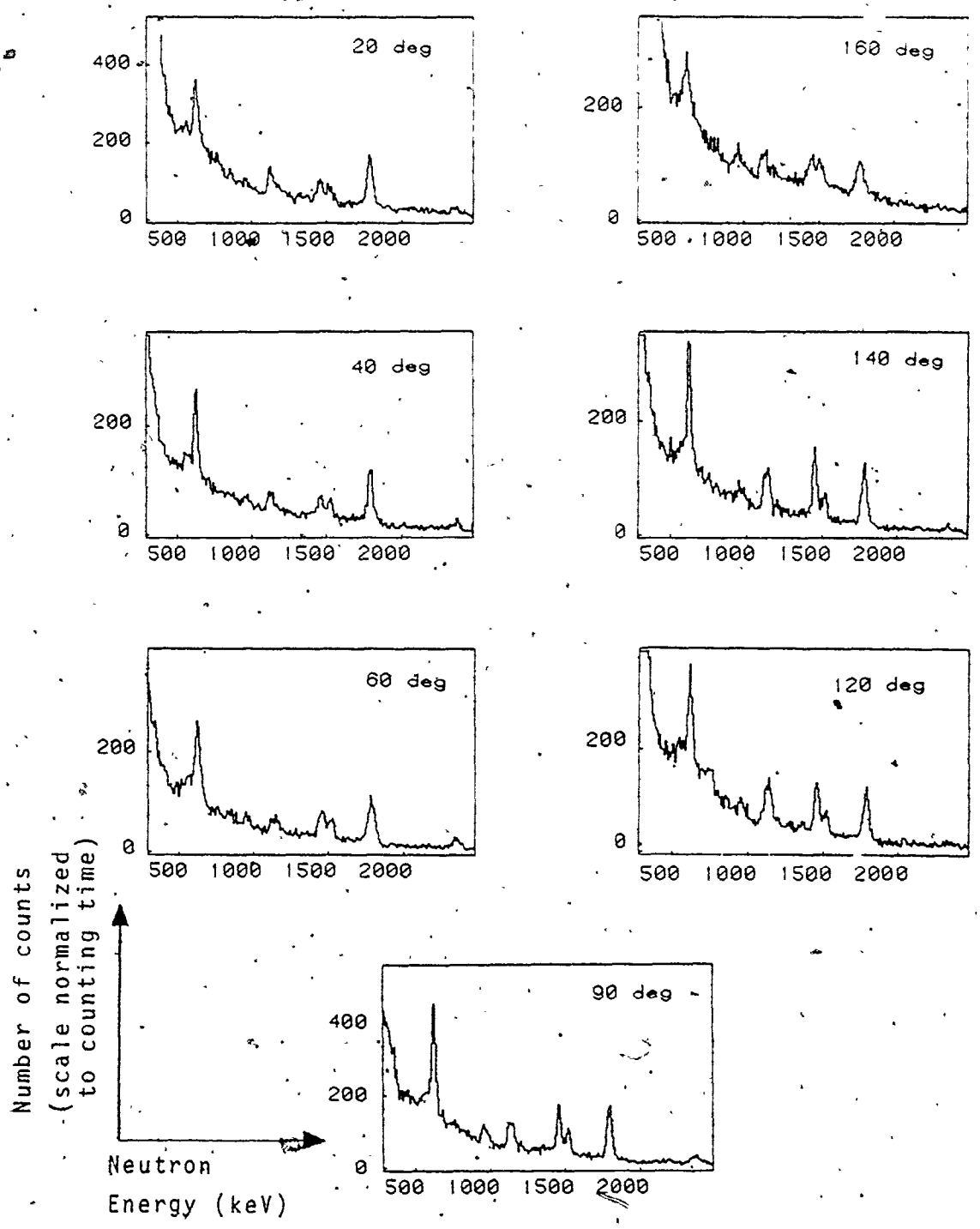

Figure 5.13 Photoneutron Spectrum of Pb-208 with Chromium Source at 90 degrees

5.2.2 THE ANGULAR DISTRIBUTIONS

The angular distribution coefficients a_ν and asymmetry parameter $I(E_\gamma, 55^o)$, determined from the fits of the measured counting rates, are listed for all measured transitions in ^{208}Pb in Tables 5.8B to 5.12B. Plots of the measured rates at each angle and the fitted functions $\Sigma_\nu a_\nu Q_\nu$ are shown in Figure 5.15 for all transitions to the ground state of ^{207}Pb and in Figures 5.16 and 5.17 for transitions to the 570 and 898 keV levels respectively.

In Figure 5.18, the values of a_1, a_2, a_3 and $I(E_\gamma, 55^o)$ are shown as a function of photon energy for each of the three lowest levels of ^{207}Pb. From this figure and Tables 5.8 to 5.12, non-zero values of a_1 indicate the existence of multipole mixing at all energies investigated except 11387 keV. However this energy is in the region of the Giant E2 Resonance (Fu62); so, the absence of asymmetry for this one transition should in no way be considered evidence for a lack of E2 strength. For the one observed transition at E_γ = 10054 keV which is near the Giant Quadrupole Resonance, a_1 is large which would indicate a large admixture. The a_3 term for the only observed transition at this energy is within error of zero but M1 mixing can be ruled out by the existence of the

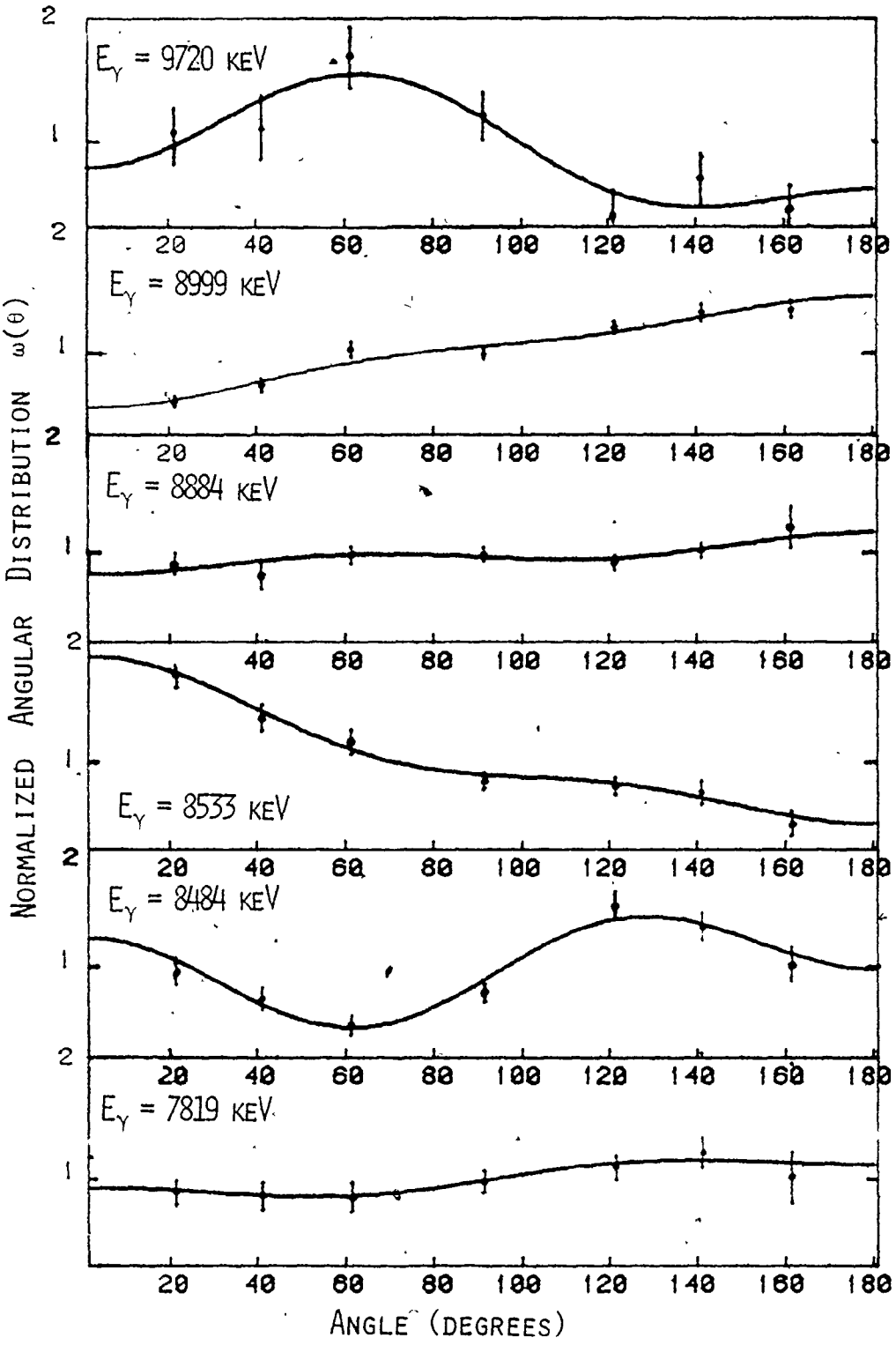

Figure 5.15 Pb-208 Angular Distributions
Transitions to the ground state of Pb-207
for E_γ = 9720,8999,8884,8533,8484 and 7819 keV.

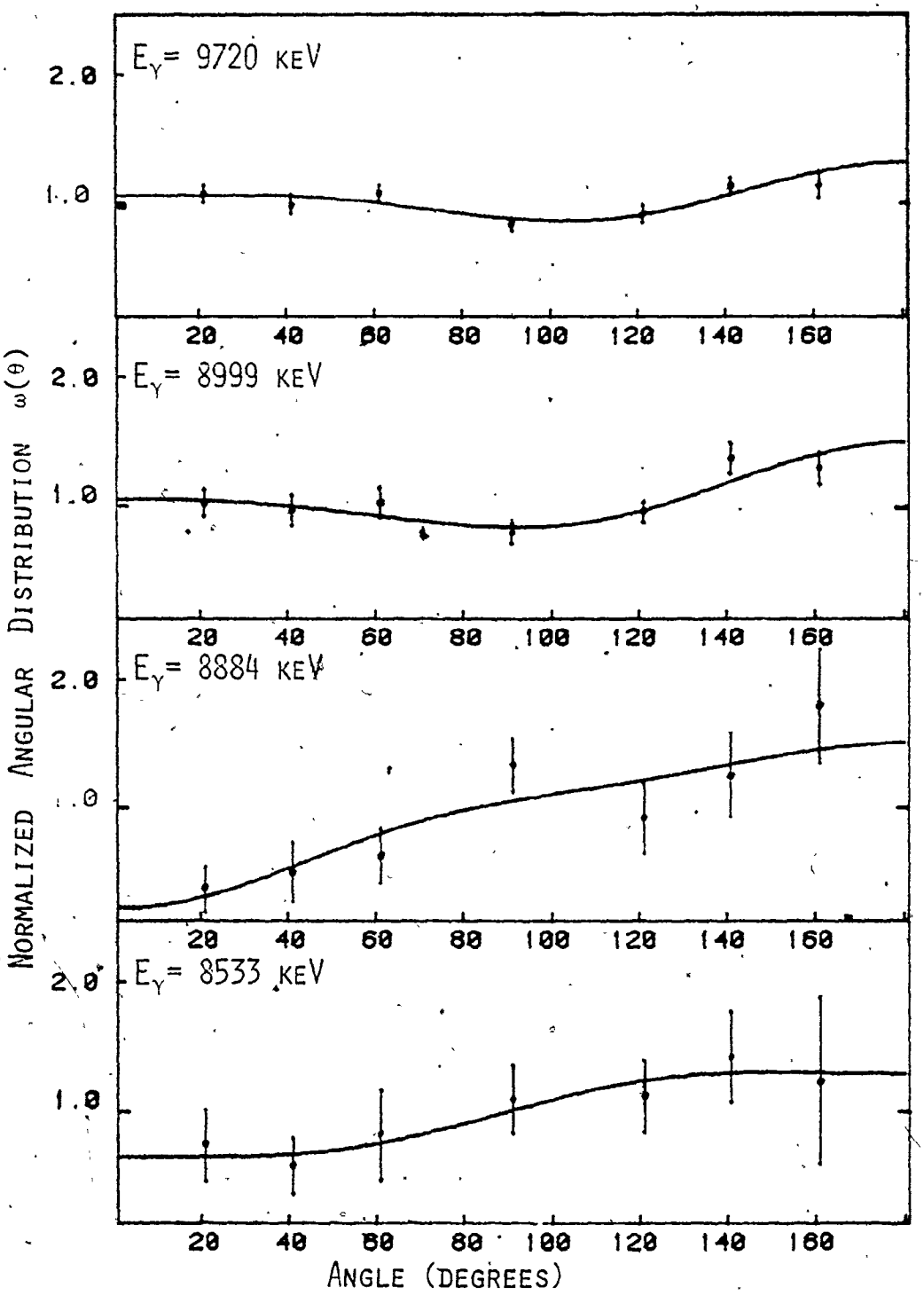

Figure 5.16 Pb-208 Angular Distributions
Transitions to the 570 keV level of Pb-207
for E_γ = 9720,8999,8884 and 8533 keV.

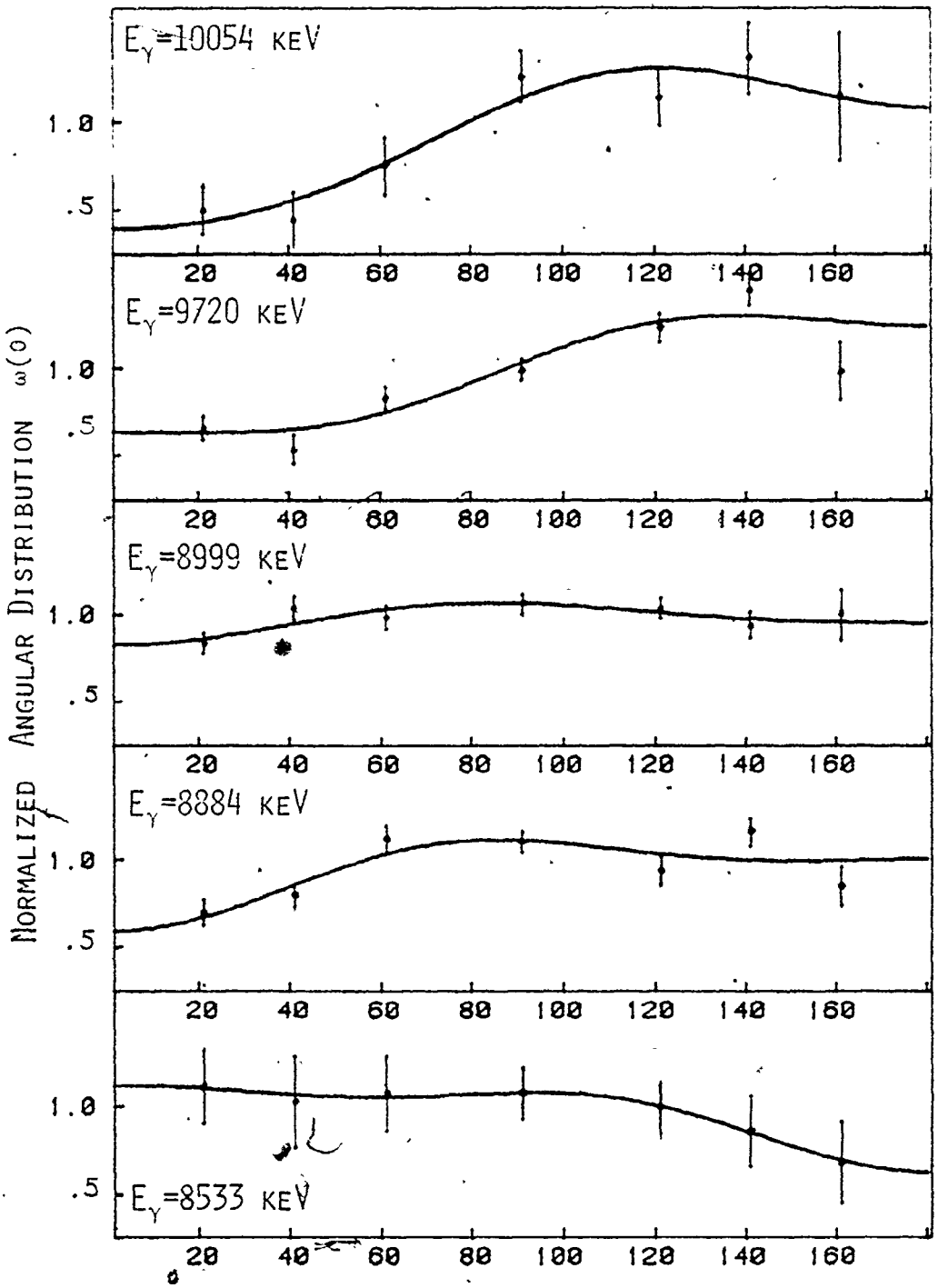

Figure 5.17 Pb-208 Angular Distributions
Transitions to the 898 keV level of Pb-207 for
E_γ = 10054,9720,8999,8884 and 8533 keV.

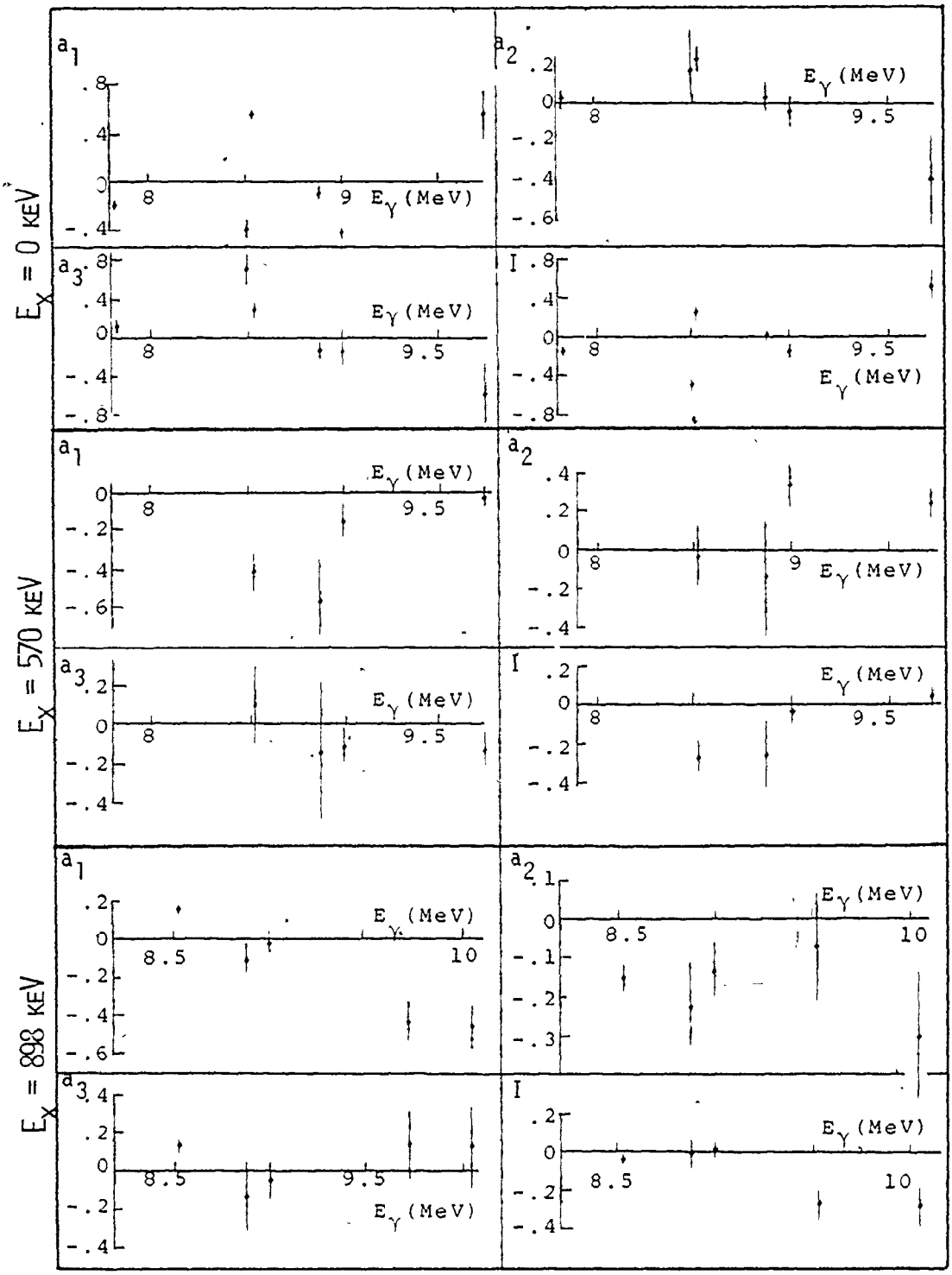

Figure 5.18 Variation of Angular Distribution Coefficients a_ν and Asymmetry Parameter $I(E_\gamma, 55°)$ with Photon Energy for $^{208}Pb(\gamma,n)^{207}Pb$

well known E2 resonance at 10.8 MeV. For all photons below 10 MeV, non-zero a_3 terms in the ground state transitions imply E1:E2 mixing. Thus, for lead 208, no evidence of M1 strength can be inferred from this experiment. Accordingly, all calculations of the mixing ratio will be made for E2:E1 admixtures only.

Finally, it can be seen from Figure 5.18 that forward peaked cross-sections ($a_1>0$) do occur for some transitions; in this case 8999 keV and 9720 keV for transitions to the ground state of ^{207}Pb, and at 8533 keV for E_x = 898 keV. The transitions to the 898 keV ($j=5/2^-$) level, in Figure 5.18, show a general trend with photon energy for a_1 and $I(E_\gamma,55^0)$. This is not found for the ground state or the 570 keV level transitions. The lack of any smooth variation of the angular distribution coefficients, and especially such large jumps in a_1, as seen in Figure 5.18 for the ground state transition between 8484 keV and 8533 keV, would imply that the individual level resonances are significant in this energy region. This individual level structure in the (γ,n) cross-section of ^{208}Pb has already been seen (Ho79) below 8.4 MeV. As such, any attempt to provide smooth functions of a_ν with photon energy is not likely to be too reliable in this energy region.

5.2.3 MULTIPOLE MIXING

Again, asymmetry seen at all photon energies below 10 MeV implies that multipole mixing does occur. Non-zero a_3 terms here imply E2:E1 mixing. No asymmetry is seen at 11387 keV but since this is near the Giant Electric Quadrupole strength and since a lack of asymmetry does not rule out multiple mixing, no arguments for a lack of mixing can be made

The mixing ratio α is calculated in the same manner as explained in section 5.1.3, using the angular distribution expansions and the experimentally determined values of a_1 and $I(E_\gamma, 55^0)$. Table 5.13 is a list of the neutron transmission probabilities and phase angles used in the reaction matrix elements. The calculated values of the mixing ratio α and phase angle δ are listed in Table 5.14 for each observed transition.

The data from Table 5.14 can be summarized as follows

E_γ = 10054 keV , $.04 < \alpha < .39$
E_γ = 9720 keV , $.08 < \alpha < .23$
E_γ = 8999 keV , $.01 < \alpha < .25$
E_γ = 8884 keV , $.05 < \alpha < .24$
E_γ = 8533 keV , $.04 < \alpha < .19$
E_γ = 7819 keV , $.02 < \alpha < .85$.

The above values show that the mixing is similar at all photon energies studied, implying that no nearby single level resonances heavily influenced the mixing.

5.3 CONCLUSIONS AND RECOMMENDATIONS

The major finding of this work is the existence of the mixing of multipole excitations as evidenced in the asymmetry of the photoneutron angular distributions. The nature of the asymmetry can be used to rule out M1 contributions at all energies except 8884 keV for ^{206}Pb, since only E2:E1 mixing can account for a non-zero value of a_3 in the angular distribution function. Of course, since the photons have such precise energies and since significant fine structure is expected in the photoneutron cross-section between 8 and 11 MeV, the angular distributions can be significantly affected by a nearby individual level. For these reasons, Compton monochromator or tagged photon techniques would be of great use both to enable the photon energy to be varied and to average over individual levels.

The statistical compound model predictions of mixing ratios are useful because no a priori assignment of E2 strength is necessary. However, because the

interactions may have significant direct-semi-direct natures, the uncoupling of the entrance and exit channels may not be entirely justified. As can be seen from the results of this analysis, reasonable, if not precise determinations of the extent of multipole mixing can be made. The assumptions used in this approach, notably the sign and magnitude of the various ℓ-wave neutron phase angles, do introduce some uncertainties into the calculations, but because of the large number of terms in the expansions, the errors would likely cancel to some extent. Also, since an upper and lower bound to the mixing ratio is the best that can be obtained using this method, these model dependent uncertainties should not be too significant.

The conclusions can be summarized as follows:

1. Over the energy range of 7.8 to 11 MeV, E1 excitation dominates, but E2 contributions are seen at all photon energies for both lead 206 and 208.
2. M1 excitation can be ruled out for both isotopes for E_γ < 11 MeV, except at 8884 keV in ^{206}Pb.
3. The statistical compound nucleus model in which the entrance and exit channels are uncoupled does not lead to precise determination of the mixing ratio and phase shift for E1:E2 admixtures but does give reasonable order of magnitude values.

TABLE 3.1.

MATERIAL PROPERTIES AND ISOTOPIC ANALYSIS OF THE SEPARATED LEAD SAMPLES

LEAD 206

Mass		47.079 g
Length		24 mm
Diameter		15 mm
Isotopic Analysis:	Pb 204	< .01 %
	Pb 206	99.80 ± .02 %
	Pb 207	0.20 ± .02 %
	Pb 208	< .03 %

LEAD 208

Mass		40.71 g
Length		18 mm
Diameter		16 mm
Isotopic Analysis:	Pb 204	< .05 %
	Pb 206	.17 ± .05 %
	Pb 207	.69 ± .05 %
	Pb 208	99.14 ± .10 %

TABLE 5.1

EXPECTED AND OBSERVED PHOTONEUTRON TRANSITIONS IN THE REACTION $^{206}Pb(\gamma,n)^{205}Pb$

Neutron Energies (keV) $E_{n'} = \frac{206}{205}(E_\gamma - Q - E_x)$

Level energy in the Residual Nucleus ^{205}Pb (level spin and parity shown) $E_{n'}$ (keV)		PHOTON ENERGY (keV)					
		NICKEL		CHROMIUM			
		8999	8533	9720	8884	8512	8484
1374.3	$(3/2^-, 1/2^-)$			(255)*			
1264.7	$(5/2^-)$			363			
1043.7	$(7/2^-)$			583			
1013.8	$(13/2^+)$			613			
999.1	$(1/2^-, 3/2^-)$			628			
987.6	$(9/2^-)$			639			
803.5	$(3/2^-, 1/2^-)$	105		(822)*			
761.4	$(5/2^-)$	147		865			
703.4	$(5/2^-)$	205		923	91		
576.2	$(3/2^-)$	331		1049	217		
262.8	$(3/2^-)$	643	179	1360	528	158	130
2.3	$(1/2^-)$	903	439	1620	788	418	390
0	$(5/2^-)$	905	441	1622	790	420	392

* Nucl. Data. Feb. 1978

Transition observed at some angles, no angular distribution calculated.

All transitions outlined were observed.

Transitions grouped together were observed but could not be resolved.

TABLE 5.2

ANGULAR DISTRIBUTION FOR $^{206}Pb(\gamma,n)^{205}Pb$. : E_γ = 8999 keV (NICKEL)

A. Reaction Rates : Counts per 100 minutes (normalized by beam monitor).

Energy Level of Residual Nucleus ^{205}Pb (keV) → Neutron Energy (keV) → Angle (degrees)	0,2keV doublet 905,903 keV	263 keV 643 keV	576 keV 331 keV
20	6.12±.39	6.10±.42	2.57±.32
40	9.73±.54	7.18±.59	4.10±.42
60	13.69±.64	9.52±.77	5.47±.45
90	16.59±.42	9.45±.39	6.38±.37
120	14.93±.38	13.45±.39	8.59±.31
140	10.85±.64	17.92±.78	8.37±.61
160	5.63±.49	14.01±.74	8.75±.63

B. Angular Distribution Coefficients and Asymmetry Parameter

Energy Level of Residual Nucleus ^{205}Pb (keV)	a_0	a_1	a_2	a_3	$I(E_\gamma,55^o)$
0,2 (doublet)	1	-.04±.03	-.73±.04	+.11±.05	-.06±.03
263	1	-.52±.11	-.08±.14	+.05±.20	-.31±.11
576	1	-.52±.06	-.15±.09	-.02±.10	-.40±.06

TABLE 5.3

ANGULAR DISTRIBUTIONS FOR $^{206}Pb(\gamma,n)^{205}Pb$: E_γ = 9720 keV (CHROMIUM)

A. Reaction Rates : Counts per 100 minutes (normalized to beam monitor).

Energy Level of Residual Nucleus ^{205}Pb (keV) → Neutron Energy (keV) → Angle (degrees)	0,2 doublet 1622,1620	263 1360	576 1049	761 865	804 822	triplet*	1044 583
20	15.85±.69	8.17±.54	2.43±.37	10.54±.66	2.15±.46	10.55±.69	8.12±.66
40	17.18±.55	7.90±.44	2.52±.31	7.34±.48	2.37±.46	8.66±.55	6.01±.55
60	19.66±.43	8.13±.33	2.42±.22	7.82±.38	.94±.22	10.18±.44	6.46±.40
90	20.83±.64	9.04±.52	3.88±.41	6.09±.49	-	10.55±.65	5.76±.54
120	16.35±.52	10.56±.45	3.34±.33	7.56±.97	-	9.78±.56	5.22±.51
140	16.04±.45	10.66±.40	3.30±.29	10.31±.44	.70±.24	9.46±.46	6.00±.44
160	14.99±.57	11.61±.56	3.29±.40	9.25±.59	-	10.89±.63	6.18±.56

*Unresolved triplet, E_γ = 988,999, 1014 keV, E_n = 639,628,613 keV, likely from E_x = 999 keV because of low spin.

B. Angular Distribution Coefficients and Asymmetry Parameter.

Energy Level of Residual Nucleus ^{205}Pb (keV)	a_0	a_1	a_2	a_3	$I(E_\gamma, 55^0)$
0,2 (doublet)	1	+.06±.03	-.22±.05	-.11±.05	+.08±.02
263	1	-.21±.02	+.06±.03	+.04±.03	-.13±.02
576	1	-.20±.07	-.13±.13	+.15±.14	-.17±.06
761	1	-.06±.10	+.36±.16	+.07±.18	-.06±.08
988,999,1014 triplet	1	-.02±.06	-.01±.10	-.05±.12	+.01±.05
1044	1	+.12±.06	+.18±.11	-.00±.12	+.07±.06

TABLE 5.4

ANGULAR DISTRIBUTION FOR $^{206}Pb(\gamma,n)^{205}Pb$: E_γ = 8884 keV/8512,8484 keV

A. Reaction Rates : Counts per 100 minutes (normalized to beam monitor)

Photon Energy E_γ keV →	8884	8884	8884	8512,8484*
Level Energy E_x keV →	0,2 doublet	263	576	0,2 doublet
Neutron Energy E_n keV →	790,780	528	217	420,418,392,390
Angle (degrees) 20	8.44±.68	8.79±.71	†	4.30±.69
40	9.51±.59	6.51±.58	†	5.85±.59
60	13.09±.46	7.16±.43	†	6.26±.40
90	16.57±.74	6.09±.64	2.04±.61	8.68±.73
120	15.83±.64	8.06±.59	3.61±.56	8.25±.63
140	14.23±.52	8.77±.50	3.21±.48	6.41±.47
160	13.41±.66	9.69±.71	2.56±.93	2.84±.54

*Contribution from 8484 and 8512 keV photons unresolved.

†Low energy peak obscured by large neutron background.

B. Angular Distribution Coefficients and Asymmetry Parameter

Photon Energy E_γ(keV)	Energy Level E_x(keV)	a_0	a_1	a_2	a_3	$1(E_\gamma, 55^o)$
8884	0,2 doublet	1	-.21±.03	-.34±.04	+.01±.05	-.12±.03
8884	263	1	-.13±.06	+.26±.11	+.03±.12	-.08±.06
8512,8484	0,2 doublet	1	-.04±.05	-.60±.08	+.33±.09	-.14±.04

TABLE 5.5 NEUTRON TRANSMISSION PROBABILITIES (Au 62) AND PHASE ANGLES (Mo 63) FOR ALL TRANSITIONS $^{205}Pb(r,n)^{206}Pb$

E_r (keV)	E_x (keV)	J^{π}_{A-1}	E_n (keV)	$T_0^{1/2}$	$T_1^{1/2}$	$T_1^{3/2}$	$T_2^{3/2}$	$T_2^{5/2}$	$T_3^{5/2}$	$T_3^{7/2}$	ϕ_0	ϕ_1	ϕ_2	ϕ_3
9720	263	3/2⁻	1360	.627	.590	.681	.410	336	.148	.273	-142°	- 74°	- 29°	- 7°
8999	263	3/2⁻	643	.534	.386	.465	.180	.140	.015	.024	- 97°	- 38°	- 8°	- 1°
8884	263	3/2⁻	528	.508	336	.408	.139	107	.009	.014	- 89°	- 31°	- 6°	- 1°
9720	576	3/2⁻	1049	.598	.525	.610	.326	.265	.067	.120	-124°	- 59°	- 21°	- 4°
8999	576	3/2⁻	330	.441	.225	.278	.058	.048	.004	.006	- 71°	- 19°	- 2°	- 1°
8884	576	3/2⁻	217	.370	.150	.190	.026	.021	∿0	∿0	- 57°	- 12°	- 1°	-
9720	761	5/2⁻	865	-	.471	.558	.269	.212	.036	.068	-	- 50°	- 14°	- 2°
9720	1044	7/2⁻	583	-	-	.365	-	.161	.011	.019	-	- 34°	- 7°	- 1°

TABLE 5.6 LEAD 206 MIXING RATIOS

1. E2 : E1 Mixing

E_γ (keV)	E_x (keV)	a_1/a_0 Calculations. Mixing Ratio α Range	$\bar{\alpha}$	δ Phase Angle °	$I(E,55)$ Calculations. Mixing Ratio α Range	$\bar{\alpha}$	δ Phase Angle (°)
9720	263	.013-.48	$.015^{+.004}_{-.002}$	60-204	.025-.48	$.04^{+.01}_{-.02}$	.82-211
	576	.008-.54	$.02^{+.03}_{-.01}$	51-204	.046-.54	$.15^{+.19}_{-.10}$	77-193
	761	0 -.25	$.001^{+.005}_{-.001}$	43-221	0 -.25	$.004^{+.018}_{-.004}$	43-221
	1043	.0003-.25	$.001^{+.002}_{-.001}$	64-237	10^{-5}-.25	$.001^{+.003}_{-.001}$	61-240
8999	263	.12 -.58	$.30^{+.11}_{-.18}$	87-164	*	*	*
	576	.10 -.64	$.16^{+.10}_{-.06}$	79-171	.12 -.64	$.17^{+.10}_{-.05}$	77-163
8884	263	.002-.59	$.008^{+.009}_{-.006}$	37-203	.001-.59	$.018^{+.045}_{-.017}$	28-199

2. M1 : E1 Mixing (For E_γ = 8884 keV only; $a_3 \neq 0$ for other energies)

E_γ (keV)	E_x (keV)	Mixing Ratio δ Range	$\bar{\delta}$	Phase Angle δ (degrees)
8884	263	.001 - .99	$.003^{+.005}_{-.002}$	232-45

* No solution for mixing ratio

TABLE 5.7 EXPECTED AND OBSERVED PHOTONEUTRON TRANSITIONS IN THE REACTION $^{208}Pb(\gamma,n)^{207}Pb$

Level Energy of the Residual Nucleus Pb 207		Neutron Energy (keV) $E_n = \frac{207}{208}(E_\gamma - Q - E_x)$								
	E_γ (keV)	9720	8884	8512	8484	8999	8533	7819	11387	11054
E_x (keV)	Spin and Parity									
2682	$7/2^+$								1354	
2624	$5/2^+$								1388	62
2340	$7/2^-$								1671	344
1633	$13/2^+$	716							2375	1048
898	$3/2^-$	1447	615	245	217	729	266		3106	1779
570	$5/2^-$	1773	941	573	543	1056	592		3432	2106
0	$1/2^-$	2341	1509	1139	1111	1623	1159	449	4000	2673

TABLE 5.8

ANGULAR DISTRIBUTIONS FOR $^{208}Pb(\gamma,n)^{207}Pb$: E_γ = 8999 keV

A. Reaction Rates : Counts per 100 minutes (normalized to beam monitor)

E_x (keV) → E_n (keV) →	0 1623	570 1056	898 729
Angle(degrees)			
20	6.65±.57	7.86±.76	14.90± .98
40	8.40±.70	7.40±.87	18.45±1.20
60	12.41±.80	7.85±.86	17.54±1.17
90	11.93±.51	6.05±.57	18.84± .95
120	14.73±.65	7.29±.60	18.43±1.00
140	16.46±.85	10.43±.87	16.70±1.27
160	16.81±.88	9.86±.90	17.76±2.54

B. Angular Distribution Coefficients and Asymmetry Paramerer coefficients normalized to a_0.

E_x (keV)	a_0	a_1	a_2	a_3	$I(E_\gamma, 55^o)$
0	1	-.41±.06	-.04±.08	-.15±.11	-.17±.06
570	1	-.15±.08	+.33±.11	-.11±.14	-.04±.07
898	1	-.02±.04	-.13±.07	-.05±.08	+.01±.04

TABLE 5.9

ANGULAR DISTRIBUTIONS FOR $^{208}Pb(\gamma,n)^{207}Pb$: E_γ = 8533 keV

A. Reaction Rates : Counts per 100 minutes (normalized to beam monitor)

E_x (keV) →	0	570	898
E_n (keV) →	1159	592	266
Angle (degrees)			
20	13.48±.81	1.65± .61	7.72±1.45
40	10.64±.84	1.31± .47	7.15±1.81
60	9.07±.80	1.83± .77	7.47±1.48
90	6.46±.53	2.44± .58	7.47±1.01
120	6.12±.53	2.49± .61	6.73±1.21
140	5.69±.73	3.17± .77	5.98±1.40
160	3.60±.79	2.75±1.42	4.75±1.62

B. Angular Distribution Coefficients and Asymmetry Parameter E_γ = 8533 keV

E_x (keV)	a_0	a_1	a_2	a_3	$I(E_\gamma, 55^o)$
0	1	+.56±.04	+.23±.06	+.28±.08	+.23±.07
570	1	-.41±.10	-.03±.16	+.10±.20	-.27±.09
898	1	+.16±.02	-.15±.03	+.12±.04	+.04±.02

TABLE 5.10

ANGULAR DISTRIBUTIONS FOR $^{208}Pb(\gamma,n)^{207}Pb$: E_γ = 9720 keV

A. Reaction Rates : Counts per 100 minutes (normalized to beam monitor)

E_x (keV) →	0	570	898
E_n (keV) →	2341	1773	1447
Angle (degrees)			
20	.77±.19	6.50±.39	2.67±.26
40	.81±.20	6.00±.40	2.18±.31
60	1.28±.20	6.52±.36	3.36±.24
90	.89±.15	5.11±.28	4.00±.23
120	.25±.16	5.60±.37	4.75±.32
140	.49±.16	6.85±.39	5.82±.35
160	.26±.18	6.94±.60	3.97±.64

B. Angular Distribution Coefficients and Asymmetry Parameter coefficients normalized to a_0

E_x (keV)	a_0	a_1	a_2	a_3	$I(E_\gamma, 55^0)$
0	1	+.56±.17	-.39±.23	-.60±.32	+.53±.16
570	1	-.03±.05	+.23±.08	-.13±.10	+.03±.05
898	1	-.42±.10	-.07±.14	+.13±.18	-.28±.08

TABLE 5.11

ANGULAR DISTRIBUTIONS FOR $^{208}Pb(\gamma,n)^{207}Pb$: E_γ = 8884 keV

A. Reaction Rates : Counts per 100 minutes (normalized to beam monitor).

E_x (keV) →	0	570	898
E_n (keV) →	1509	941	613
Angle (degrees)			
20	2.08±.20	.57±.26	5.93±.62
40	1.82±.24	.76±.33	6.74±.55
60	2.24±.17	.94±.30	9.40±.63
90	2.26±.13	1.97±.30	9.27±.48
120	2.10±.14	1.37±.39	7.91±.65
140	2.34±.14	1.86±.49	9.75±.64
160	2.79±.40	2.63±.64	7.16±.89

B. Angular Distribution Coefficients and Asymmetry Parameter coefficients normalized to a_0

E_x(keV)	a_0	a_1	a_2	a_3	$I(E_\gamma, 55^o)$
0	1	-.09±.05	+.03±.08	-.14±.10	.01±.04
570	1	-.56±.19	-.14±.29	-.14±.35	-.25±.17
898	1	-.11±.08	-.23±.12	-.13±.17	-.01±.08

TABLE 5.12

ANGULAR DISTRIBUTION FOR $^{208}Pb(\gamma,n)^{207}Pb$: E_γ = 8484,8512 keV (Cr), 7819 keV (Ni), 10054, 11387 keV (^{60}Ni)

A. Reaction Rates : Counts per 100 minutes (normalized to beam monitor)

Photon Energy E_γ (keV) →	8484,8512*	7819	10054	11387
Level Energy E_x (keV) →	0	0	898	2624
Neutron Energy E_n (keV) →	1111	449	1779	1388
Angle (degrees) 20	4:51±.50	7.95± .90	1.16±.31	2.24±.48
40	3.41±.43	7.65±1.07	1.03±.36	1.65±.53
60	2.38±.36	7.59±1.13	1.74±.37	2.88±.54
90	3.66±.37	8.84± .84	2.92±.33	2.36±.45
120	7.15±.52	9.91± .89	2.65±.37	2.44±.39
140	6.31±.52	11.11±1.16	3.15±.46	2.57±.56
160	4.79±.68	9.13±2.03	2.65±.83	2.49±.58

*Contributions from 8484 and 8512 keV photons unresolved

B. Angular Distribution Coefficients and Asymmetry Parameter

Photon Energy E_γ (keV)	Energy Level E_x (keV)	a_0	a_1	a_2	a_3	$I(E_\gamma, 55^0)$
8484,8512	0	1	-.39±.08	+.17±.12	+.70±.15	-.49±.07
7819	0	1	-.20±.04	+.03±.06	+.12±.07	-.16±.03
10054	898	1	-.45±.11	-.30±.17	+.12±.21	-.29±.10
11387	2624	1	-.08±.11	-.06±.16	-.07±.20	-.02±.10

TABLE 5.13 NEUTRON TRANSMISSION PROBABILITIES (Au62) AND PHASE ANGLES (Mo63) FOR ALL TRANSITIONS $^{208}Pb(\gamma,n)^{207}Pb$

E_γ (keV)	E_x (keV)	J^π_{A-1}	E_n (keV)	$T_0^{1/2}$	$T_1^{1/2}$	$T_1^{3/2}$	$T_2^{3/2}$	$T_2^{5/2}$	$T_3^{5/2}$	$T_3^{7/2}$	$T_4^{9/2}$	ϕ_s	ϕ_p	ϕ_d
9720	0	1/2⁻	2341	.661	.738	.812	-	.465	-	.821	-	-186°	-113°	-58°
8999	0	1/2⁻	1623	.630	.662	.748	-	.375	-	.450	-	-155°	- 85°	-37°
8884	0	1/2⁻	1509	.623	.643	.732	-	.355	-	378	-	-149°	- 80°	-34°
8533	0	1/2⁻	1159	.596	.578	.668	-	.284	-	185	-	-131°	- 64°	-23°
8484/ 8512	0	1/2⁻	1122	567	568	.658	-	276	-	.165	-	-129°	- 63°	-23°
7819	0	1/2⁻	449	469	.307	.378	-	.079	-	.010	-	- 81°	- 26°	- 4°
9720	570	5/2⁻	1773	-	.683	.765	.462	.399	.318	.540	.025	-	-97°	-46°
8999	570	5/2⁻	1056	-	.550	640	.315	.260	076	.136	.003	-	-59°	-20°
8533	570	5/2⁻	592	-	.380	.462	159	.121	.012	019	<.001	-	-35	- 7°
10054	898	3/2⁻	1779	.639	.684	.767	.464	.400	.320	551	-	-169°	-98°	-46°
9720	898	3/2⁻	1447	.619	.631	.722	.408	342	.189	.336	-	-150°	-81°	-34°
8999	898	3/2⁻	729	.537	.442	.529	.211	166	.024	.042	-	-104°	-43°	-11°
8884	898	3/2⁻	615	.511	.390	.473	.169	.130	.015	.024	-	- 95°	-36°	- 8°
8533	898	3/2⁻	266	.405	.185	.230	.035	.025	.003	.004	-	- 63°	-15°	- 2°

TABLE 5.14 LEAD 208 MIXING RATIOS

E_γ (keV)	E_x (keV)	a_1/a_0 Calculations			$I(E_\gamma,55^\circ)$ Calculations		
		α Mixing Ratio		δ Phase	α Mixing Ratio		δ Phase
		Range	$\bar{\alpha}$	Angle (°)	Range	$\bar{\alpha}$	Angle (°)
10054	898	.03 -.39	$.07^{+.08}_{-.04}$	63-180	.04 -.39	$.16^{+.23}_{-.12}$	81-188
9720	0	.01 -.41	$.03^{+.03}_{-.02}$	55-200	.04 -.41	$.11^{+.40}_{-.07}$	89-200
	570	0 -.23	$.091^{+.009}_{-.001}$	356-175	0 -.23	$.05^{+.18}_{-.05}$	315-213
	898	.03 -.44	$.06^{+.06}_{-.03}$	72-192	.08 -.44	<.44	103-191
8999	0	.01 -.50	$.013^{+.012}_{-.008}$	55-197	.005-.50	$.02^{+.01}_{-.01}$	70-227
	570	.001-.25	$.008^{+.012}_{-.006}$	44-207	0 -.25	$.002^{+.015}_{-.002}$	35-217
	898	0 -.53	$.0002^{+.0014}_{-.0002}$	33-213	0 -.53	$.01^{+.52}_{-.01}$	84-264
8884	0	10^{-5}-.52	$.0002^{+.0003}_{-.0002}$	37-215	10^{-5}-.52	$10^{-5}+10^{-5}_{-10^{-5}}$	57-237
	570	.05 -.24	<.24	90-171	.007-.24	<.24	60-201
	898	.001-.54	$.005^{+.012}_{-.004}$	35-209	0 -.54	$.01^{+.53}_{-.01}$	84-264
8533	0	.04 -.62	$.05^{+.01}_{-.01}$	64-230	.03 -.62	$.04^{+.02}_{-.02}$	75-209
	570	.02 -.19	$.03^{+.03}_{-.02}$	87-206	.02 -.19	$.07^{+.12}_{-.05}$	92-201
	898	.01 -.66	$.009^{+.003}_{-.002}$	51-207	.001-.66	$.003^{+.003}_{-.002}$	38-211
7819	0	.004-.85	$.007^{+.003}_{-.003}$	44-208	.02 -.35	$.03^{+.01}_{-.01}$	47-195

APPENDIX I

PHOTONEUTRON ANGULAR DISTRIBUTION OF THE 8884keV RESONANCE IN ^{49}Ti

If a photoneutron energy matches a single level resonance in a nucleus, there should be almost no multipole mixing. The photoneutron spectrum from such a resonance would be symmetric about 90 degrees and would be of the form

$$\omega(\theta) = 1 + a_2 P_2(\cos\theta) \quad \text{AI.1}$$

A resonance was found in Titanium-49 (Be78) at 8884 keV which matched one of the strong chromium photon energies. The (γ,n) transition, from the $^{7}/_{2}^{-}$ ground state, involved E1 excitation to the $^{7}/_{2}^{+}$ intermediate level of ^{49}Ti followed by the emission of an $\ell=4$ neutron of 741 keV, leaving the residual nucleus ^{48}Ti in the 0^{+} ground state. The spin and parity of the intermediate level had been deduced from photon scattering and Compton polarimeter experiments (Be78).

This transition was investigated to check for any asymmetry which could arise from changes in the geometry of the beam, target and at different angles. Measurements of the photoneutron spectra were made at six angles from 20 to 140 degrees.

The angular distribution (Figure A.I-1) was

$$\omega(\theta) = 1 + (.01\pm.05)P_1(\cos\theta) + (.41\pm.07)P_2(\cos\theta) - (.03\pm.12)P_3. \qquad \text{A.I-2}$$

This result agreed with a previous study (Be78) which determined $a_2 = .40\pm.08$. The lack of asymmetry as expected for a resonance transition, indicated that there was no variation in the counting efficiency at different angles which could have been due to the scattering of neutrons or photons in the beam by the target or to changes in the target-detector solid angle.

A value of a_2 could be predicted by the theoretical expansion of the angular distribution (Ca71). The ratio of the A_2 to A_0 terms gives a unique value of a_2 since only one reaction channel is permitted, thus eliminating the reaction channel matrix element. This predicted value from equation 2.12 is

$$a_2 = \frac{A_2}{A_0} = \frac{(2x2+1)\begin{pmatrix}4&4&2\\0&0&0\end{pmatrix}\begin{pmatrix}1&1&2\\-1&1&0\end{pmatrix}\begin{Bmatrix}4&7/2&1/2\\7/2&4&2\end{Bmatrix}\begin{Bmatrix}1&7/2&7/2\\7/2&1&2\end{Bmatrix}}{(2x0+1)\begin{pmatrix}4&4&0\\0&0&0\end{pmatrix}\begin{pmatrix}1&1&0\\-1&1&0\end{pmatrix}\begin{Bmatrix}4&7/2&1/2\\7/2&4&0\end{Bmatrix}\begin{Bmatrix}1&7/2&7/2\\7/2&1&0\end{Bmatrix}}$$

$$= .476. \qquad \text{A.I-3}$$

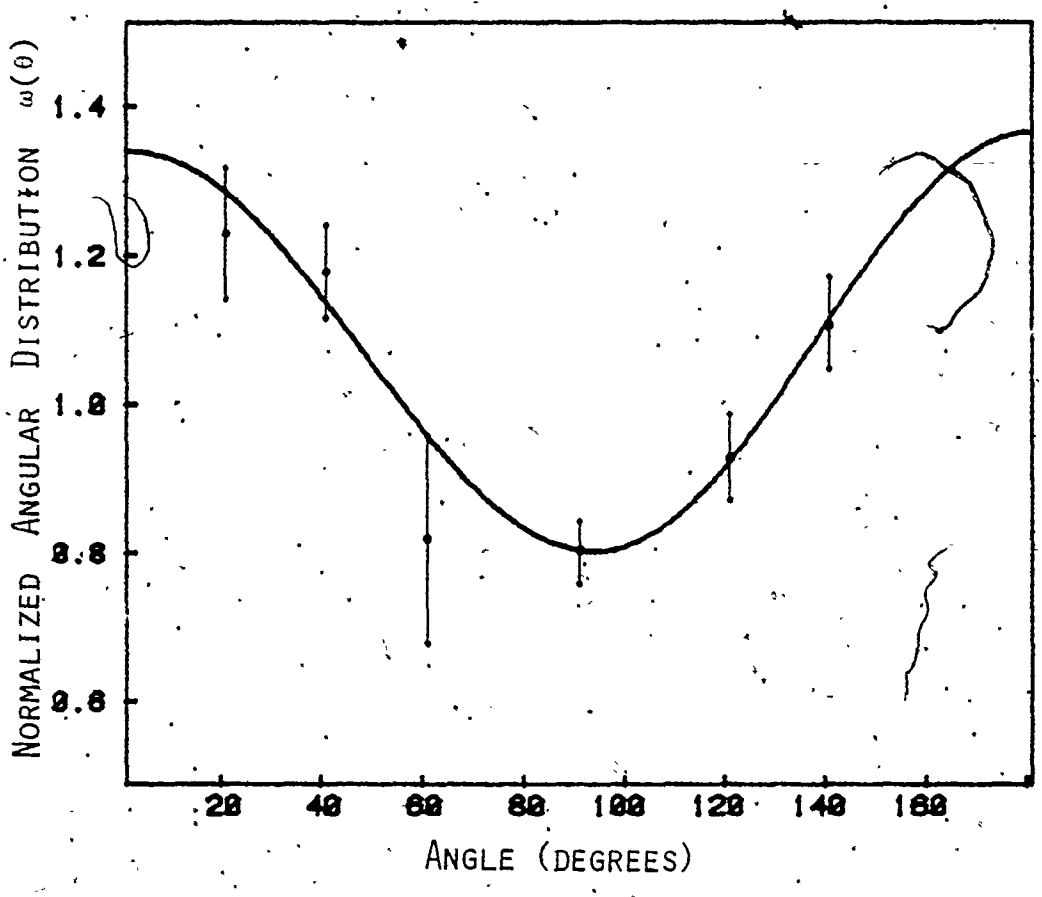

Figure A I. 1 Photoneutron Angular Distribution for the Resonance in ^{49}Ti at 8884 kev

APPENDIX II

ANGULAR DISTRIBUTION COEFFICIENTS FOR PHOTONEUTRON REACTIONS ON A 0^+ TARGET NUCLEUS

For a 0^+ target nucleus, the angular distribution coefficients $B_{t_1 t_2}$ (if $t_1 \neq t_2$) and $2B_{t_1 t_2}$ (if $t_1 = t_2$) have been tabulated by Carr and Baglin (Ca71) for photoneutron transitions to residual levels of spin $1/2$, $3/2$ and $5/2$. Using equation 2.12, transitions to levels with higher spins were calculated. The observed transitions in the photoneutron spectra of ^{206}Pb and ^{208}Pb, involved level spins and parities of $1/2^-$, $3/2^-$, $5/2^-$ and $7/2^-$ only.

The angular distribution coefficients are listed in this section in tables classified by channel spin s, rather than by the spin of the residual nucleus. For a given residual level j^-_{A-1}, the coefficients are chosen from the tables of 2 channel spins defined by

$$s\uparrow = j_{A-1} + 1/2$$

$$s\downarrow = j_{A-1} - 1/2 . \qquad \text{AII -1}$$

Thus, for each spin, the angular distribution expression is the sum of all non-zero components from 2 channel-spins as follows

$j_{A-1} = 1^-/2^-$: $s_+ = 0$, $s_+ = 1$

$j_{A-1} = 3^-/2^-$: $s_+ = 1$, $s_+ = 2$

$j_{A-1} = 5^-/2^-$: $s_+ = 2$, $s_+ = 3$

$j_{A-1} = 7^-/2^-$: $s_+ = 3$, $s_+ = 4$.

The coefficients are shown in the following five tables, for both E1-E2 and E1-M1 admixtures. Each coefficient corresponds to the interference between the matrix elements specified by the column and row of the table. Orders of ν from 0 to 3 in the expansion in terms of the Legendre Polynomials $P_\nu(\cos\theta)$ are included in these tables.

Matrix elements $\langle pL\,\ell s\rangle$ are specified as follows:

p = M for magnetic and E for electric interactions

L is the photon multipolarity

ℓ = s,p,d,f,g for ℓ = 0,1,2,3,4 neutrons

s = channel spin (= $\ell \pm \frac{1}{2}$) .

CHANNEL SPIN s=0

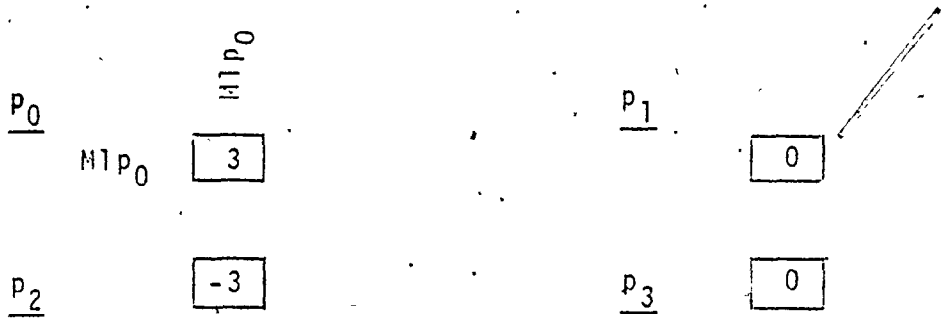

CHANNEL SPIN s=1

P_0

	E1s1	E1d1	M1p1	E2p1	E2f1
E1s1	3				
E1d1		3			
M1p1			3		
E2p1				5	
E2f1					5

P_1

	E1s1	E1d1	M1p1	E2p1	E2f1
			-7.348	9.487	
			-5.196	-1.342	9.859

P_2

E1s1		4.243			
E1d1		-1.5			
M1p1			1.5	*	*
E2p1				2.5	-1.75
E2f1					2.857

P_3

				7.746
			8.050	-4.382

*E2:M1 term is non-zero but is not considered in this experiment.

CHANNEL SPIN s=2

P_0

	E1d2	M1p2	M1f2	E2p2	E2f2
E1d2	3				
M1p2		3			
M1f2			3		
E2p2				5	
E2f2					5

P_1

E1d2	M1p2	M1f2	E2p2	E2f2
	-5.692	-6.971	-4.025	8.050

P_2

E1d2	1.5				
M1p2		-.3	4.409	*	*
M1f2			-1.2	*	*
E2p2				-2.5	-4.286
E2f2					.714

P_3

			-2..683	5.367

*E2:M1 term is non-zero but is not considered in this experiment.

CHANNEL SPIN s=3

P_0

	E1d3	E1g3	M1f3	E2p3	E2f3	E2h3
E1d3	3					
E1g3		3				
M1f3			3			
E2p3				5		
E2f3					5	
E2h3						5

P_1

	E1d3	E1g3	M1f3	E2p3	E2f3	E2h3
			-6.803	-8.050	5.270	
			-5.892		-2.535	9.487

P_2

	E1d3	E1g3	M1f3	E2p3	E2f3	E2h3
E1d3	-.429	4.454				
E1g3		-1.071				
M1f3			1.5	*	*	*
E2p3				.714	-5.611	
E2f3					-1.310	-3.180
E2h3						2.381

P_3

				.383	-2.342	7.825
				-6.639	5.071	-2.711

*E2:M1 term is non-zero but is not considered in this experiment.

CHANNEL SPIN s=4

P_0

	E1g4	M1f4	M1h4	E2f4	E2h4
E1g4	3				
M1f4		3			
M1h4			3		
E2f4				5	
E2h4					5

P_1

E1g4	M1f4	M1h4	E2f4	E2h4
	-6.708	-6.0	-5.196	7.348

P_2

E1g4	1.5			
M1f4	-.5	4.47	*	*
M1h4		-1	5.774	-8.165
E2f4			-1.786	-5.051
E2h4				

P_3

			-3.464	4.899

BIBLIOGRAPHY

(Au 62) E.H. Auerbach and F.G.J. Perey, Brockhaven Natl. Lab. Report BNL-765 (1962).

(Ba 64) R. Batchelor and K. Parker, Report AWRE O-78/64 (1964).

(Ba 79) J.N. Barkman, J.E. McFee, T.J. Kennett and W.V. Prestwich, Zeit. fur Physik A289, 325 (1979).

(Be 75) G.F. Betsch and S.F. Tsai, Phys. Reports 18C, 125 (1975).

(Be 76) R. Bergere, Lecture Notes in Physics, Photonuclear Reactions 1, Int. School on Electro- and Photonuclear Reactions, Springer-Verlag, Berlin, 1 (1976).

(Be 76a) F.E. Bertrand, Ann. Rev. of Nucl. Sci. 26, 457 (1976).

(Be 78) Z. Berant, Priv. comm. to W.V. Prestwich (1978).

(Be 79) Z. Bell, Ph.D. Thesis, Univ. of Illinois at Urbana (1979).

(Bi 79) Y. Birenbaum, Z. Berant, A. Wolf and R. Moreh, Phys. Lett. 88B, 239 (1979).

(Bo 76) A. Bohr and B. Mottelson, Nuclear Structure Vol II, Benjamin, N.Y., 670 (1960).

(Br 59) G.E. Brown and M. Bolsterli, Phys. Rev. Lett. 3, No. 10, 472 (1959).

(Ca 71) R.W. Carr and J.E.E. Baglin, Nucl. Data Tables 10, 143 (1971).

(Ca 75) M. Carbone, R. Cenni, R. Malvano and A. Molinari, Il Nuovo Cimento 27A, No. 1, 60 (1975).

(Cu 69) J.M. Cuttler, S. Greenburger and S. Shalev, Nucl. Instr. and Meth. 75, 309 (1969).

(Fa 75) L.W. Fagg, Rev. Mod. Phys. 47, 683 (1975).

(Fi 70) F.W.K. Firk, Ann. Rev. of Nucl. Sci. 20, 39 (1970).

(Fu 62) S.C. Fultz, R.L. Bramblett, J.T. Caldwell and N.A. Kerr, Phys. Rev. 127, 1273 (1962).

(Fu 76) E.G. Fuller and E. Hayward (edit.), Photonuclear Reactions, Benchmark Papers in Nucl. Phys. Vol 2, Dowden, Huntingden and Ross, Stroudsberg Pa. (1976).

(Gi 66) V. Gillet, A.M. Green and E.A. Sanderson, Nucl. Phys. 88, 321 (1966).

(Go 48) M. Goldhaber and E. Teller, Phys. Rev. 74, No. 9, 1046 (1948). Reprinted (Fu 76).

(Gr 64) L. Green and D.J. Donahue, Phys. 135, 703 (1964).

(Ha 64) E. Hayward, Photonuclear Reactions, Nuclear Structure and Electromagnetic Interactions, Oliver and Boyd, 141 (1964).

(Ha 76) S. Hanna, Lecture Notes in Physics, Photonuclear Reactions 1, Int. School on Electro- and Photonuclear Reactions, Springer-Verlag, Berlin, 275 (1976).

(Ha 77) M.N. Harakeh, K. vander Borg, T. Ishimatsu, H.P. Morsch, A. van der Waude and F.E. Bertrand, Phys. Rev. Lett. 38, 676 (1977).

(Ho 77) R.J. Holt, J.R. Specht, H.E. Jackson and R.M. Laszewski, Nucl. Instr. and Meth. 141, 125 (1977).

(Ho 79) R.J. Holt, H.E. Jackson, R.M. Laszewski and J.R. Specht, Phys. Rev. C20, 93 (1979).

(Hu 67) R.R. Hurst and D.J. Donahue, Nucl. Phys. A91, 365 (1967).

(Ke 78) T.J. Kennett, P.M. Brewster, W.V. Prestwich and A. Robertson, Nucl. Instr. and Meth. 153, 125 (1978).

(Ke 78a) T.J. Kennett, W.V. Prestwich and A. Robertson, Nucl. Instr. and Meth. 151, 285 (1978).

(Ke 78b) T.J. Kennett, W.V. Prestwich and A. Robertson, Nucl. Instr. and Meth. 151, 293 (1978).

(Le 73) M. Lewis et al, Phys. Rev. C8, 39B (1973).

(Le 78) C.M. Lederer and V.S. Shirley, Table of Isotopes, Seventh Ed., John Wiley and Sons, N.Y. (1978).

(Lo 78) G. Longo, F. Saporetti and Guidotti, Phys. Lett. 76B, 15 (1978).

(Ly 68) J.E. Lynn, The Theory of Neutron Resonance Reactions, Caledon Press, Oxford (1968).

(Ma 63) J.B. Marion and J.L. Fowler, Fast Neutron Physics II, Interscience Publishers, John Wiley and Son, N.Y., 1232 (1963).

(Mc 76) J.E. McFee, W.V. Prestwich and T.J. Kennett, Phys. Rev. C13, 1864 (1976).

(Mc 77) J.E. McFee, Ph.D. Thesis, McMaster University (1977).

(Mi 44) A. Migdal, J. Phys. (Moscow) 8, 331 (1944).
Reprinted (Fu 76).

(Mi 62) J. Miller, C. Schuhl and C. Tzara, Nucl. Phys. 32, 236 (1962).

(Mo 60) B.R. Mottelson, Proc. Int. Conf. in Nuclear Structure, Kingston, Canada, University of Toronto Press, Toronto, 525 (1960).

(Mo 73) A. Moalem et al, Phys. Rev. Lett. 31, 482 (1973).

(Oc 62) J.S. O'Connell, P.A. Tipler and P. Axel, Phys. Rev. 126, 228 (1962).

(Pi 77) R. Pitthan and F.R. Buskirk, Phys. Rev. C16, 983 (1977).

(Pr 62) M.A. Preston, Physics of the Nucleus, Addison-Wesley, Reading Mass, 511 (1962).

(Ra 67) D.C. Rasmussen, Y. Hukai, T. Inouye and V.J. Orphan, M.I.T. Report MITNE-85 (1967).

(Sa 74) G.R. Satchler, Physics Reports 14, 97 (1974).
Reprinted (Mc 77).

(St 50) H. Steinwedel and J.H.D. Jensen, Phys. Rev. 79, 1019 (1950). Reprinted (Fu 76).

(Ve 70) A. Veyssière, H. Beil, R. Bergère, P. Carlos and A. Leprêtre, Nucl. Phys. A159, 561 (1970).

(Wa 78) A. Wapstra and K. Bos, Atomic Data and Nuclear Data Tables 20, No. 1 (1977).

(We 61) R.E. Welsh and D.J. Donahue, Phys. Rev. 121, 880 (1961).

(Yo 76) D. Youngblood, Phys. Rev. C13, 944 (1976).